学位論文

Near-infrared Studies on Very Low-Luminosity Young Objects in the Taurus Molecular Cloud

近赤外線によるおうし座分子雲に付随した超光度ＹＳＯの研究

平成19年12月博士(理学)申請

東京大学大学院理学系研究科
天文学専攻

谷口 淳一

Near-Infrared Studies on Low-Luminosity Young Stellar Objects in the Taurus Molecular Cloud

Yoichi Itoh

Department of Astronomy, University of Tokyo

1998.1.

論文の要旨

ごく最近の、Gl229B などの褐色矮星や 51 Peg をはじめとする系外惑星の発見を考えると、非常に低質量の天体は普遍的に存在するのかもしれない。しかしながら星の初期質量関数 (IMF) が 0.2 $M_\odot$ 付近でピークを持つか否かはいまだに定かではない。低質量天体の統計的な研究の多くは 80 年代初頭までに得られた写真乾板によるデータに基づくもので、見直すべき時期に来ている。特に、高感度近赤外線検出器の発展により、低光度で低温の天体の観測が可能になった今、星形成領域において生まれたばかりの低質量天体を研究することは重要である。

そこで、修士課程においては、近傍の星形成領域であるおうし座分子雲の一部 (Heiles Cloud 2 をほぼカバーする約 1 平方度の領域) をサーベイ観測し、測光を行った。その限界等級は J バンドで 14.5 等で、以前の同領域の観測よりも 4 等も深い。その結果、赤外超過を伴う、すなわち、星周ディスクを持つ天体の光度関数 (Luminosity Function) は限界等級までターンオーバーが無く、既知の T タウリ型星よりも低光度な若い天体が多数あることがわかった。では、これらの天体はどうして低光度なのか? 最も魅力的な解釈は、それらの天体が若い超低質量天体である可能性である。天体の年齢を典型的な T タウリ型星と同じく $10^5 \sim 10^6$ 年と仮定し、最新の進化トラックを用いると、ほとんどの天体が 0.3 $M_\odot$ 以下、いくつかの天体に対しては 0.08 $M_\odot$ 以下と求まる。つまり若い褐色矮星である。しかし、低光度天体は比較的年齢が古い (10^8 年程度) という考え方も否定できない。この場合は、従来考えられていたよりも 10 倍以上長くディスクが生き延びることになる。

残念ながら、上記のサーベイ・測光観測からだけでは低光度天体の質量と年齢は同時に求めることができない。そこで、博士課程においては、これらの低光度天体を近赤外波長において分光観測することにより、天体の有効温度を推定し、各低光度天体を HR 図上にプロットすることに成功した。それに基づき、年齢と質量とを同時に決定することができる。その結果、これらの天体の年齢は T タウリ型星と比べ著しく年齢が古いわけではなく、「低光度」は天体

の質量がより軽いことを意味することがわかった。そして、Heiles Cloud 2 領域の IMF は褐色矮星までターンオーバーが見られないことが推測できる。

さらに、既知の T タウリ型星の半分以上が連星系をなすことから類推して、上記のおうし座低光度天体も伴星を持つ可能性が高いと考え、高解像度の近赤外撮像観測を行った。その結果、いくつかの非常に暗く (J ~17 等) かつ赤外線超過を持つ伴星候補天体が見つかり、その連星率は T タウリ型星と同程度に高いことがわかった。この伴星候補天体は、主星の低光度天体よりもさらに暗いことから、必然的により軽いことが予想される。これらの天体は若い褐色矮星でもとりわけ質量の軽いものであり、最も軽いものは巨大惑星の質量領域に限りなく近い。　以下に、この 2 つの観測・研究の詳細を述べる。

1. 低光度 YSO の近赤外分光観測

低光度天体の有効温度を求め、天体の質量と年齢を求めることを主目的とし、K バンド (2.2μm) の中分散 (R~1000) 分光観測を、ハワイ島マウナケア山頂にある英国赤外線望遠鏡 UKIRT と近赤外分光器 CGS4 を用いて行なった。露出時間は 100 秒から 2000 秒にわたり、K バンドで 13 等より明るい低光度 YSO 候補天体 21 個を観測した。ほかに、有効温度のテンプレートとして近傍の低質量矮星を、YSO のテンプレートとして T タウリ型星をそれぞれ数個観測した。典型的な S/N 比は約 70 である。

21 の低光度 YSO 候補天体中、11 の天体については Brackett γ が吸収線を示さない、または輝線を示し、天体の活動が活発であることから YSO と確認できた。近傍の矮星の観測と過去のデータ、および大気モデル計算をあわせることにより、大気の透過率の良い波長に位置するカルシウムとナトリウムの吸収線は、有効温度が 3500K 以下の矮星、巨星、YSO に対し、有効温度の良い指標であることが証明できた。特にこれらのラインは近い波長にあることからライン比をとることによって、若い天体にみられる星周ディスクによるベーリングの効果を打ち消すことができる。一方で、2.05~2.15μm の水の吸収バンドの強さも、天体の表面重力にも依存性があるものの、特に低温の天体に対し有効温度の関数となることがわかった。近

赤外域にあるこの 2 つの温度の指標、すなわちカルシウムとナトリウムのライン比および水バンドの強度から求まる、可視光で見える既知の T タウリ型星の有効温度は、スペクトルタイプが晩期のものに対しては、可視光の分光から求められたスペクトルタイプと矛盾しないことがわかった。こうして得られる有効温度は ±300K 程度の不確定さを持つ。

この結果、YSO であると確認できた 11 個の天体の多くが 3000K 程度の低い有効温度を持つことがわかった。こうして求められた有効温度を以前の測光観測の結果とあわせ、天体を HR 図にプロットし、最新の進化トラックと比べることにより、その質量と年齢を推定した。低質量の天体は有効温度が低いために、分子やダストが吸収係数に大きく関わり、進化経路の計算が難しい。いくつかの現在使用可能な進化モデルによって、求められる質量、年齢はファクターで異なるものの、多くの天体が 0.1~0.2$M_\odot$ の質量と 10^5 ~10^7 年の年齢を持つことがわかった。さらに、ある一つの天体の質量は 0.08$M_\odot$ 以下である確率が非常に高く、若い褐色矮星である可能性が高い。

このようにして分光観測から求められた天体の質量は、測光観測の結果から、年齢を仮定して求めた質量とファクター 2 程度の誤差しかなく、両者に矛盾のないことがわかった。測光観測から、星間吸収を補正した J バンドの光度関数は暗い天体にむかい単調増加で、ピークを示さないことから、おうし座分子雲 Heiles Cloud 2 に付随する若い天体の質量関数は、少なくとも測光観測の限界等級に対応する 0.05$M_\odot$ まで、軽い天体にむかい単調増加を示すことが推測できる。このことは、星はフラグメントのジーンズ長程度の長さでの分裂により生まれ、おうし座分子雲では形成される天体の質量が典型的に 1$M_\odot$ であるという、単純な理論のシナリオでは説明できない。

2. 低光度 YSO に付随する伴星の探査

おうし座分子雲に付随すると思われる 23 の低光度の YSO 候補天体に対して、JHK バンドの深い撮像観測を行ない、その伴星を探査した。このサンプルの一部は分光観測のサンプルと重複する。観測はマウナケア山頂にあるハワイ大学 2.2m 望遠鏡に 1024×1024HgCdTe 素子を持つ QUIRC 赤外カメラを取りつけて行なった。またガイド星がある場合には副鏡 tip-tilt を用い分解能をあげた。ピクセルスケールは 0.″061/pix で視野は 62.″5 四方である。Tip-tilt

を用いた場合、星像のFWHMは0.″4、用いない場合は0.″8程度であった。典型的な露出時間は10分で、限界等級はKバンドで18等ないしは16.5等である。観測は一部、パロマー5m鏡を用いても行なわれた。

連星系の探査は過去にも多くの観測があり、手法も多岐にわたる。現在までに行なわれた手法の主なものは、直接撮像のほかに、アストロメトリー法、ドップラーシフトを用いたもの、スペックル法、ルナオカルテーション法などがある。これらの手法は主星のごく近傍にある伴星まで検出できる反面、離角の大きなものが検出困難であったり、主星との光度差が大きいもの(ダイナミックレンジを必要とするもの)を検出できない面がある。直接撮像は、従来、シーイングサイズでその検出限界が決められており、多くの場合中心天体から2″以内にある天体は検出できなかった。しかし、近年のアダプティブオプティクスおよびtip-tiltに関する著しい進歩により、星像が0.″5以内に収まり、直接撮像により主星から1″以内の伴星も検出が可能になってきた(おうし座分子雲の距離では100AU以内)。本来、直接撮像法はダイナミックレンジの大きな観測手法であり、中心星に低光度YSO候補天体を選ぶことにより、非常に暗い伴星が発見される期待が持てる。

今回の観測では中心天体からの離角が0.″6以上で、光度差がKバンドで7等以下の天体に対してほぼ完全な検出ができることがわかった。1視野に対し、約1個の背景星または背景銀河が受かることが予想されるが、JHKの2色図から赤外超過を持っている天体のみを伴星とした。これらの天体は星周円盤を持つ若い天体である。観測の結果、中心天体との離角が2″から8″、Jバンドの等級が15ないし19等の若い伴星候補天体が6個見つかった。Jバンドの等級から求めた天体の質量が、分光から求めた質量と比較的良い一致を示すことが、分光観測からわかったため、これらの非常に暗い若い伴星候補天体についても、最新の進化トラックを用いて質量を推定した。天体の年齢を10^6年、または10^7年と仮定すると、いずれの伴星候補天体も質量が$0.08M_\odot$以下であり、褐色矮星の候補であることがわかる。さらにそのうちの3個については質量が$0.015M_\odot$以下と推定され、巨大惑星の質量領域にせまりつつある。

観測した低光度YSOの連星系率は、サンプル数が少ないものの、同じ進化段階にあり、より質量が重いTタウリ型星の連星系率と矛盾しない。この観測では質量が$0.006M_\odot$以上で、中心星との離角が1.″5以上の伴星に対してコンプリートである。伴星の軌道が円軌道でランダムな傾斜角を持って分布していると仮定すると、軌道周期が10^7 ~10^8日の連星系率は22^{+9}_{-10}%である。この数値はスペックル観測から得られたおうし座分子雲のTタウリ型星の数値と矛盾はなく、近傍の低質量星の連星系率より有意に高い。

以上の二つの観測から、星形成領域に非常に低質量の若い天体が多数存在すること、さらにその中には、若くて軽い褐色矮星が含まれる可能性のあることがわかった。

Acknowledgment

I would like to express my thanks to my adviser, Dr. Motohide Tamura of National Astronomical Observatory of Japan (NAOJ), for his scientific guidance to complete this work. He always encouraged me in my studies, and created an environment where I could study effectively. Prof. Takashi Tsuji of University of Tokyo gave me continuous support and discussion on stellar spectra. I learned a lot from the spectroscopic observations with Dr. Alan Tokunaga of the Institute for Astronomy in Hawaii. Dr. Tadashi Nakajima spent many hours discussing very low-mass objects. He gave me a chance of the observations at the Palomar observatory. The CIAO members always encouraged me. I am grateful to Dr. Hiroshi Suto, Dr. Noboru Ebizuka, Dr. Koji Murakawa, Mr. Katsuyuki Chikami, and Ms. Yumiko Oasa. Dr. Chris Packham taught me English, English culture, and new Japanese culture I didn't know. I really enjoyed conversations with him in English. I am also grateful to the infrared group at NAOJ, Dr. Yukiyasu Kobayashi, Dr. Masuo Tanaka, Dr. Takuya Yamashita, Dr. Hirokazu Kataza, Dr. Saeko, Hayashi, Dr. Hideki Takami, Dr. Naoto Kobayashi, Dr. Takeo Minezaki, Dr. Tomonori Usuda, Mr. Daigo Tomono, Mr. Koji Nakashima, and Ms. Yoshiko Okamoto. I thank Dr. Hugh Jones, Mr. Wako Aoki, Mr. Hirohiko Masunaga for discussions on astronomy, and Ms. Mikako Matsuura for the IRTS data. I had many excellent roommates at NAOJ, Dr. Takashi Hasegawa, Dr. Masatoshi Taga, Dr. Shin'ichirou Okumura, Mr. Takashi Miyata, Mr. Atsushi Mori, Mr. Osamu Nakamura, Ms. Shino Ohkubo, and Mr. Adbel-Naby Saad Aridah.

Four month stay in Hawaii for studying at the Joint Astronomy Centre was very impressive. I would like to thank Dr. Antonio Chrysostomou for supporting me not only on astronomy but also on the Big Island life with a Latin hospitality. Dr. Chris Davis, Dr. Stewart Ryder, and Mr. Lerothodi Leeuw always encouraged me at JAC. I am grateful to Prof. Jim Hough and Prof. Tom Geballe for inviting me to JAC. I am thankful to the staff in the Subaru office at Hilo, especially Prof. Norio Kaifu and Prof. Tetsuo Nishimura for their hospitality and support. A part of this stay was supported by the UK-Japan

collaboration fund from the JSPS.

I would like to thank Prof. Keith Matthews for kindful support at the Palomar observation, Dr. Andrew Pickles at the UH observation, and Dr. Tom Kerr at the UKIRT observation.

During the graduate course, I was supported by the fund from the JSPS.

Finally, I would like to thank my family for their support.

ABSTRACT

Recent infrared surveys of nearby dark clouds have detected a number of very low luminosity sources whose nature is unknown. They might be the best candidates for very low-mass young stars, some of them may be even substellar ($<0.08M_{\odot}$). However, these mass estimates are based on infrared photometry alone and the derived parameters are still uncertain. One of the best ways to resolve the uncertainty is to measure the effective temperature, placing the objects on the HR diagram.

In order to determine the effective temperature, near-infrared spectroscopy of 21 low-luminosity young stellar object (YSO) candidates have been carried out. These objects have been detected by our previous survey of Heiles Cloud 2, one of the densest parts of the Taurus molecular cloud.

Eleven objects are confirmed as YSOs by the Br γ feature. The line ratio of calcium feature to sodium feature, as well as 2.05μm$\sim$$2.15\mu$m H_2O gradient is found to be a good effective temperature indicator of dwarfs, giants, and YSOs. Using these indices, the effective temperature of the low-luminosity YSOs are determined. Most of the 11 low-luminosity YSOs have temperatures as low as 3000K. Detailed comparison of our photometric observations and evolutional tracks on the HR diagram suggest that such low temperatures indicate these objects to be very low-mass YSOs. Most of these objects have a mass of $0.1M_{\odot}$ $\sim$$0.2M_{\odot}$, and one object may be a young brown dwarf.

While the age of the very low-mass YSOs depends on evolutional tracks, it appear to be 10^5 year or 10^7 year. The mass of the low-luminosity YSOs estimated from photometric observations is in agreement with the mass derived from spectroscopic observations. Therefore, since the luminosity function of

class II objects in Heiles Cloud 2 increases toward lower luminosity, the mass function does not appear to have any turnover down to substellar regime.

Since most T Tauri stars have companions, most low-luminosity YSOs may also have companions. In order to find very low-luminosity YSOs, a near-infrared search for companions around 23 low-luminosity YSOs in the Taurus molecular cloud have been carried out. The direct imaging observations have been carried out partly with the tip-tilt telescope secondary.

Six very low-luminosity YSO candidates are discovered as companions. The magnitudes of the companions range from 15 to 19 magnitude at J band. The mass of the companions is estimated from J band luminosity, with using recent evolutional tracks of very low-mass stars, brown dwarfs, and giant planets. All of them are substellar, that is, the very low-luminosity companions are young brown dwarfs.

The magnitude differences between the very low-luminosity companions and the primaries range from 2 to 5mag at Ks band, which are significantly larger than the difference in T Tauri binaries. Statistical tests indicate that this is not only due to different observational techniques but also due to different parent-populations of the samples. It is possible that these very low-luminosity companions are formed by fragmentation of a disk around the central object.

The binary frequency is 22^{+9}_{-10}% for the system whose period is $10^7 \sim 10^8$day. This frequency is consistent with that of T Tauri stars, but significantly higher than that of nearby main sequence stars. Such a high binary frequency for low-luminosity binary systems implys that the binary formation mechanism by capture could be rejected.

Contents

Part I

General Introduction

Terminology

The terminology used in this thesis is briefly summarized.

1. Stellar objects are classified by the mass.
   - Low-mass stars are the stars with the mass of $0.2M_{\odot} < M < 2.5M_{\odot}$.
   - Very low-mass stars (VLM stars) are the stars with the mass of $0.08M_{\odot} < M < 0.2M_{\odot}$.
   - Brown dwarfs are the objects with the mass of $0.015M_{\odot} < M < 0.08M_{\odot}$. Also referred to substellar objects.
   - Very low-mass objects (VLM objects) are VLM stars and brown dwarfs.
2. Classification by luminosity is follows.
   - Low-luminosity objects are the objects with the apparent J band luminosity of $10 > J > 16$ mag.
   - Very low-luminosity objects are the objects with the apparent J band luminosity of $16 > J > 19$ mag.
3. The categories for objects in the early stages of evolution are follows.
   - Class I objects are the objects whose flux at 10μm is larger than that at 2μm. Also referred to (low-mass) protostars.
   - Class II objects are the objects whose flux at 2μm is larger than that at 10μm. Optically visible class II objects correspond to classical T Tauri stars (CTTSs).
   - Class III objects are the objects whose spectral energy distribution is similar to blackbody. Optically visible class III objects correspond weak-line T Tauri stars (WTTSs), naked T Tauri stars, or post T Tauri star for low-mass stars.
   - Young stellar objects (YSOs) are either class I, class II, or class III objects.
   - Pre-main sequence stars (PMSs) are either class II or class III.

We may regard very low-mass objects to be ubiquitous, considering the discoveries of the definitive brown dwarf, Gl229B, and of extra-solar giant planets such as 51 Pegasi. However it is still an open question whether the initial mass function (IMF) turns over at low-mass ($\sim 0.2 M_{\odot}$). Frequently quoted statistical studies of low-mass objects are taken from older photographic observations. A comprehensive near-infrared survey which is suitable for learning the low-mass part of IMF has been limited by small format and less sensitive infrared detectors.

Recent progresses on near-infrared arrays enable us to study young low-mass objects in star forming regions. Near-infrared surveys of nearby star forming regions, such as Taurus, Ophiuchus, Chamaeleon, and Orion, reveal a numerous population of low-luminosity YSO candidates. Since they have near-infrared excess, they are thought to have circumstellar disks. However, their infrared luminosity is one order of magnitude fainter than that of typical T Tauri stars, and their nature is unknown. They may be very low-mass young stars or young brown dwarfs.

In this general introduction, recent progresses on low-mass stars/very low-mass objects and the motivation of this study are described.

Chapter 1

Reviews on Studies of Very Low-Mass Objects

1.1. Nearby Very Low-Mass Objects

The shapes of the initial mass function are very different at low mass between the mass function of Salpeter (1955) and that of Scalo (1986). However, Salpeter considered the luminosity function only in the range M_V = 4.5 to +13.5, which corresponds to $0.4M_\odot$ <M<$10M_\odot$. The data sets considered by Scalo are sparse or incomplete below M_V >14. Therefore neither the mass function of Salpeter nor that of Scalo do not provide enough information on very low-mass stars or brown dwarfs. Moreover, the complex behavior in the mass-luminosity relation due to H^- opacity and convection zone makes it difficult to convert luminosity to mass below $0.3M_\odot$. Combining these uncertainties with the effect of unresolved binary stars, the mass function of nearby stars does not appear to have a peak at $\sim 0.3M_\odot$ unlike the Scalo function (Kroupa, Tout, & Gilmore 1993). Recent optical and infrared observations of low-mass nearby stars suggest that the mass function increases toward the end of the main sequence (Tinney et al.1993; Kirkpatrick et al.1994)

Very recently, 3 field brown dwarf candidates are identified by a near-infrared sky survey (DENIS; Delfosse et al. 1997). They are ~13 mag at K band, and their I, J, K colors are very red. One of them is confirmed as a brown dwarf by optical spectroscopy (Martin et al. 1997; Tinney, Delfosse & Forveille 1997).

Observations of gravitational microlensing effect are another powerful technique to search low-mass objects. Currently three groups are studying the LMC and looking for low-mass objects, including brown dwarfs and planets, in the galactic halo. Although the detection events are only several, both MACHO group and EROS group conclude that the mass of the halo is not contributed more than 50% by the objects in the mass range $3\times10^{-4}M_\odot$ <M<$0.06M_\odot$ (MACHO group; Alcock et al. 1995) or by the objects in the mass range 10^{-7} <M<$0.1M_\odot$ (EROS group; Ansari et al. 1996).

Review on the spectroscopic studies and the studies on multiple systems are described in Part II and Part III, respectively.

1.2. Young Very Low-Mass Objects

As discussed by Stringfellow (1991) and Burrows et al.(1993), very low-mass stars and brown dwarfs are relatively luminous and have a higher temperature at their younger evolutionary stage (10^6 yr ~ 10^7 yr). Therefore the detection of such objects is relatively easier than detecting more aged ones. These young brown dwarfs could be found associated with nearby star forming regions. Considering their very red spectral energy distribution and the high extinction of star forming regions, the near infrared wavelengths are most important for studies of such objects.

1.2.1. Studies in Open Clusters

The Pleiades is one of the best studied open clusters including brown dwarf searches. Since there is little interstellar extinction, optical observations are possible.

Stauffer et al.(1989) conducted $V \sim K$ band photometry and concluded that very low-mass stars and brown dwarfs, if any, are not the major component of the Pleiades. In contrast, Simons & Becklin (1992) carried out I and K band imaging of 200 arcmin^2 of the Pleiades. They pointed out that the mass function is characterized by a power law in the mass range $0.1M_\odot$ ~$0.04M_\odot$ and that the combined mass of very low-mass stars and brown dwarfs would contribute significantly to that of the Pleiades. Both are based on photometry and star count. Their discussions are statistical, therefore proper motion studies and spectroscopic observations are needed for more definite identification.

Hambly, Hawkins, & Jameson (1991) made a deep proper motion survey for the Pleiades and found about 10 brown dwarf candidates. J and K band spectra of some of these objects were obtained by Steele et al.(1995). Although their spectra being poor signal-to-noise ratio, low temperatures of some objects imply brown dwarfs. Oppenheimer et al.(1997) obtained optical high-resolution spectra, and made lithium test.

1.2.2. Imaging Survey of Star Forming Regions

Young stellar objects have been investigated in many star-forming regions at various wavelengths, but an infrared study has two advantages in obtaining a census of low-mass YSOs in molecular clouds: (1) At infrared wavelengths, the light from the source is less affected by extinction in the cloud than at optical wavelengths, and (2) low-mass YSOs radiate a large portion of their energy in the infrared.

Strom, Strom, & Merrill (1993) observed the L1641 cloud in the Orion giant molecular cloud with completeness of K=14.7 mag. They concluded that the YSO aggregates in the cloud appear to have formed within 1Myr with the Scalo initial mass function. Comeron et al. (1993) surveyed a core of the ρ Ophiuchi molecular cloud with completeness of K = 15.5 mag and concluded that the luminosity function increases down to their completeness limit. Itoh (1995) surveyed Heiles Cloud 2 and L1495 cloud in the Taurus molecular cloud. Detailed descriptions of this survey are presented later. Oasa et al.(1998) carried out a deep near-infrared observation of the central core of the Chamaeleon I molecular cloud with completeness of K=16.5 mag. They found two peaks in the luminosity function of the YSO candidates. Wilking et al.(1997) observed the R Coronae Australis molecular core with completeness limit of K=16.5 mag.

Many infrared suveys have also been conducted in the more massive star-forming regions. For example, Okumura (1997) carried out the near-infrared survey of the central part of W51A, known as massive star-forming region. They found ~200 O and B type stars, and concluded that there are two sequential star formations. However, all massive star-forming regions are so distant that most of these surveys are not deep enough to detect low-luminosity objects discussed in this thesis.

Reviews on the spectroscopic studies of YSOs and the studies on YSO multiple systems are described in Part II and Part III, respectively.

1.3. Theory of Low-Mass Stars

1.3.1. Theories of Low-Mass Star Formation

Larson (1985) suggested that a cloud core collapses to a filament, then fragmentation into a clump occurs by gravitational instability. The minimum mass of the clump is roughly one-quater of the Jeans mass (Larson 1992). Because the Jeans mass is the order of $1M_{\odot}$ for typical molecular cloud, the minimum mass is predicted to be of the order of $0.3M_{\odot}$.

Mouschovias & Morton (1991) examined the role of ambipolar diffusion in the formation of molecular cloud cores. They found that the characteristic length of protostellar core produced by fragmentaion is about 0.14 pc and the characteristic mass is about 1 $M_{\odot}$ for typical dark clouds.

Recently, Nakano (1998) discusses the formation of VLM objects. He considered the magnetically supercritical cloud and the effect of the outflow of the YSO. He concluded that there is no critical mass around $0.1M_{\odot}$.

1.3.2. Theories of Evolution of Low-Mass Objects

Several groups have developed evolutional tracks of low-mass stars, brown dwarfs, or even giant planets.

D'Antona & Mazzitelli (1994) calculated evolutional tracks of low-mass stars as well as brown dwarfs using opacities of Alexander et al.(1989) and of Kurucz (1991). Combining these two opacities under gray-atmosphere with two convection models, they calculated 4 evolutional tracks. However they failed to find the evolution track which is in agreement with observational results such as loci of low-mass dwarfs on the HR diagram and Li depletion in the α Persei open cluster.

Swenson (Hartigan, Strom & Strom 1994) also made an evolutional track for low-mass

stars. Unfortunately, his original paper was not published.

Nelson, Rappaport & Joss (1993) investigated an evolutional track for low-mass stars and brown dwarfs. They used analytic fits of the Alexander opacities and assumed gray-atmosphere in their calculations.

Recently evolution tracks with non-gray atmosphere have been developed. Chabrier & Baraffe (1997) calculated an evolutional track for very low-mass stars ($0.07M_\odot$ <M<$0.8M_\odot$) using the Alexander & Fergusson (1994) opacities and considering non-gray atmosphere model (named *NextGen*). Their model can account for the loci of very low-mass main sequence stars on the HR diagram. While their calculation included the most recent physics concerning on very low-mass stars, their limited results on mass and age make it difficult to compare with current observational data and therefore to confirm accuracies of their evolution track model. Although the mixing length of turbulent convection is important for a massive star, they did not examine the effect of this parameter and fixed even for the star with M>$0.2M_\odot$. As pointed out by Luhman & Rieke (1998), this model should be acceptable below $\sim 0.2M_\odot$.

Another evolutional track was built by Burrows et al.(1997). They calculated evolutional tracks for extra-solar giant planets and brown dwarfs ($0.0003M_\odot$ $\sim$$0.07M_\odot$). They used the HITRAN database and other calculations for opacities, and considered non-gray atmosphere. They made not only calculations of evolution tracks but also predictions of photometric colors of the objects.

As low-mass objects being low temperature, opacities for low temperature are need for precise calculation. However opacities under low temperature conditions should be concerned with a number of molecules and even dust. Therefore opacities for low temperature are still not trustworthy.

1.3.3. Atmosphere of Low-Mass Objects

Due to a high surface gravity and low temperature, spectra of very low-mass stars and brown dwarfs are no longer approximated by blackbody. Collision-induced absorption of H_2, as well as absorption by H_2O and other molecules becomes important for M dwarf and brown dwarf spectra.

Recently model atmospheres and its emergent spectra become available for M dwarfs and brown dwarfs with zero metallicity (Saumon et al. 1994), and with solar abundance (Tsuji & Ohnaka 1994; Allard & Hauschildt 1995).

Tsuji, Ohnaka, & Aoki (1996) proposed dust formation in late type dwarfs and brown dwarfs. This is observationally confirmed by Jones & Tsuji (1997).

Chapter 2

The Previous Survey of the Taurus Molecular Cloud and the Motivations of This Study

A JHK near-infrared survey of Heiles Cloud 2 have been carried out (Itoh 1995, Master thesis; Itoh, Tamura & Gatley 1996). Heiles Cloud 2 is one of the densest regions of the Taurus molecular cloud. The limiting magnitude of the survey was 14.5 mag at J band, which is about 4 magnitude deeper than the previous surveys. 1394 sources were detected at J band, and 47 sources were classified as class II objects based on the near-infrared color-color diagram (Fig. 1). The differential luminosity function of the class II objects in the survey region does not appear to have any cutoff (fig. 2). The majority of the class II objects are low-luminosity class II objects.

Then, what is the origin of their low luminosity? They might be low-mass class II objects. Assuming that their age is similar to that of classical T Tauri stars (CTTSs) in the Taurus molecular cloud ($10^6 \sim 10^7$ yr), and using a recent evolutional track of low-mass objects, we estimate that their masses range from $1M_\odot$ to $0.03M_\odot$. Some objects may be

substellar, therefore young brown dwarfs. An alternative hypothesis for the explaination of the low luminosity is that they are older than the assumed age and the dissipation timescale of the circumstellar disk is longer than that of typical CTTSs. Some objects may be as old as $\sim 10^8$ years. However, from the photometric observations alone, it is impossible to simultaneously determine the mass and age of a young stellar object.

In order to overcome this difficulty, we have conducted a near-infrared spectroscopy of low-luminosity class II objects to derive their effective temperature and to estimate their mass and age. The observations have revealed that these low-luminosity objects are indeed very low-mass young objects, not simply older objects. Therefore we concluded that the mass function of the class II objects in the survey region does not appear to have any turnover down to brown dwarf regime.

Furthermore, in order to find fainter YSOs, we have carried out a deep high-resolution imaging observation around the low-luminosity YSOs. Six very low-luminosity YSO candidates are found as companion, whose J band magnitudes are between 15 and 19 mag. Such faint magnitudes imply that the objects are brown dwarfs. The binary frequency of low-luminosity YSOs is as high as that of T Tauri stars, and is sinificant higher than that of nearby dwarfs.

The results of the spectroscopic observations are described in Part II. The results of the deep high-resolution imaging observations are described in Part III.

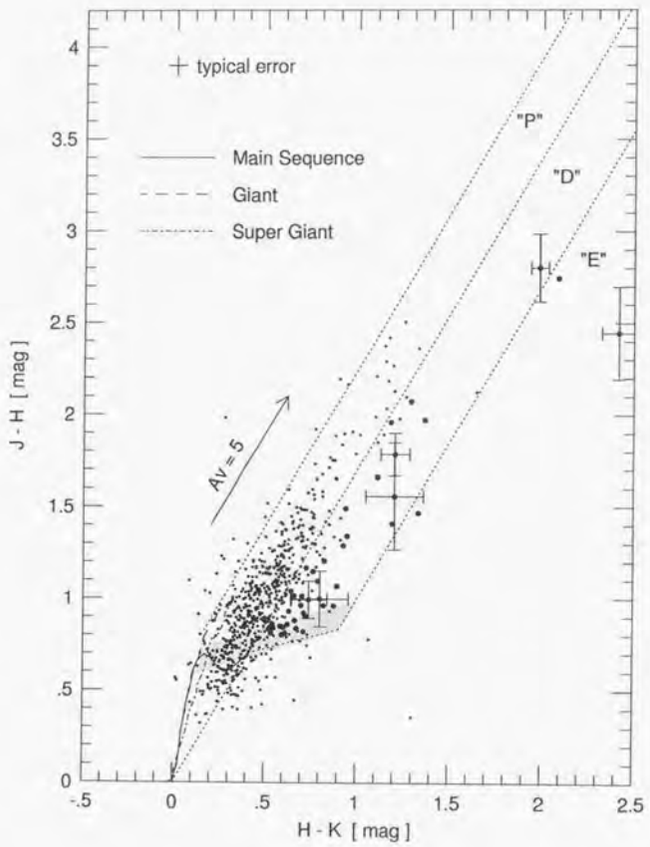

Fig. 1.— The JHK color-color diagram for Heiles Cloud 2. The YSO candidates identified by the previous near-infrared survey (Ihot 1995) are shown by filled circles.

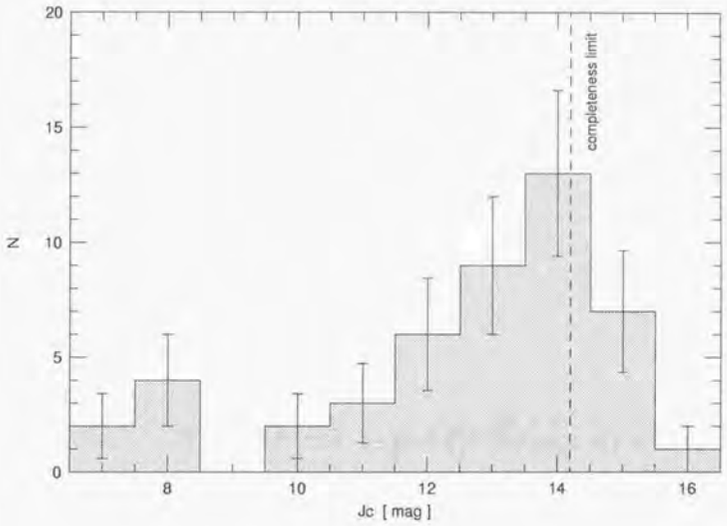

Fig. 2.— J luminosity function of the class II object candidates in Heiles Cloud 2. The histogram shows the differential funcion of Jc, after correction of the observed J magnitudes for extinction.

Part II

Near-Infrared Spectroscopy of Low-Luminosity YSOs in the Taurus Molecular Cloud

Chapter 1

Previous Spectroscopic Studies on Low-Mass Objects

1.1. Spectroscopic Observations of Low-Mass Main-Sequence Stars

Optical Spectroscopy

Spectroscopic studies on late type dwarfs were mainly carried out in R and I band, because those objects radiate a large portion of their energy in infrared and important features, such as TiO and VO, are in these wavelengths. Spectral types or effective temperatures of late type dwarfs have been usually derived from its broad band color, or, if those spectra were taken, from its narrow band color or flux ratio of continua (Kirkpatrick, Henry, & McCarthy 1991). Recent progresses of atmosphere model of late type dwarfs make it possible to quantitatively derive effective temperatures of M dwarfs from optical spectra (Kirkpatrick et al. 1993).

A lithium absorption line is the best diagnosis of a field brown dwarf. Martin et al.(1997) observed the field brown dwarf candidate discovered by DENIS survey and found the Li absorption line at 670.7nm. This fact strongly suggests the mass of the object is

less than $0.06M_{\odot}$. The lithium test can also be used for a brown dwarf candidates in open clusters. Basri, Marcy, & Graham (1996) observed a brown dwarf candidate in the Pleiades, and found the Li line in absorption. Note, however, low-mass YSOs also have the Li absorption line, whose temperature of the central core is not yet high enough to destroy Li. Therefore, the diagnosis of a brown dwarf using the Li absorption line cannot be used for low-luminosity YSOs.

Near-Infrared Spectroscopy

Since M type stars and brown dwarfs emit the most portion of energy in near-infrared, near-infrared spectroscopy is more suitable for understanding photospheric property of late type stars. Medium resolution spectroscopic observations revealed several spectral features vary significantly with temperature (Jones et al. 1994; Ali et al. 1995). Moreover, comparisons of observed spectra with synthetic spectra gave effective temperatures, metallicities, and surface gravities of the objects (Legett et al. 1996; Jones et al. 1996).

1.2. Optical Spectroscopy of Low-Luminosity YSOs

The YSOs have been observed by spectroscopy in optical, but they are limited to the bright PMSs or the PMSs with small interstellar extinction.

Briceño et al.(1997) and Martín (1997) observed X-ray sources located far from molecular clouds. They observed mainly Li line at 670.7 nm, and pointed out that these sources are not post T Tauri stars but young main sequences of age up to $\sim 10^8$ yr.

Recently, Luhman, Liebert, & Rieke (1997) carried out an optical spectroscopy of a young brown dwarf candidate within the ρ Ophiuchi star-forming region. This object has a mid-infrared excess and exhibits little extinction. The optical spectrum of this object shows deep TiO and VO bands in 700 nm$\sim$900 nm, which indicate a spectral type of M8.5$\pm$0.5. With near-infrared photometry, the mass and age are estimated to be $0.01\sim0.06M_{\odot}$ and

3$\sim$10M yr, respectively, from recent evolutional track on the HR diagram. Although this result is of course remarkable, an optical observation is restricted to the objects little affected by extinction, therefore the objects away from star-forming cloud core. This large distance from the cloud core may be responsible to the relatively old age of this object.

1.3. Near-Infrared Spectroscopy of Low-Luminosity YSOs

Near-infrared spectroscopy is a suitable tool for understanding physical parameters of young objects embedded within the clouds.

Williams et al.(1995) carried out K band spectroscopy of the low luminosity sources in the ρ Oph cloud. However, the low signal-to-noise ratio of the data prevented them from quantitative discussion based on spectral features.

Greene & Meyer (1995) conducted J, H, and K band spectroscopic observations of YSOs in the ρ Oph cloud. The sample was a flux-limited one ($K < 10.5$ mag) and many objects had small veiling by circumstellar disks. The equivalent widths of K band features (Br γ, CO band head, Na I line, and Ca I line) were measured. The effective temperatures and the amount of veiling effect at K band were estimated from these features. The mass and age of the objects were deduced to be $0.1\sim2.5M_{\odot}$ and 3×10^5yr, respectively, using recent evolutional track on the HR diagram. The median mass of the sample is $\sim 0.5M_{\odot}$, therefore these objects are embedded low-mass YSOs.

Greene & Lada (1996a), Meyer (1996), and Luhman & Rieke (1998) also try to derive physical properties of embedded YSOs in Ophiucus, Taurus, and Orion.

The possible weak point of near-infrared medium resolution spectroscopic study was that it is not well established whether the near-infrared spectral features come from the photosphere. If the circumstellar disk, the disk atmosphere, or the circumstellar envelope is responsible for the near-infrared features, the derived temperature from the near-infrared

features does not show the effective temperature of the object itself, and the mass and age of the object cannot be correctly estimated from near-infrared spectroscopy. This problem might be crucial for class I objects and class II objects.

Recently this problem has been solved by Greene & Lada (1997), who confirmed that the K band features are of photospheric origin. They carried out a high resolution (R=21,000) K band spectroscopic observation of a sample of flat-spectrum and class II objects in the ρ Ophiuchi cloud. The evolutional stage of flat-spectrum YSOs is thought to be between the stage of class I and that of class II objects. The flat-spectrum and class II objects exhibit CO and and atomic (Na, Sc, Si) line shapes which are consistent with those expected for rotating stellar photosphere. Therefore effective temperature can be correctly estimated from near-infrared features.

Chapter 2

Observations

The observations were carried out on 1996 November 24–26 with the Cooled Grating Spectrometer 4 (CGS4, Mountain et al. 1990) on the UK Infrared Telescope (UKIRT) at Mauna Kea, Hawaii. The CGS4 is equipped with a 256×256 InSb array. The 75 line mm^{-1} grating was used to cover the wavelength range of 1.8 – 2.4 μm. The 0.″6 width slit was used. The spectral resolution $R \equiv \lambda/\delta\lambda$ is about 400 per pixel at 2.21 μm. The integration time used for each source was typically 1 – 20 second per exposure depending on source brightness. In the most cases, 96 exposures were taken of each object. Sky subtraction was performed by nodding the telescope approximately 16 arcsec up and down the slit.

The objects are 21 low-luminosity YSO candidates, 3 T Tauri stars, and 7 late-type dwarfs (Table 1). The low-luminosity YSO candidates are listed in Itoh (1995). These objects have been found by the near-infrared survey of Heiles Cloud 2 of the Taurus molecular cloud using the Kitt Peak 1.3 meter telescope and SQIID multi color camera. The sample is flux-limited, and their K band magnitudes range from 8 to 12 mag., which are one or two orders of magnitude fainter than that of typical T Tauri stars. Considering that they have near-infrared excess which implies a circumstellar disk, they may be low mass YSOs analogous to CTTSs.

For the Taurus objects, SAO76542(A2V) was used to correct for the effects of atmospheric absorption. For late-type dwarfs, the dwarfs in the spectral type range A0 – A3 and at similar air mass were used. Exposures of an incandescent lamp on and off were taken at the start of each night as dome flat. Also exposures of a krypton lamp were taken for wavelength calibrations.

Chapter 3

Data Reduction

Extraction of Spectra

The Image Reduction and Analysis Facility (IRAF) software was used for all data reduction. The reduction process consisted of subtraction of dithered pair each other, and flat fielding using dome flats. The data frames were geometrically transformed to correct for the curvature of the slit image caused by the grating (IDENTIFY,REIDENTIFY,FITCOORDS,TRANSFORM). This geometric transformation and wavelength calibration were derived from emission line of the krypton lamp taken at the nearest time. Background subtraction was done by using sky region (BACKGROUND). Individual spectra from the transformed images were extracted using APALL task. The extracted region was automatically determined where the intensity of the object is more than 20 % of the peak intensity in each wavelength. Extracted spectra were normalized and averaged to produce the final spectrum. Some low signal spectra due to tracking error of the telescope are rejected. Then the object spectra were divided by the standard star spectra and multiplied by a blackbody spectrum of the temperature appropriate to the spectral type of that standard star (Tokunaga 1998). Brackett γ line absorption at 2.166μm in A type standard stars is removed by interpolation of the nearby continuum, using SPLOT

task.

Measurements of Equivalent Widths

Equivalent widths for several features were computed with SPLOT task. The SPLOT task has several methods to measure an equivalent width. An equivalent width of a single line is measured using "e" command of SPLOT task by simple integration of the intensity, or using "k" command by Gaussian fit of the line. Equivalent widths of blended multiple line profiles are measured using "h" command by simple integration of the flux, or using "d" command of SPLOT by Gaussian profile fit. An equivalent width is measured by these four methods for typical metallic lines with typical signal-to-noise ratio (S/N). The derived equivalent widths are 1.54 $\AA$ for "e", 1.52 $\AA$ for "k", 1.54 $\AA$ for "h", and 1.64 $\AA$ for "d". The scatter in these derived equivalent widths is much smaller than the errors caused by other factors.

Error Estimation

Several kinds of signal-to-noise ratio estimation have been proposed for an equivalent width of a line. Ali et al.(1995) calculated the formal error of the equivalent widths, assuming that $\sigma_{line} \sim \sigma_{cont}$ for the case of background dominated data and weak absorption lines. The error is given as

$$\sqrt{2N_{pixels}} \times \text{dispersion} \times \sigma_{cont} \tag{3.1}$$

where N_{pixels} = the number of spectral pixels contained within the defined band edges for the line and σ_{cont} is the rms noise of the continuum as calculated the continuum regions. The formal errors of the objects are estimated for each object by the this method. The derived S/N are listed in Table 1. However, the number of pixels of the continuum is too small. Ali et al. define the six continuum regions, whose band widths are 30$\AA$ to 70$\AA$. Only 2 or 4 pixels covered each continuum region with their medium spectral resolution ($R \sim$1380). The errors were estimated from only 15 pixels. This is also the case for this

UKIRT observation. Therefore another method is need for error estimation.

The deviation of the flux between each spectrum also means the observational error at the wavelength. The derived signal-to-noise ratios of the objects and the standard stars are shown in Table 1 (S/N_{obj} and S/N_{std}). S/N_{obj} is calculated before divided by the standard star. The signal-to-noise ratios of the final spectra are calculated as follows.

$$S/N_{est} = \sqrt{(S/N_{obj})^2 + (S/N_{std})^2} \tag{3.2}$$

Measuring the equivalent width, in actual, these derived signal-to-noise ratios are not used to estimate error, because the difficulty in finding real continuum is main factor of error of the equivalent width. Nevertheless, the estimated S/N_{est} values are in agreement with the error of the equivalent width due to continuum fit.

Chapter 4

Results

4.1. Spectra

The K band spectra of low-luminosity YSO candidates, T Tauri stars, and late-type dwarfs are shown in Figure 1, Figures 2, and Figure3, respectively. Prominent features in the spectra are HI Br γ (2.17μm), Na I doublet (2.21μm), Ca I triplet (2.26μm), CO band (2.29μm and longer), and H_2O absorption (<2.15μm and >2.3μm). The measured equivalent widths of the lines and bands are tabulated in Table 2. The errors are estimated from the continuum fit. The strength of H_2O absorption is measured as gradients of the apparent continuum in 2.05–2.15μm and 2.29–2.40μm (see discussion below).

4.2. Prominent Features

4.2.1. Br γ

As Ali et al.(1995) pointed out, though the HI Brackett γ line is the strongest atomic feature in the 2.2μm atmospheric window in early type stars, this line is not suitable to determine effective temperature of YSOs, because the strength of this line may indicate

activities of the boundary region of YSOs. Some observed low-luminosity YSO candidates show Br γ in emission, and some others show in absorption.

The objects with Br γ absorption may be field stars. Ali et al.(1995) shows that B, A, and early F type stars have $6\AA \sim 10\AA$ absorption in the Br γ equivalent width. The star count by Jones et al.(1981) predicts that there are 6 B and A type stars for $K < 11$, or 9 for $K < 12$. Therefore, these stars with Br γ absorption could be background early-type dwarfs. An A0 type field star with $K = 11$ behind the cloud (typical A_K=1) would locate at 1 Kpc from the Sun and 300 pc away from the Galactic plane. Note that the number of these distant early stars does not increase for $K > 12$ toward high latitude direction such as the Taurus molecular cloud.

Figure 4 shows the color-color diagram of the observed YSO candidates as well as the other YSO candidates and field stars toward Heiles Cloud 2. The intrinsic color of main-sequence, giant (Bessell & Brett 1988), supergiant (Tokunaga 1998) are also plotted with the reddening vector (Koornneef 1983). Following the scheme discussed by Strom et al.(1993), the near-infrared sources are classified into three groups. In the "P" region on the color-color diagram, located are main sequence stars, giants, class III objects, and the class II objects whose near-infrared excess is small. In the "D" region, a part of class II objects are located. Class I objects are located in the "E" region on the color-color diagram. The objects located in the "D" region or the "E" region were identified as YSO candidates by the previous photometry (Itoh et al. 1996). The objects with absorption less than 5 $\AA$ or with emission in Br γ line are denoted by filled square. The objects with absorption more than 5 $\AA$ in Br γ are shown by cross. The YSO candidates without the spectroscopic observation are denoted by open square. The objects with Br γ absorption are located near the boundary between the "P" region and the "D" region. Therefore these objects may be indeed early-type background stars and be misidentified as YSO candidates by photometry errors. The uncertainty of slope of the reddening vector may account for the misidentification. Alternatively these may be YSOs with little near-infrared excess and

with less activities.

Figure 5 shows the histogram of the objects with and without Br γ emission as a function of J band magnitude which is corrected its extinction estimated from the color-color diagram. The ratio of the YSO candidates without Br γ absorption to those with Br γ absorption appears not to have any correlation with their luminosity. Therefore the luminosity function of the YSO candidates without Br γ absorption, as well as that of candidates with Br γ absorption, does not have any cuttoff, down to the maglitude limit of the previous survey.

4.2.2. Na I

The Na I feature at 2.20μm is a doublet (2.206μm and 2.209 μm). Their excitation energy is very low (3.19eV), thus this feature is strong in M type stars. Figure 7 shows that this Na I feature is the strongest atomic feature in the K band for dwarfs with T_{eff} <3400K. This feature is strong and has weak dependence on gravity, therefore this is used for spectral classification. Ali et al. (1995) pointed out that dispersion of the equivalent widths in Fig. 7 is mainly due to metallicity.

As indicated by Wallace & Hinkle (1996) and Greene & Lada (1997), Si and Sc lines near the Na lines are moderately strong for K type stars, and become much stronger in late-type giants and supergiants. These Si and Sc lines are too close to be resolved by our UKIRT observation. Therefore Si and Sc lines may be contaminated in the Na 2.20μm feature for a hot object or a very young object (a very young object has lower surface gravity like giants). However, usual YSOs, even flat spectrum YSOs (class II_D), have surface gravities more similar to dwarf stars than to giant stars (Greene & Lada 1997).

In a T Tauri star, Na I lines in optical wavelengths shift to redward, and this fact suggests that this line is produced in the boundary region (Gullbring et al. 1996). Cohen & Kuhi (1979) found that about 8% of T Tauri stars have the optical Na I line in emission. However, the K band Na I lines of CTTSs have symmetric profiles and do not shift (Greene & Lada 1997). The FWHMs of those lines are 5$\sim$30km/s. much narrower than the FWHM of the optical lines thought to be of boundary region origin, such as Hα (Gullbring et al.1996). Therefore, the Na I lines are of photospheric origin.

4.2.3. Ca I

The Ca I feature at 2.26μm is a triplet, whose excitation energy is 4.68eV. Because of this moderate excitation energy, the Ca I feature has a peak in its equivalent width around 3400 K and decreases dramatically in the cooler objects (Figure 7). This line is also strong and has weak dependence on gravity, therefore this is used for spectral classification.

As Ali et al.(1995) and Wallace & Hinkle (1996) show, this Ca feature is dominated by Ca I triplet and the 2.263μm Fe I line for hotter (earlier than K7) stars, and Si line for the object whose spectral type is earlier than G8.

A T Tauri star has the optical Ca II line in emission, as one of the criteria for a T Tauri star. Gullbring et al.(1996) found that this Ca II line has a peak with broad and slightly blue asymmetric component. This feature suggests that the optical Ca II line is produced in its chromospheric region and boundary region. To date no high-resolution observation has been carried out for the K band Ca I feature.

4.2.4. Mg I

The Mg I feature at 2.28μm is weaker than the Na I or Ca I features. Its excitation potential of 6.72 eV implies that this feature has a peak in its equivalent width at higher temperature than that for Ca I. However, the observed equivalent width is nearly flat between 3500K and 5000K. Ali et al.(1995) claim that this is due to additional blended

lines. High resolution spectra by Wallace & Hinkle shows that the weak Ca line could contribute to the equivalent width of this Mg feature.

This feature is located near the CO(2,0) band head, thus making it difficult to identify the continuum at redward of Mg I line. Moreover, for late type stars H_2O band absorption affects the continuum level of this region. Therefore reliable measurement of Mg I feature could not be done for some objects.

4.2.5. CO band

The $^{12}CO(2,0)$ overtone bandheads are the strongest absorption features in the K band for cool stars. However, because the strength of CO bandhead has sensitive dependence on surface gravity of the object, it is not suitable to use the strength of the CO bandhead as a temperature scale. Moreover, some very young objects has CO band head in emission (Greene & Lada 1996b). The CO strength also indicates the activities of the YSOs, such as outflow.

4.2.6. H_2O

The H_2O absorption bands in near-infrared are thought to be a sensitive function of effective temperatures for very cool stars (e.g. Aaronson, Frogel , & Persson 1978). Especially, for the object with T_{eff} <3500K, the strength of the H_2O absorption varies significantly with its effective temperature (Kleinmann & Hall 1986, Ali et al. 1995). Jones et al.(1995) observed 3μm H_2O absorption band for M dwarfs and, by comparing synthetic spectra they concluded that changes in metallicity and gravity have a small effect on the strength of the observed water bands whereas temperature changes produce large differences in strength.

Several techniques were employed to measure the strength of the H_2O absorption.

Aaronson et al.(1978) made photometry using two specific filters for the H_2O absorption at 2.0μm region. The derived values for the H_2O absorption are sometimes called as photometric indices. On the other hand, Kleinmann & Hall (1986) and Ali et al.(1995) measured the flux ratio of spectra in the bands whose edges are chosen appropriately. These methods may be subject to weak lines or signal-to-noise ratio. The band widths measured by Ali et al. are only 0.01μm, which is covered by only 14 pixels for their medium resolution($R \sim$1380). Jones et al.(1994) measured the gradient at 2.05 – 2.15μm and found that gradient is sensitive to temperature, for M dwarfs.

The strength of H_2O bands are measured as

$$H_2O \text{ index(blue)} = \text{gradient}(2.05 - 2.15\mu\text{m}) - \text{gradient}(2.15 - 2.29\mu\text{m}) \quad (4.1)$$

and

$$H_2O \text{ index(red)} = \text{gradient}(2.29 - 2.40\mu\text{m}) - \text{gradient}(2.15 - 2.29\mu\text{m}) \quad (4.2)$$

where gradient is the slope of the linear line which fits the continuum of the spectra in the wavelength region. Figure 8 shows measured H_2O indices at blue side of K band (2.05–2.15μm) taken by our UKIRT observation, as well as taken from literatures. For our UKIRT observation, the errors of the indices are less than 0.02, estimated from the deviation of the indices for individual exposure. All data except Kleimann & Hall (1986) were taken at the summit of Mauna Kea using UKIRT, giving us reliable data sets. The samples include not only dwarfs but also giants, to investigate the effect of surface gravity of the objects. The indices of either dwarfs or giants are sensitive to temperature less than 3500K. The indices of giants are bigger than those of dwarfs. Therefore, the H_2O index at blue side of K band is a good indicator for temperature of late type stars, although the index is also affected by the surface gravity of the objects. As discussed in the next section, the observed low-luminosity YSOs have gravities whose strength is between those of dwarfs and those of giants.

On the other hands, H_2O index at red side of K band is not good indicator of effective

temperature (Fig.9). This is probably due to contamination of the CO bands.

The effective temperature of the low-luminosity YSOs can be determined using the H_2O blue index. Because some portion of K band flux of YSOs comes from a circumstellar disk, veiling effect due to disk could reduce the H_2O blue index. Therefore the effective temperature of YSOs derived from the H_2O blue index may be lower limit. The deduced effective temperatures of the low-luminosity YSOs and the classical T Tauri stars are tabulated in Table 3.

4.3. Two-Dimensional Classification

Since the Na I and Ca I features (and Br γ for dwarfs and giants) are sensitive to effective temperatures and the CO feature to surface gravities, a plot of the equivalent widths of the atomic lines against that of the CO bandhead is useful to classify luminosity class. Because some YSOs show Br γ in emission, which may imply the chromospheric activities of the object, the sum of the equivalent widths of the Na and Ca features is taken as an atomic index, without including Br γ (Greene & Meyer 1995). The sum of the equivalent widths of CO(2,0) and CO(4,2) is taken as a CO equivalent width. CO(3,1) band is not included, because it contains another Na I feature (Kleinmann & Hall 1986).

Figure 10 shows the atomic index against the CO band equivalent width, where the low-luminosity YSOs, observed T Tauri stars and observed late-type dwarfs are plotted. The loci of giants and dwarfs are also shown by the solid lines (Greene & Meyer 1995). Almost all the low-luminosity YSOs as well as T Tauri stars lie between these two lines. Therefore the low-luminosity YSOs and classical T Tauri stars are classified as the same luminosity class, class IV.

4.4. Line Ratio of Metallic Lines

Meyer (1996) carried out H band spectroscopy of more than 100 MK standard stars. He proposed a system of line ratio of remarkable features for classifying stellar spectra. He used OH, CO, and Mg I feature in H band for cool stars and found that the line ratio method using these lines can estimate spectral type within ± 2 subclasses from K3–M5. The line ratio method can avoid not only the effect of metallicity but also the effect of continuum emission if selected is the features whose wavelengths are close with each other. The line ratio method requires relatively strong and high S/N lines from the point of view of error propagation.

The Na I, Ca I, and Mg I are tested as indices of effective temperature. Br γ cannot be used as discussed in the previous section. Also the CO band is not a good indicator for effective temperature.

Figure 11 shows the line ratio of Ca I to Na I for dwarfs and giants as a function of effective temperature. Although the scattering is relatively large, the ratio decreases as the temperature decreases. The surface gravity does not appear to affect significantly to this line ratio (Figure 20). Therefore this line ratio is a very sensitive indicator of effective temperature for low temperature.

In the figure the line ratio predicted by a model calculation is also shown. Although the model is simple and does not include precise treatments of the opacities of water vapor and dust grain, the resultant equivalent widths and the line ratio are consistent with measured equivalent widths and the line ratio (see the appendix for details on the model).

Figure 12 shows the line ratio of Mg I to Na I as a function of effective temperature. Since the Mg I line may be contaminated by unknown lines, the scattering is relatively large. Nevertheless, this line ratio can also be used as temperature scale.

For hotter objects, other metallic lines whose excitation potential is higher than Na

and Ca are available. In K band, Al I at 2.117μm could be useful for K type star, and Si at 2.136μm for G type star.

Chapter 5

Discussion

5.1. Effective Temperature

5.1.1. Uncertainties of Effective Temperature for Late Type Dwarfs

A number of synthetic spectra from model atmospheres have been calculated for comparison with observed spectra. However, there is an unaccountable discrepancy in effective temperatures for late-M dwarfs. The uncertainties can be found even in the spectral type. The spectral type of Gl406 is referred as M5.8 (Kleinmann & Hall 1986), M6 (Bessell 1991, Kirkpatrick et al. 1991, Legett 1992, Jones et al. 1996), or M8(Gliese & Jahreiss 1979, Arnaud et al. 1989). The effective temperature of M6 dwarfs is derived to be 2550K (Tokunaga 1998), 2800K (Bessell 1991, Legett 1992), or 2950K (Johnson 1966). Jones et al.(1994) and Jones et al.(1996) derived the effective temperature of Gl406 as 2670K from moderate resolution JHK spectroscopy, or as 2900K from J band spectra compared with synthetic spectra. Therefore, when the effective temperature is derived from the spectral features, the uncertainty in the effective temperature scale as much as $\pm$ 150K should be considered.

5.1.2. Effective Temperature of the Low-Luminosity YSOs

The effective temperatures of the observed low-luminosity YSOs are calculated using the Ca/Na line ratio, the Mg/Na line ratio, the Na line strength, the Ca line strength, and the H_2O gradient at blue side of the K band window. The each temperature derived from these temperature indices is tabulated in Table 3. For many cases except for the H_2O index, the temperature can be determined only its lower or higher value. The temperatures of the objects are estimated for the most objects combining Ca/Na ratio and H_2O index, because these indices are reliable one.

Table 3 also contains the effective temperatures of T Tauri stars using the near-infrared features. Optical spectroscopy revealed FP Tau as M5 (3120K; Cohen & Kuhi 1979), or M5.5 (Strom et al. 1989). An Effective temperature of M5.5 dwarf is 2900K (Bessell 1991) and that of M5.5 giant is 3360K (Fluks et al.1994). The effective temperature deduced from K band feature is 3100∼3400K, not inconsistent with the optical estimation.

Spectral types of DD Tau and GH Tau are estimated from optical spectroscopy as M1 (T_{eff} ∼3650K) and M2 (T_{eff} ∼3500K) respectively. The methods employed here can not determine such high temperature. As discussed above, Al and Si lines may be better temperature indicators for these high temperature objects.

5.2. Continuum Veiling Effects

The observed sample was selected by its intrinsic red color which is thought to be due to dust emission. This dust emission makes continuum veiling effect and dilutes the equivalent widths of stellar lines in the near-infrared wavelengths. This veiling effect can be expressed by

$$EW' = \frac{EW}{1 + r_\alpha} \tag{5.1}$$

where EW is the intrinsic equivalent width of the photospheric line, EW' is the measured equivalent width, and r_α is the veiling effect index at the band α.

The K band excess r_K for each source is calculated from the Na and Ca features (Table 4). The J band excess r_J is estimated from

$$-2.5\log(\frac{1 + r_J}{1 + r_K} = (J - K) - 0.17A_V - (J - K)_0 \tag{5.2}$$

where $(J - K)_0$ is the $J - K$ color of the dwarf whose effective temperature is the same as that of low-luminosity YSOs. Although the r_K and the r_J have large uncertainties, r_J is smaller than r_K for all low-luminosity YSOs.

5.3. Masses and Ages of the Low-Luminosity YSOs

The mass of the observed low-luminosity YSOs is estimated from recent evolutional tracks on the HR diagram.

5.3.1. Bolometric Luminosity

Because the J band emission arises primarily from the photosphere of class II objects (Bertout, Basri & Bouvier 1988), the bolometric luminosity of the observed YSOs is estimated from the J band luminosity and effective temperature deduced above. The J band luminosity of the low-luminosity YSOs tabulated in Itoh (1995) are corrected for interstellar extinction on the color-color diagram (Itoh et al 1996). Assuming that a circumstellar disk is optically thick and geometrically thin, fraction of emission arises from photoshere to total intrinsic J band luminosity of the YSO system is related to the inclination of the system as follows.

$$\frac{1 + \cos i}{2\alpha \cos i + (1 + \cos i)} \tag{5.3}$$

α is the ratio of disk lumnosity to photospheric luminosity at J band. If α is 0.5, as expected by the model, this value can vary between 0.67 ($r_J = 0.5$) and 1.0($r_J = 0.0$). Therefore 8/10 of the J band luminosity can be regarded to come from the photoshere in average. Also considered is the case that whole J band luminosity is due to the photosphere as a maximum, or half as a minimum.

The bolometric luminosity of the low-luminosity YSOs are estimated by the scaling late type dwarf spectra with the same effective temperature up to the intrinsic luminosity of the YSOs at J band.

5.3.2. HR Diagram

Recently, several groups develop and refine evolution tracks for low-mass stars, brown dwarfs, and even giant planets using new opacity tables. However, as the low temperature opacities contain a number of molecule and dust, how such low mass objects evolve at the pre-main stage is still an open question. Therefore, we use several evolution tracks for comparison with the observational data. On the other hand, evolutional tracks for more massive object ($M \geq 0.5 M_\odot$) are well consistent each other (e.g., D'Antona & Mazzitelli 1994).

Figure 13 is the HR diagram of the classical T Tauri stars listed in Strom et al.(1989) with one set of the evolution tracks by D'Antona & Mazzitelli. From this figure one can deduce that mass of T Tauri stars is $0.3 \sim 2 M_\odot$ and their age is 10^5 year $\sim 3 \times 10^7$ year. These values are little subject to evolutional track models.

Figures 14 show the HR diagrams of the low-luminosity YSOs. Overlaid are the evolutional tracks of four sets of D'Antona & Mazzitelli (1994), Chabrier & Baraffe (1997), Burrows et al.(1997), Nelson et al.(1993), and Swenson. These models cover the objects with different masses with each other; D'Antona & Mazzitelli and Swenson for low mass

stars, Chabrier & Baraffe and Nelson et al. for very low-mass stars, and Burrows et al. for brown dwarfs and giant planets. All HR diagrams strongly indicate that the low-luminosity YSOs are indeed VLM objects in pre-main sequence stage.

5.3.3. Mass and Age of Low-Luminosity YSOs

Mass and age for individual low-luminosity YSOs can be estimated from the HR diagrams with evolutional tracks. The derived mass and age are tabulated in Table5. Most of the low-luminosity YSOs are very low-mass YSOs (typically $0.1 \sim 0.2 M_\odot$). Especially, ITG 40 may be a young brown dwarf. The uncertainties in the mass are about factor 2, and those in the age are about factor 5 for the low-luminosity YSOs as shown in the figures.

Both classical T Tauri stars and the low-luminosity YSOs have near-infrared excess, implying the existence of circumstellar disks. The age of these objects indicates survival time of circumstellar disk, and it is interesting to ask whether the mass of the central object affects the evolution of circumstellar disk. However, the relationship between the object mass and its age is still unknown. Figure 15 shows this relation using D'Antona & Mazzitelli model with the Alexander opacities and CM convection. This figure suggests that two samples are definitely different with age. However, from the model with Kurucz opacities the age of the most low-luminosity YSOs is deduced to be less than 10^5 year. Therefore, mass – age relation depends strongly on evolutional tracks.

5.3.4. Mass Estimation from Photometry vs Spectroscopy

Many near-infrared imaging surveys have been carried out toward nearby star forming regions (e.g. Itoh et al.1996). Although their motivations are, for many cases, to construct initial mass function, imaging observations can supply only luminosity of the objects, not mass. Many authors, therefore, should assume parameters of YSOs, such as age, coeval star

formation, to estimate object mass.

The mass of the object estimated from the spectroscopic observation is shown in the J luminosity function of the Class II objects in Heiles Cloud 2 (Fig. 16). In the figure the mass of the known T Tauri star, the objects whose mass cannot be estimated by Br γ absorption, high effective temperature, and low S/N are also plotted. This figure indicates that lower luminosity YSOs have lower mass.

The mass-luminosity relation of the low-luminosity YSOs are derived from our spectroscopic observation. The relation is shown in Figure 17, where also shown are the mass-luminosity relations for three ages calculated from Alexander-CM model in D'Antona & Mazzitelli with the bolometric temperature of Bessell (1991). The figure shows that all the ages of the low-luminosity YSOs are distributed within one order of magnitude and the mass-luminosity relation for the low-luminosity YSOs appears to be established.

It implies that the mass estimated from the photometric observation alone is in agreement with the mass estimated from the spectroscopic observation. The relation between these two estimated mass is shown in Figure 18 in logarithmic scale. The error bars for photometric mass come from the uncertainty of the age of the object, which is represented by the age distribution of classical T Tauri stars (Itoh 1995). It is known that this photometric mass estimation method can derive the mass of classical T Tauri stars estimated from optical spectroscopy with factor of 2 in mass. Figure 18 indicates that this method is valid even for the low-luminosity YSOs. The J band luminosity function of the class II objects in Heiles cloud 2 shows an increase in shape down to about 14.2 mag which is the completeness limit of the survey. Therefore it can be concluded that the mass function of the class II objects in Heiles cloud 2 increases toward brown dwarf regime.

Chapter 6

Conclusions

We have carried out K band spectroscopic observations to estimate the mass and age of the low-luminosity YSO candidates detected by the imaging survey of a part of the Taurus molecular cloud (Heiles Cloud 2).

1. Out of 21 objects, 11 objects have Br γ in emission. We conclude that these are YSOs.
2. Compiling near-infrared spectra of dwarfs and giants taken by us as well as those in literature, the line ratio of calcium to sodium turns out to be a good indicator of the effective temperature for M type objects.
3. The spectral gradient between 2.05μm and 2.15μm due to H_2O band absorption also has a good correlation with effective temperature of late M type objects.
4. The effective temperatures of classical T Tauri stars deduced from the K band features are in good agreement with those derived from optical spectroscopy.
5. The effective temperatures of the low-luminosity YSOs are determined. These objects are very cool (T_{eff} ~3000K) YSOs.
6. The mass of these low-luminosity YSOs is estimated from HR diagram with recent evolutional tracks. Most of these objects are very low-mass (typically 0.1~0.2$M_\odot$)

YSOs, and one object may be a young brown dwarf.

7. The age of these low-luminosity YSOs appears to be 10^5 year or 10^7 year. However, the deduced age depends on evolutional track models.

8. The mass of the low-luminosity YSOs estimated from the photometric observation is in agreement with the mass derived from the spectroscopic observation.

9. Since the luminosity function of class II objects in Heiles Cloud 2 increases toward low luminosity, the mass function does not appear to have any turnover down to substellar regime.

Chapter 7

Appendix — Model Calculations of the Metallic Line Strengths

In order to understand behaviors of spectral features, we have calculated equivalent widths of metallic lines as functions of temperature, metallicity and surface gravity.

7.1. Opacity Table

The precise opacity table and convection model are need for the calculation of stellar structure, stellar evolution, and spectra synthesis. The modern opacity tables contain water opacities of water and molecules and become huge database (e.g. OPAL, HITRAN). Usage of such databases, however, demands a complicate program and a high performance computer, which are beyond the scope of this thesis. Here, we only use the Rossland mean opacities computed by Alexander, Johnson & Rypma (1983). For T_{eff} <5000K, an analytic fit of Alexander's opacities presented in Nelson et al.(1993) is used.

7.2. Stellar Atmosphere Model

The model of the stellar atmosphere is adopted from Cayrel & Jugaku (1963), which assumed local thermodynamic equilibrium. The numerical integration of a model atmosphere structure

$$d\tau = \rho\kappa(T,\rho)dz \tag{7.1}$$

$$T = T_{eff} f(\tau) \tag{7.2}$$

$$\tag{7.3}$$

was performed, in which τ is optical depth, κ is the Rossland mean opacity, and $f(\tau)$ is the function of the temperature with optical depth for radiative zone (Cayrel & Jugaku 1963).

7.3. Equivalent Width of Weak Atomic Line

The reduced equivalent widths for sufficiently weak lines $(\frac{W}{\lambda})_{wk}$ can be given by

$$\log(\frac{W}{\lambda})_{wk} = \log\frac{N_E}{N_H} + \log gf + \log\Gamma_{\lambda,\mu}(\chi) \tag{7.4}$$

with

$$\Gamma_{\lambda,\mu}(\chi) = \frac{\pi e^2}{mc^2}\lambda\int_0^\infty P(\tau)g_\lambda(\tau,\mu)/\mu \tag{7.5}$$

where

$$P(\tau) = \frac{n_r}{\sum n_r}\frac{1}{u_r(T)}10^{-\chi_{r,s}\theta}(1-e^{-hc/\lambda kT})\frac{1}{\mu_H m_H}\frac{1}{\kappa} \tag{7.6}$$

and N_E is number of the element, N_H is number of hydrogen, gf values are taken from Kurucz CD-ROM (No.23, http://leanda.pmp.uni-hannover.de/projekte/kurucz/sekur.html). μ is cosine of the inclination angle to the radial direction, χ is the lower excitation potential at r-th ionized stage, $\theta = 5040/T$, κ is absorption coefficient ([cm^2/gr]), and μ_H is the mean molecular weight defined by

$$\mu_H = \sum_i \mu_i N_i/N_H \tag{7.7}$$

$g_\lambda(\tau,\mu)$ is the weighting function, which is represented by

$$g_\lambda(\tau,\mu) = \int_\tau^\infty (dB_\lambda/dt)e^{-t/\mu}dt/\int_0^\infty B_\lambda(t)e^{-t/\mu}dt/\mu \tag{7.8}$$

where $B_\lambda(t)$ is the blackbody function.

$u_r(T)$ is the partition function. Irwin (1981) presented polynomial partition function approximations of 344 atomic and molecular species for a temperature range from 1000 to 16000 K. The absolute errors in the approximations are estimated to be less than 0.1% of the ground state statistical weight.

7.4. Equivalent Width for General Case

For general case,

$$\Gamma_{\lambda,\mu}(\chi) = \frac{\pi e^2}{mc^2}\lambda\int_0^\infty P(\tau)\Psi(Y/\mu,\alpha)g_\lambda(\tau,\mu)/\mu \tag{7.9}$$

where

$$\Psi(Y/\mu,\alpha) = \frac{2}{\sqrt{\pi}}\int_0^\infty H(\alpha,v)e^{-H(\alpha,v)Y/\mu}dv \tag{7.10}$$

$\Psi(Y/\mu,\alpha)$ is the saturation function, and $Y(\tau)$ is defined as

$$\int_0^\tau \frac{\kappa_\lambda}{\kappa}dt = Y(\tau)H(\alpha,v) \tag{7.11}$$

Broadening Function

The line broadening function $H(\alpha,v)$ is given by the following expression.

$$H(\alpha,v) = \frac{\alpha}{\pi}\int_{-\infty}^{+\infty}\frac{e^{y^2}}{\alpha^2+(v-y)^2}dy \tag{7.12}$$

For small values of α, the Taylor series of $H(\alpha,v)$ can be written (Harris 1948) as

$$H(\alpha,v) = H_0(v) + \alpha H_1(v) + \alpha^2 H_2(v) + \alpha^3 H_3(v) + \alpha^4 H_4(v) + ... \tag{7.13}$$

where

$$H_0(v) = e^{-v^2} \tag{7.14}$$

$$H_1(v) = -\frac{2}{\sqrt{\pi}}[1 - 2vF(v)] \tag{7.15}$$

$$H_2(v) = (1 - 2v^2)e^{-v^2} \tag{7.16}$$

$$H_3(v) = -\frac{2}{\sqrt{\pi}}[\frac{2}{3}(1 - v^2) - 2v(1 - \frac{2}{3}v^2)F(v)] \tag{7.17}$$

$$H_4(v) = (\frac{1}{2} - 2v^2 + \frac{2}{3}v^4)e^{-v^2} \tag{7.18}$$

here

$$F(v) = e^{-v^2}\int_0^v e^{t^2}dt \tag{7.19}$$

v and α are represented as

$$v = \frac{\lambda - \lambda_0}{\Delta\lambda_D} \tag{7.20}$$

$$\alpha = \frac{\lambda^2\gamma}{4\pi c\Delta\lambda_D} \tag{7.21}$$

where

$$\gamma = \gamma_u + \gamma_l + \gamma_{coll} \tag{7.22}$$

and

$$\Delta\lambda_D = \frac{\lambda}{c}v_D \tag{7.23}$$

$$v_D = \sqrt{\frac{2RT}{\mu} + \xi^2_{micro}} \tag{7.24}$$

R is the gas constant, and ξ_{micro} is velocity of microturbulence. From high dispersion spectroscopy (Padgett 1996), ξ_{micro} is estimated to be 1.6 km/s for T Tauri stars in the Taurus molecular cloud.

γ_l is natural broadening by Lorenz theory, and given by

$$\gamma_l = \frac{8\pi^2}{3}\frac{e^2}{mc}\frac{1}{\lambda_0^2} \tag{7.25}$$

γ_u is natural broadening by quantum theory, which is given by

$$\gamma_u = \sum A_{lu} = \frac{1}{T_U} \tag{7.26}$$

where A_{lu} is the Einstein transition probability for spontaneous emission. The A_{lu} values for many spices are tabulated in Kurucz CD-ROM No.23.

γ_{coll} is Van der Waals broadening for neutral atoms, and represented as

$$\gamma_{coll}(V.d.W.) = 17.0C^{2/5}v^{3/5}N \tag{7.27}$$

where

$$C = 1.61 \times 10^{-33}(\frac{13.5Z}{\chi_r - \chi_{r,s}})^2 \tag{7.28}$$

χ_r is the ionized potential, and $\chi_{r,s}$ is the excitation potential.

7.5. Equivalent Width of Atomic Lines

Padgett (1996) derived metallicities for nearby star forming regions including Taurus by high-resolution echelle spectra of T Tauri stars, and they concluded that [Fe/H] is approximately solar. Therefore solar abundance is assumed in our calculation. The derived equivalent widths are compared to the high-resolution near-infrared solar intensity atlas of Livingston & Wallace (1991) and the calculated equivalent widths are adjusted. The resultant equivalent width for Na I, Ca I, and Mg I are shown in Figure 19, overlaid with the predicted line strengths for [Fe/H]=0 by Ali et al.(1996) and the measurement equivalent widths for nearby dwarfs (Ali et al. 1996). For lower temperature stars, especially for T_{eff} <3500K, water vapor is the most important opacity source at infrared wavelength (Allard et al. 1994). Although the current simple model include only the approximate treatment of the opacity of water vapor and dust grain, the resultant equivalent widths are consistent with the measured line strength. Especially, the model is in agreement with the fact that the measured equivalent width of the Na I line increases well below 3500K while that of the Ca I line turns over at 3500K.

The Ca/Na line ratios are shown in Figure 20 with variant metallicities and surface gravities. The deviation of the line ratio due to metallicity and gravity is not significant compared with observational uncertainties.

Table 1. The observed objects.

Object	Object Type	m_K[a] [mag]	T_{exp} [sec.]	S/N_{Ali}	S/N_{obj}	S/N_{std}	S/N_{est}
ITG 2	low-luminosity YSO	10.05	960	97	69	168	64
ITG 4	low-luminosity YSO	11.05	1920	88	90	162	79
ITG 5	low-luminosity YSO	8.31	96	165	88	139	74
ITG 6	low-luminosity YSO	10.37	480	63	87	203	80
ITG 13	low-luminosity YSO	11.69	1200	252	64	111	55
ITG 15	low-luminosity YSO	9.02	288	66	77	146	68
ITG 17	low-luminosity YSO	10.37	960	54	32	140	31
ITG 18	low-luminosity YSO	10.27	960	80	79	145	69
ITG 21	low-luminosity YSO	10.83	960	65	73	149	66
ITG 24	low-luminosity YSO	13.05	2160	55	44	153	42
ITG 25	low-luminosity YSO	8.97	480	140	97	121	76
ITG 27	low-luminosity YSO	8.46	288	130	101	122	78
ITG 28	low-luminosity YSO	11.87	1920	170	50	182	48
ITG 29	low-luminosity YSO	10.74	960	180	65	120	57
ITG 33	low-luminosity YSO	11.50	1920	70	55	133	51
ITG 36	low-luminosity YSO	11.01	1920	130	53	111	48
ITG 39	low-luminosity YSO	11.80	1440	108	60	164	56
ITG 40	low-luminosity YSO	11.47	1440	33	32	118	31
ITG 41	low-luminosity YSO	9.72	480	125	96	154	81
ITG 43	low-luminosity YSO	11.24	1920	140	62	149	57
ITG 46	low-luminosity YSO	11.01	1440	92	68	181	64

Table 1—Continued

Object	Object Type	m_K[a] [mag]	T_{exp} [sec.]	S/N_{All}	S/N_{obj}	S/N_{std}	S/N_{ext}
DD Tau	T Tauri(M1)	7.97	192	150	96	139	79
GH Tau	T Tauri(M2)	7.86	192	135	130	141	96
FP Tau	T Tauri(M5.5)	8.84	480	113	146	142	102
IRAS04365+2535	proto star	10.7	1200		159	140	105
Gl96	Dwarf (M1.5)	5.59	12.12	74	108	171	91
Gl85.1	Dwarf (M3)	7.51	480	150	311	140	128
Gl806	Dwarf (M3)	6.54	12.12	136	94	23	22
Gl12	Dwarf (M5)	7.31	96	113	9	98	9
Gl406	Dwarf (M6)	6.23	28.8	110	64	192	61
LHS2397a	Dwarf (M8)	10.77	1440	116	89	94	65
BRI0021-214	Dwarf (M9.5)	10.64	768	74			

[a]Apparent K magnitudes for Strom et al. (1989) for T Tauri stars, Johnson & Wright (1983) for Gliese stars, and Myers et al.(1987) for the IRAS source.

Table 2. Equivalent widths and gradients of the line/band of the objects.

Object	Brγ [Å]	Na [Å]	Ca [Å]	Mg [Å]	CO(2-0) [Å]	CO(4-2) [Å]	H_2O(blue)	H_2O(red)
ITG 2	flat	2.18±0.39	1.00±0.16	1.66±0.21	6.20	7.80	0.50	3.31
ITG 4	6.80	...	...	1.60±0.65?	...	...	0.08	0.11
ITG 5	4.24	0.80±0.26	1.44±0.28	1.14±0.33	2.71	1.97	-0.09	-0.40
ITG 6	-2.25	0.98±0.23	0.53±0.22	1.02±0.30	2.30	1.97	0.46	-0.70
ITG 13	14.08	0.25±0.25	...	1.18	...	...	-0.07	0.14
ITG 15	-0.79	3.29±1.00	4.12±1.24	1.06±0.24	6.73	10.39	0.53	-1.21
ITG 17	-0.5?	1.96±0.37	2.48±0.17	1.30±0.73	6.79	10.02	0.42	-2.00
ITG 18	8.25	...	...	0.7±0.7	...	...	0.06	0.14
ITG 21	-3.8	2.22±0.78	2.31±0.44	0.62±0.18	5.11	8.50	0.47	-2.12
ITG 24	6.6	...	0.58?	1.9?	...	...	-0.25	0.37
ITG 25	-5.3	1.94±0.51	2.54±0.50	2.27±1.50	3.72	5.43	0.24	-0.61
ITG 27	abs.?	1.36±0.64	1.33±0.70	2.57±1.41	7.87	8.50	-0.15	0.03
ITG 28	5.5	0.75	...	1.7?	...	...	-0.22	0.49
ITG 29	11.5	0.47	...	0.93	...	...	-0.07	0.20
ITG 33	-2.83	3.68±0.43	3.76±0.37	1.97±0.25	6.16	8.56	0.19	-1.18
ITG 36	5.1	1.20±0.43	1.26±0.33	2.04±0.41	...	...	-0.08	0.06
ITG 39	7.4	...	...	2.22	...	...	-0.09	0.37
ITG 40	-1.7?	4.15±1.00	1.78±0.53?	2.02±0.45	4.95?	10.76	0.68	-1.54
ITG 41	flat	2.31±0.50	2.08±0.56	1.49±0.56	3.43	6.53	0.30	-0.46
ITG 43	7.7	...	...	...	...	...	-0.17	0.43
ITG 46	-0.6?	1.46±0.50	1.34±0.33	1.96±0.49	11.13	13.69	-0.07	-0.18

Table 2—Continued

Object	Brγ [Å]	Na [Å]	Ca [Å]	Mg [Å]	CO(2-0) [Å]	CO(4-2) [Å]	H_2O(blue)	H_2O(red)
DD Tau	-2.5±0.3	1.99±0.42	1.84±0.25	0.93±0.04	3.21	4.93	0.06	-0.72
GH Tau	-0.6	2.91±0.46	2.81±0.48	0.92±0.19	5.01	6.92	-0.05	-0.10
FP Tau	-1.02±0.46	3.35±0.69	3.47±0.38	1.37±0.24	6.91	8.27	0.48	-0.47
Gl96	-1.8	4.78±1.18	4.24±0.24	1.02	6.67	7.19	-0.03	0.09
Gl85.1	-1.04	2.60±0.60	1.97±0.39	0.64±0.34	3.74	5.11	-0.00	0.31
Gl806	-0.4	4.08±0.34	3.97±0.36	0.52±0.11	4.88	7.39	-0.06	0.25
Gl12	emission?	4.39±0.34	3.37±0.27	0.35±0.35?	···	···	0.28	-0.77
Gl406	-1.72	7.67±0.75	1.65±0.15	0.82±0.15	8.13	7.96	0.52	-1.84
LHS2397a	···	4.98±0.31	0.39±0.07	0.98±0.33	14.32	13.54	2.06	-1.19
BRI0021-214	flat	2.87±0.52	1.75±0.82	1.64±0.48	11.54	10.59	1.80	-1.42
Black Body[a]						-0.20	0.22	

[a]T=3000K

Table 3. Effective temperatures ([K]) of the low-luminosity YSOs and T Tauri stars.

Object	T_{eff}(Ca/Na)[a]	T_{eff}(Mg/Na)[b]	T_{eff}(Na)[c]	T_{eff}(Ca)[d]	T_{eff}(H_2O)[e]	T_{eff}[f]
ITG 2	2300~3400	···	<5200	···	2800~3400	2800~3400
ITG 6	2300~3700	···	···	···	2800~3400	2800~3400
ITG 15	>3000	>2850	<4800	<4800	2800~3400	3000~3400
ITG 17	···	>3250	···	···	2900~3450	2900~3450
ITG 21	>2900	>3000	···	···	2800~3400	2900~3400
ITG 25	>3250	···	···	···	3000~3600	3250~3600
ITG 27	>2500	···	···	···	>3300	>2500
ITG 33	>3200	>3450	<4200	<4600	>3200	3200~4200
ITG 40	2000~3400	>3200	<4200	···	2500~3300	2500~3300
ITG 41	>2750	>3400	···	···	3000~3600	3000~3600
ITG 46	>2700	···	···	···	>3300	>2700
DD Tau	>2900	>3350	···	···	>3300	>3300
GH Tau	>2900	>2900	<4700	···	>3300	3300~4700
FP Tau	>3100	>3100	<4600	<5000	2800~3400	3100~3400

[a]T_{eff} estimated from the Ca/Na line ratio.

[b]T_{eff} estimated from the Mg/Na line ratio.

[c]T_{eff} estimated from the the equivalent widths of the Na line. Because YSOs are subject to continuum emission and the strength of the line increases with low temperature, the upper limit of the effective temperature can be estimated.

[d]T_{eff} estimated from the the equivalent widths of the Ca line.

[e]T_{eff} estimated from H_2O index at blue side of K band.

[f]T_{eff} estimated from the Ca/Na ratio and the H_2O index.

Table 4. Near-infrared excesses of the low-luminosity YSOs.

Object	r_K(Na)	r_K(Ca)	r_J(Na)	r_J(Ca)
ITG 2	$1.94^{+0.64}_{-0.45}$	$2.45^{+0.66}_{-0.48}$	$0.85^{+0.40}_{-0.28}$	$1.17^{+0.41}_{-0.30}$
ITG 6	$5.67^{+2.05}_{-1.27}$	$5.67^{+5.69}_{-1.95}$	$1.93^{+0.90}_{-0.56}$	$1.93^{+2.06}_{-0.86}$
ITG 15	$0.89^{+0.82}_{-0.44}$	$-0.03^{+0.42}_{-0.22}$	$0.11^{+0.49}_{-0.26}$	$-0.43^{+0.25}_{-0.13}$
ITG 17	$2.23^{+0.75}_{-0.51}$	$0.54^{+0.11}_{-0.10}$	$0.51^{+0.35}_{-0.24}$	$-0.28^{+0.05}_{-0.05}$
ITG 21	$1.94^{+1.60}_{-0.77}$	$0.61^{+0.38}_{-0.26}$	$0.60^{+0.87}_{-0.41}$	$-0.13^{+0.21}_{-0.41}$
ITG 25	$1.70^{+0.97}_{-0.56}$	$1.04^{+0.50}_{-0.34}$	$-0.02^{+0.35}_{-0.20}$	$-0.26^{+0.18}_{-0.12}$
ITG 27	...	...	...	...
ITG 33	$0.22^{+0.16}_{-0.13}$	$0.28^{+0.14}_{-0.11}$	$-0.60^{+0.05}_{-0.04}$	$-0.58^{+0.05}_{-0.04}$
ITG 40	$0.72^{+0.55}_{-0.33}$	$0.47^{+0.62}_{-0.34}$	$-0.52^{+0.15}_{-0.09}$	$-0.59^{+0.17}_{-0.09}$
ITG 41	$1.56^{+0.71}_{-0.46}$	$1.86^{+1.05}_{-0.61}$	$0.16^{+0.32}_{-0.21}$	$0.30^{+0.48}_{-0.28}$
ITG 46	...	...	...	...

Table 5. Mass ([$M_\odot$]) and age ([yr]) of the low-luminosity YSOs.

Object		AlexCM	AlexMLT	KurCM	KurMLT	CB	Burrows	Nelson	Swenson
ITG 2	mass	0.11	0.12	<0.10	<0.10	0.15	>0.07	0.09	0.37
	age	1.5×10^6	2×10^6	$<1\times10^5$	$<1\times10^5$	3×10^6	...	9×10^5	1×10^7
ITG 6	mass	0.09	0.10	<0.10	<0.10	0.11	>0.07	0.11	0.36
	age	3×10^6	3×10^6	$<1\times10^5$	$<1\times10^5$	5×10^6	...	3×10^6	3×10^7
ITG 15	mass	0.17	0.16	<0.10	<0.10	0.22	>0.07	0.12	0.37
	age	1.5×10^6	2×10^6	$<1\times10^5$	$<1\times10^5$	$<2\times10^6$	...	4×10^5	5×10^6
ITG 17	mass	0.12	0.12	<0.10	<0.10	0.15	>0.07	0.13	0.42
	age	3×10^6	4×10^6	$<1\times10^5$	$<1\times10^5$	7×10^6	...	6×10^6	6×10^7
ITG 21	mass	0.11	0.12	<0.10	<0.10	0.14	>0.07	0.12	0.40
	age	3×10^6	3×10^6	$<1\times10^5$	$<1\times10^5$	6×10^6	...	4×10^6	4×10^6
ITG 25	mass	0.25	0.28	0.09	<0.10	0.35	>0.07	0.2	0.55
	age	2×10^6	2.5×10^6	2×10^5	1×10^5?	5×10^6	...	8×10^5	8×10^6
ITG 27	mass	...	...	...	...	...	...	...	...
	age	...	...	...	...	...	...	...	...
ITG 33	mass	...	...	0.20	0.22	...	>0.07	>0.3	...
	age	$>1\times10^7$	$>1\times10^7$	$>1\times10^7$	$>1\times10^7$	$>3\times10^7$	...	$>1\times10^7$	...
ITG 40	mass	<0.10	<0.10	<0.10	<0.10	<0.075	0.065	0.05	0.15
	age	2×10^6?	2×10^6?	$<1\times10^5$	$<1\times10^5$	$<3\times10^6$	3×10^6	9×10^5	1.5×10^7
ITG 41	mass	0.18	0.2	<0.10	<0.10	0.28	>0.07	0.16	0.55
	age	2.5×10^6	2.8×10^6	$<1\times10^5$	$<1\times10^5$	6×10^6	...	2×10^6	2×10^7
ITG 46	mass	...	...	...	...	...	...	...	...
	age	...	...	...	...	...	...	...	...

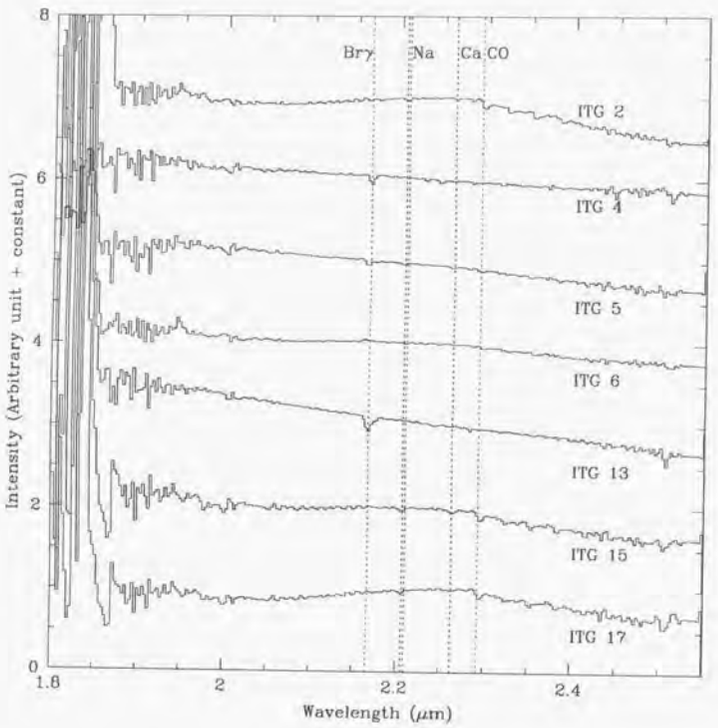

Fig. 1.— K band spectra of low-luminosity YSO candidates.

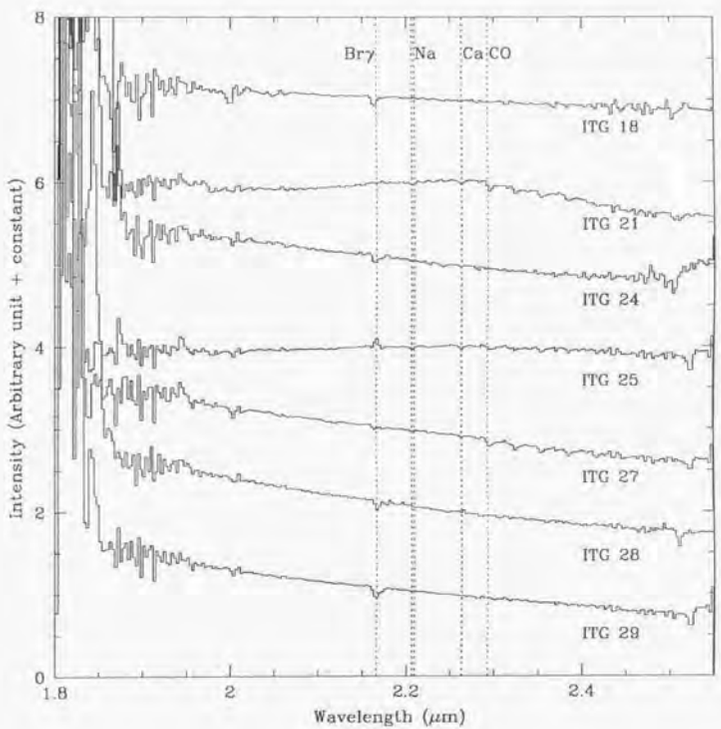

Fig. 1 (cont.).— K band spectra of low-luminosity YSO candidates.

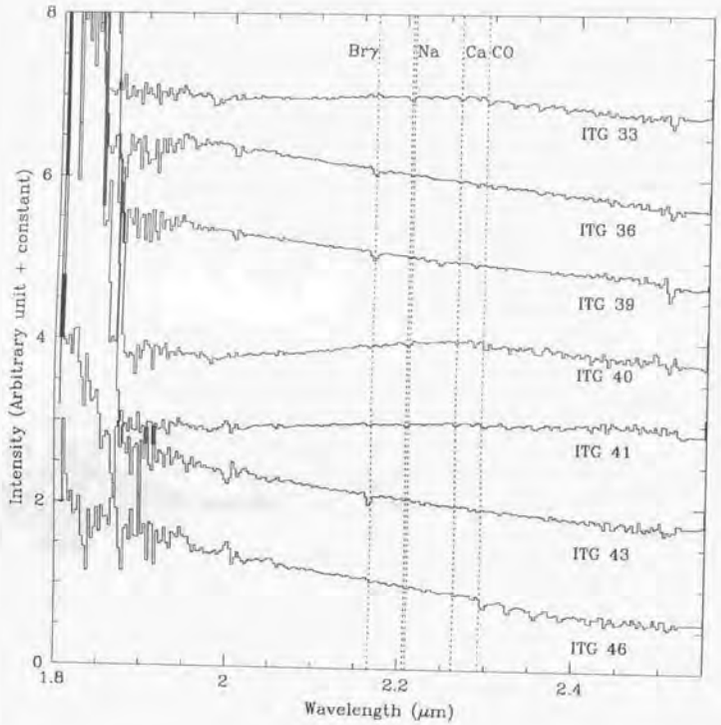

Fig. 1 (cont.).— K band spectra of low-luminosity YSO candidates.

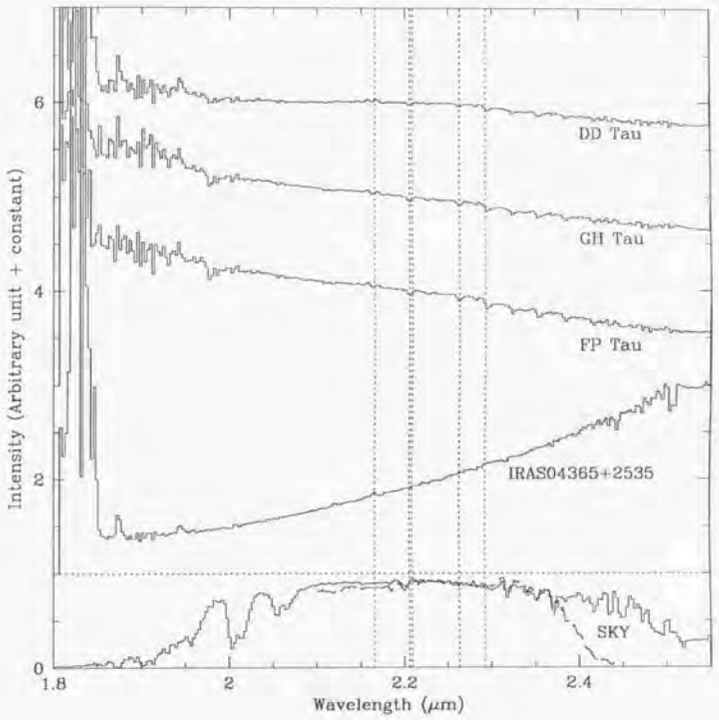

Fig. 2.— K band spectra of T Tauri stars. The spectra of a standard star with nterpolated Brγ line is shown at the bottom as an indication of the sky transmittance pattern. The solid line is the spectrum taken at Mauna Kea, while the dashed line at Okayama as a comparison. Note that both line are normalized to 0.9 in average at $\lambda = 2.2\mu$m $\sim 2.3\mu$m. Therefore the figure does not reflect the difference of the transmittance of the atmosphere between Mauna Kea and Okayama even at 2.2μm$\sim 2.3\mu$m. The wavelengths shorter than 2.1μm and longer than 2.45μm are out of range in the Okayama observation.

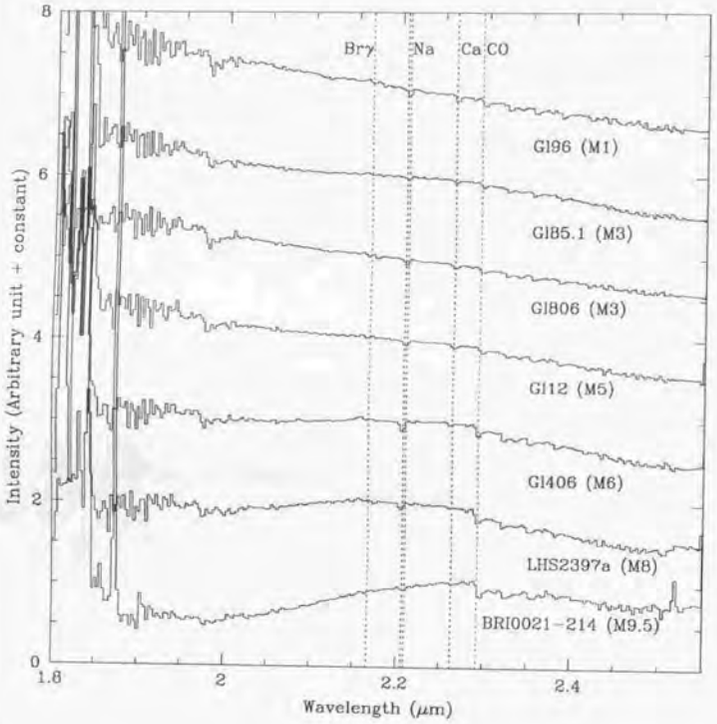

Fig. 3.— K band spectra of nearby late-type dwarfs.

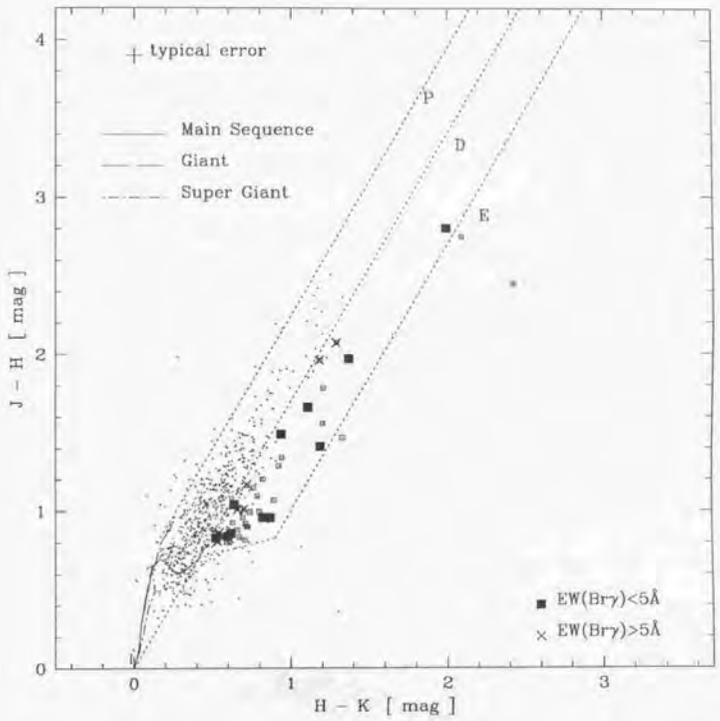

Fig. 4.— The color-color diagram for Heiles Cloud 2. The observed objects with absorption less than 5 $\AA$ or with emission in Brγ line are denoted by the filled squares. The observed object with absorption more than 5 $\AA$ in Brγ line are shown by the crosses. The other YSO candidates identified by the previous near-infrared survey (Itoh 1995) are shown by the small open squares. Field stars are shown by the dots.

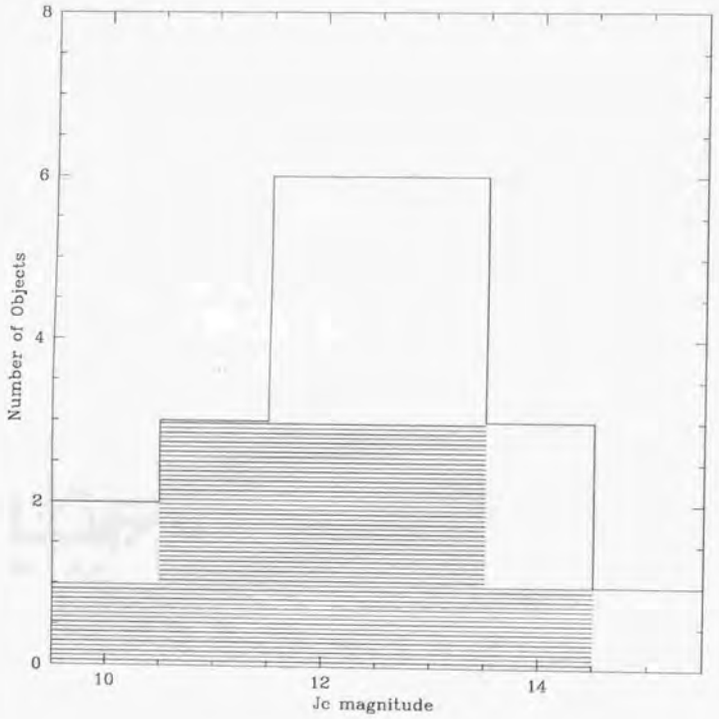

Fig. 5.— Histogram of the objects with Brγ absorption (no-shaded bar) and the objects without absorption or with emission (shaded bar).

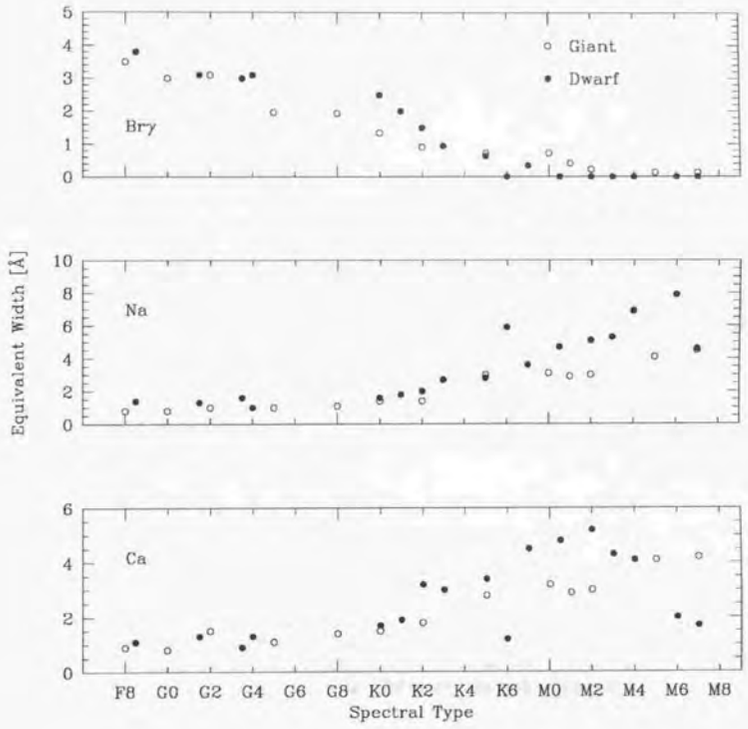

Fig. 6.— Equivalent widths of the prominent K band absorption features. Data from Luhman et al.(1997)

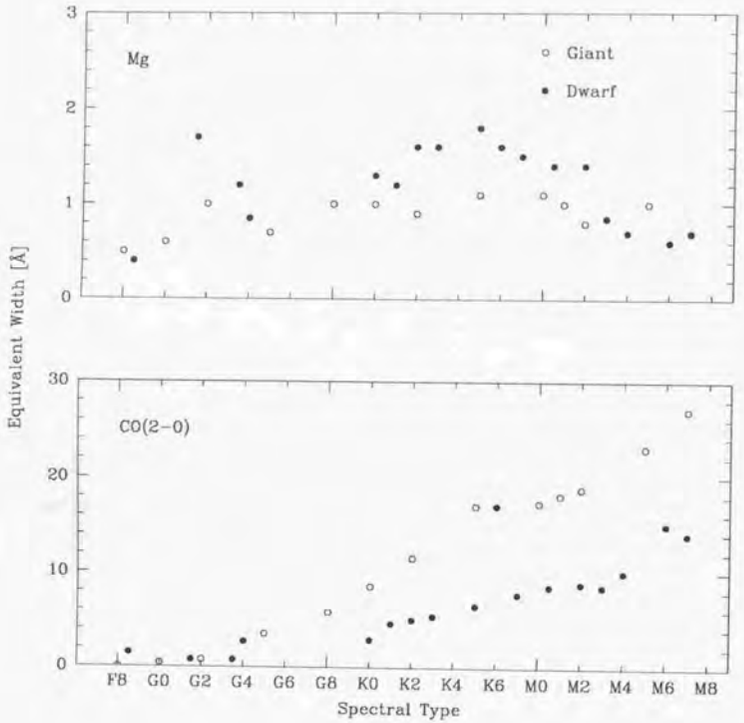

Fig. 6 (cont.).— Equivalent widths of the prominent K band absorption features. Data from Luhman et al.(1997)

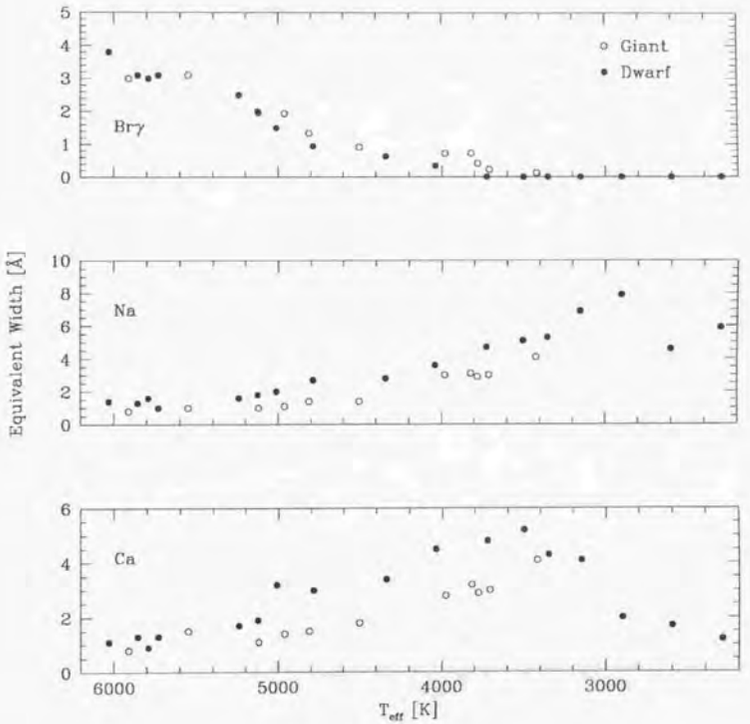

Fig. 7.— Equivalent width versus T_{eff}.

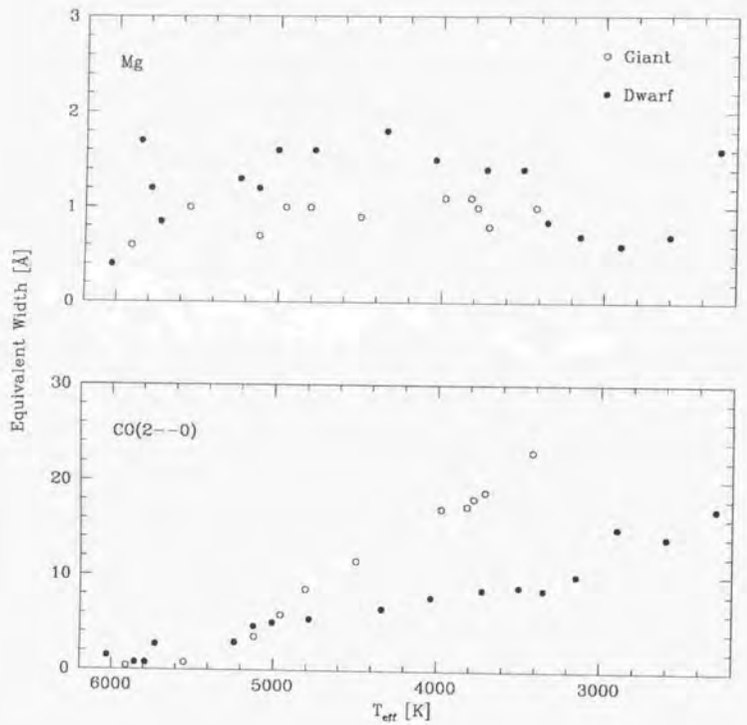

Fig. 7 (cont.).— Equivalent width versus T_{eff}.

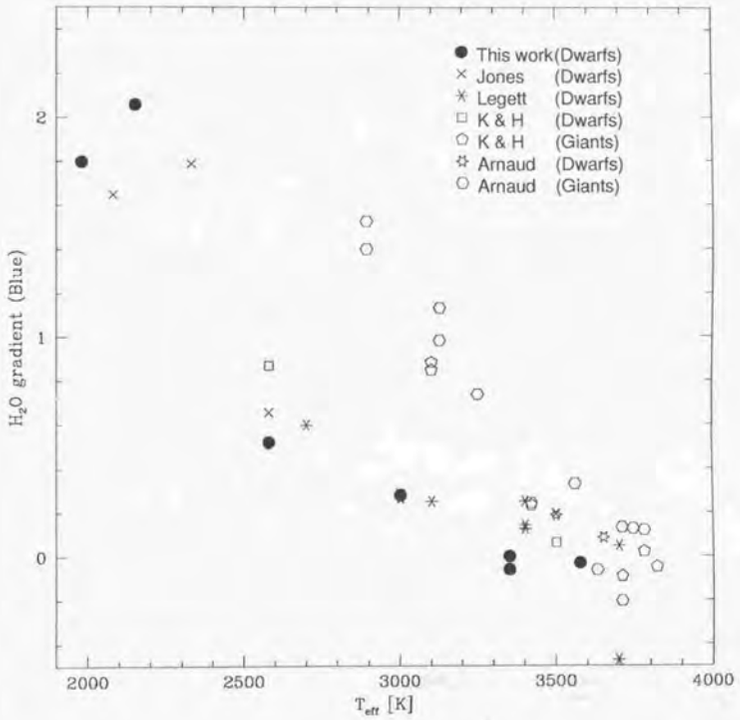

Fig. 8.— H_2O gradient at the blue side of the K band window versus effective temperature.

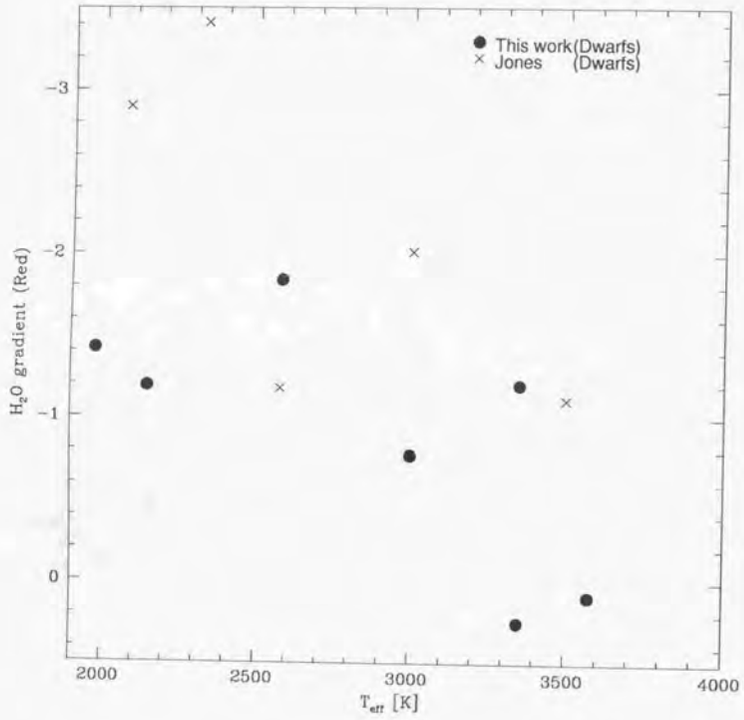

Fig. 9.— H_2O gradient at the red side of the K band window versus of effective temperature.

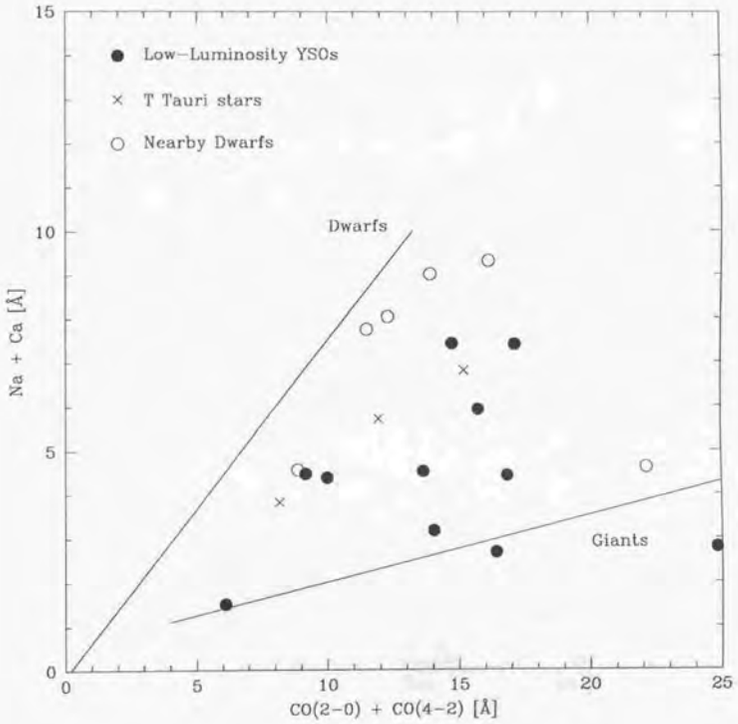

Fig. 10.— Metallic line index versus CO band head index.

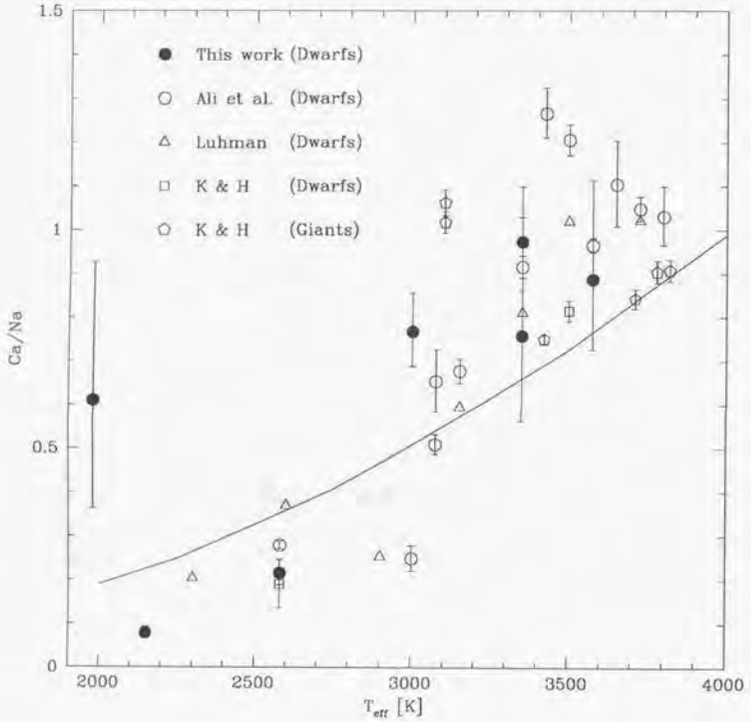

Fig. 11.— Ratio of calcium to sodium versus effective temperature. The line ratio calculated by the model is shown by the solid line.

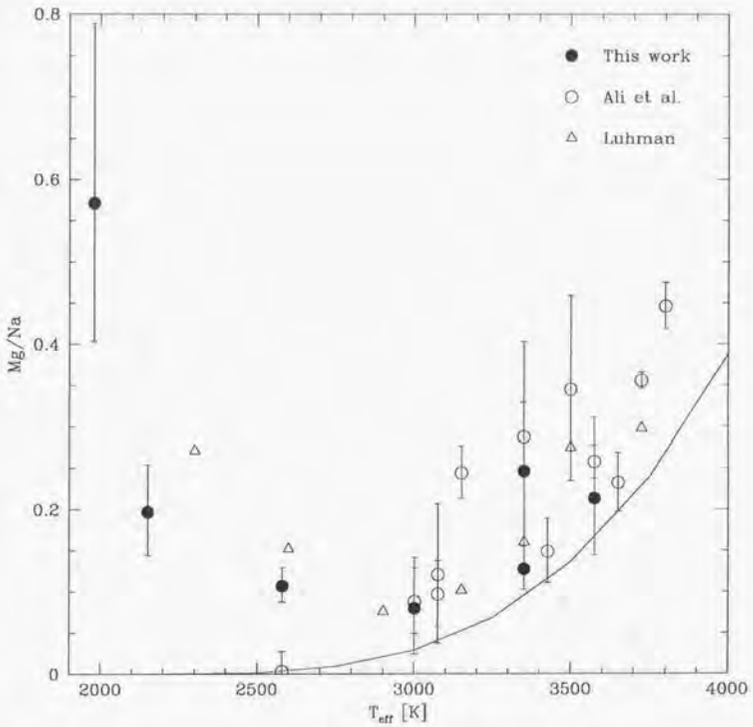

Fig. 12.— Ratio of magnesium to sodium versus of effective temperature.

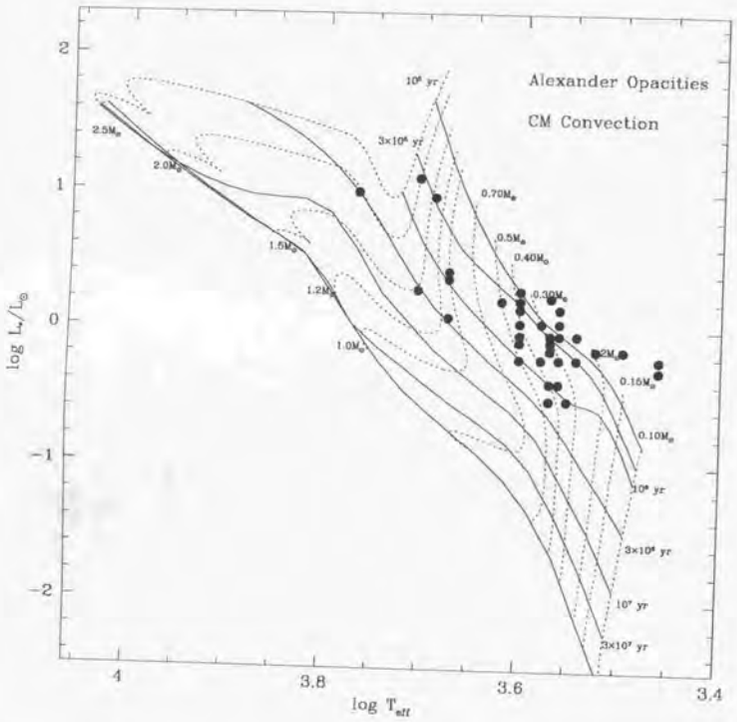

Fig. 13.— HR diagram of classical T Tauri stars with the evolutional track of D'Antona & Mazzitelli (1994) overlaid.

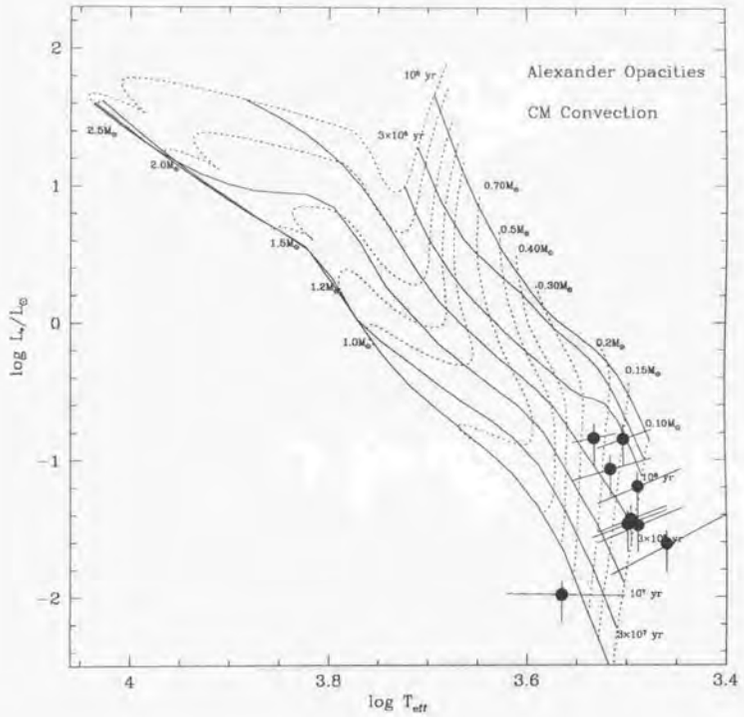

Fig. 14.— HR diagram of low-luminosity YSOs with evolutional tracks overlaid.

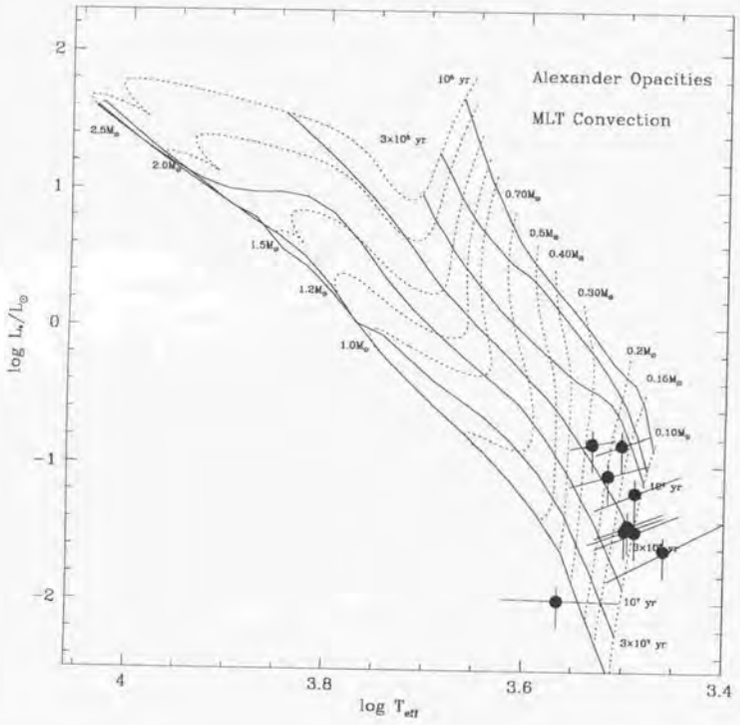

Fig. 14 (cont.).— HR diagram of low-luminosity YSOs with evolutional tracks overlaid.

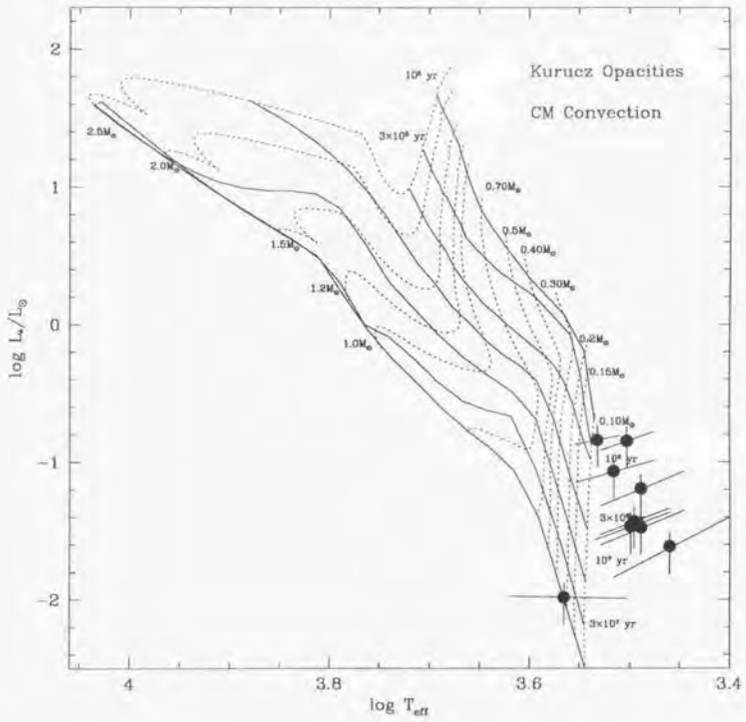

Fig. 14 (cont.).— HR diagram of low-luminosity YSOs with evolutional tracks overlaid.

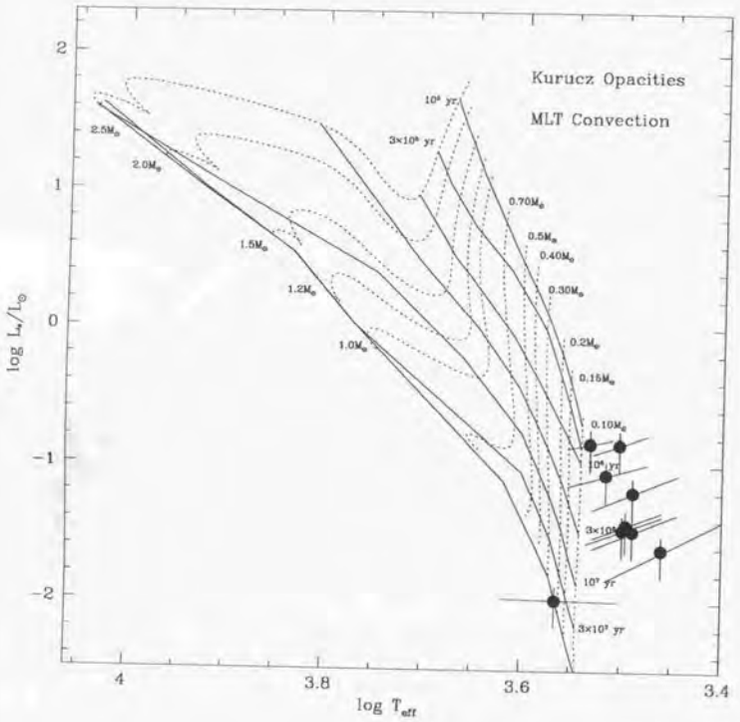

Fig. 14 (cont.).— HR diagram of low-luminosity YSOs with evolutional tracks overlaid.

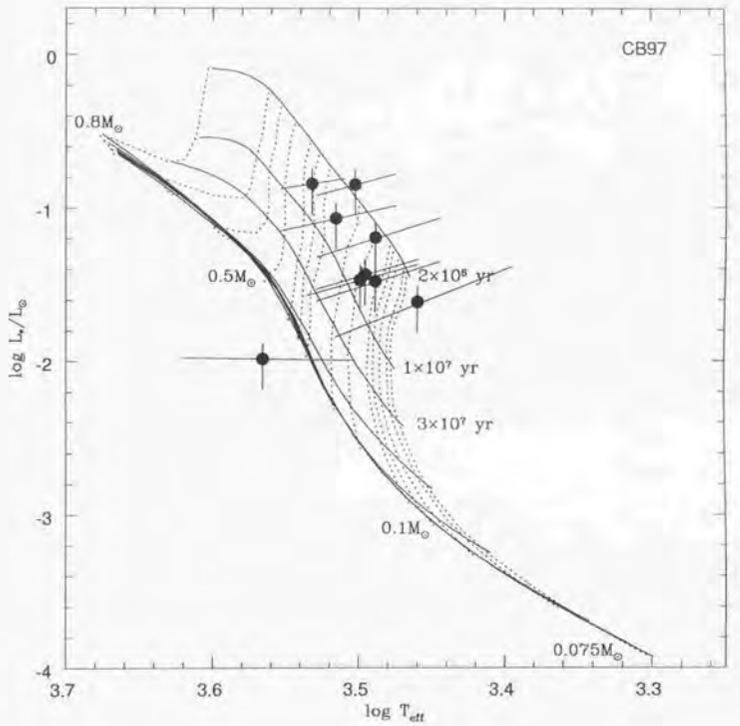

Fig. 14 (cont.).— HR diagram of low-luminosity YSOs with evolutional tracks overlaid.

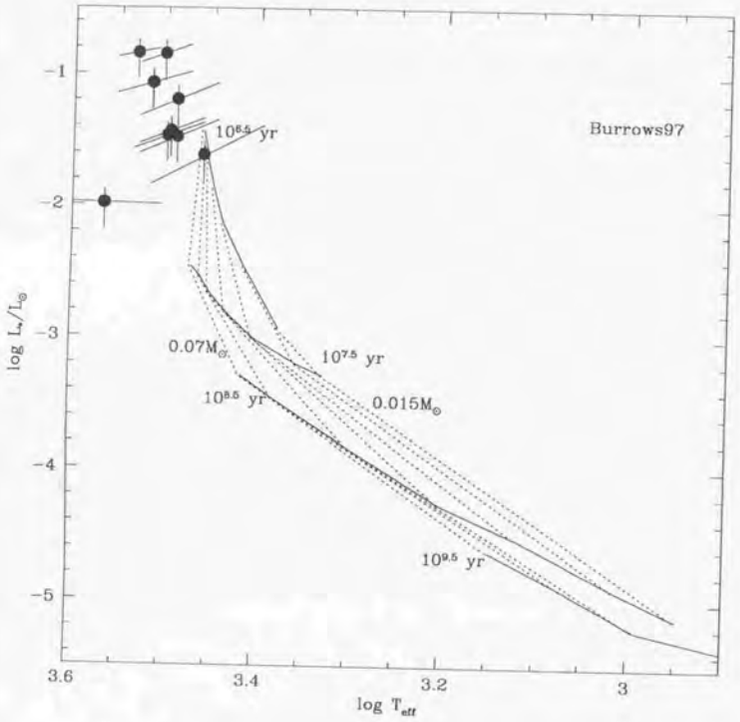

Fig. 14 (cont.).— HR diagram of low-luminosity YSOs with evolutional tracks overlaid.

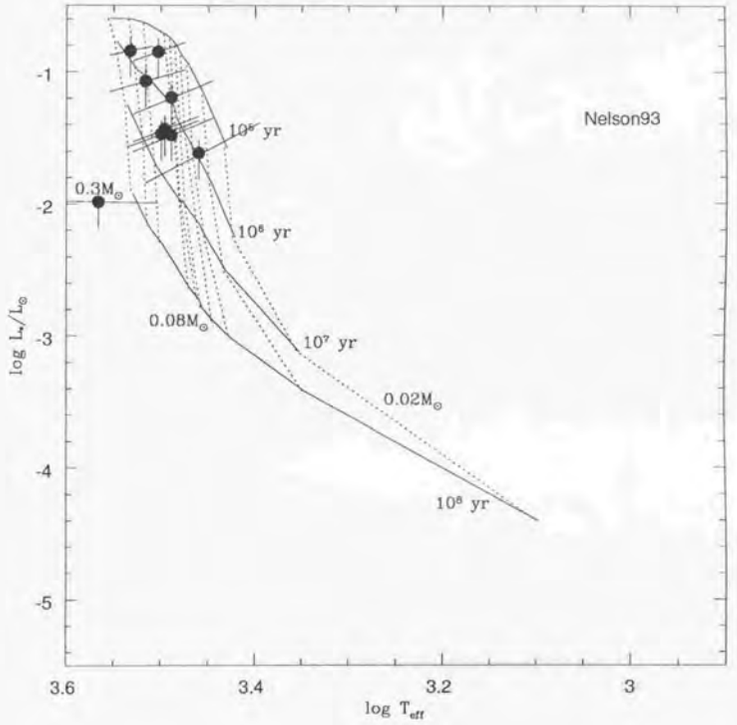

Fig. 14 (cont.).— HR diagram of low-luminosity YSOs with evolutional tracks overlaid.

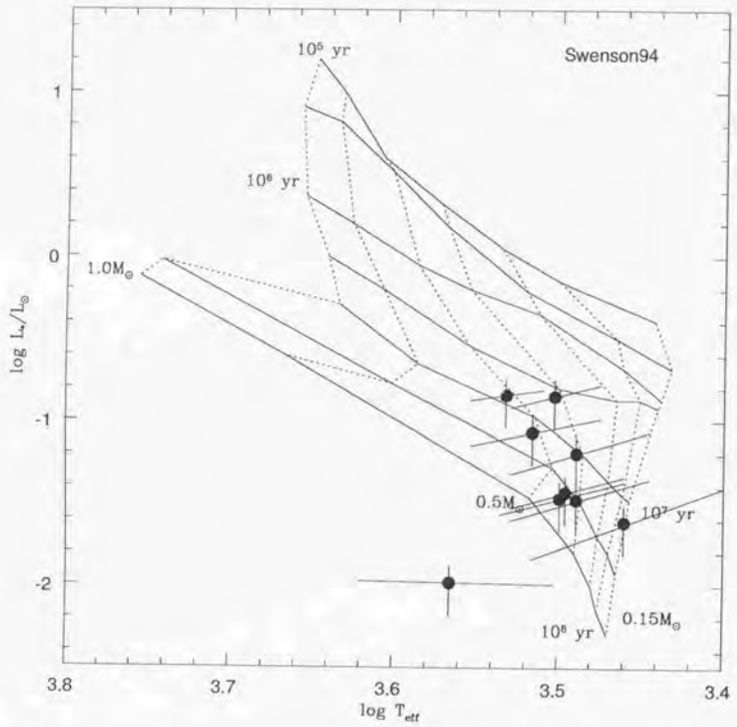

Fig. 14 (cont.).— HR diagram of low-luminosity YSOs with evolutional tracks overlaid.

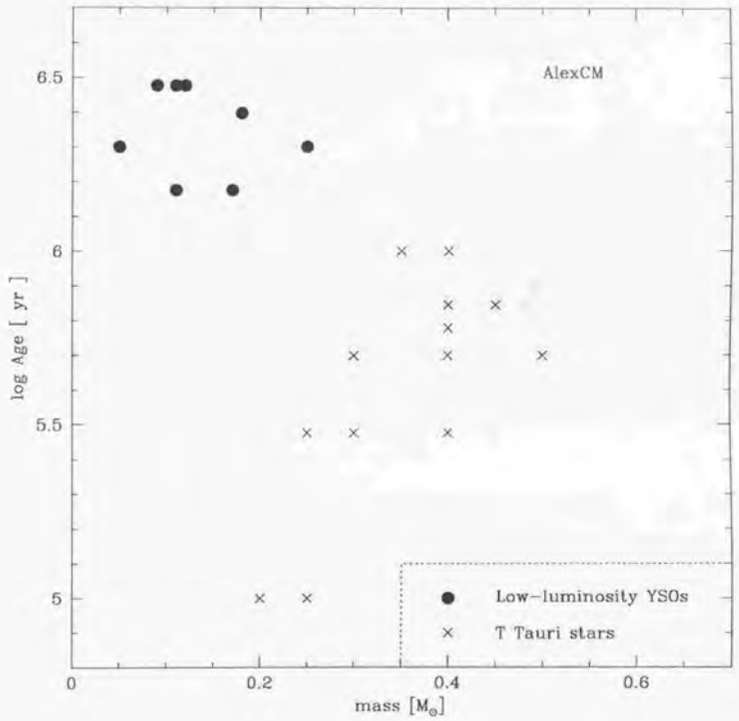

Fig. 15.— Mass vs. age for T Tauri stars and low-luminosity YSOs.

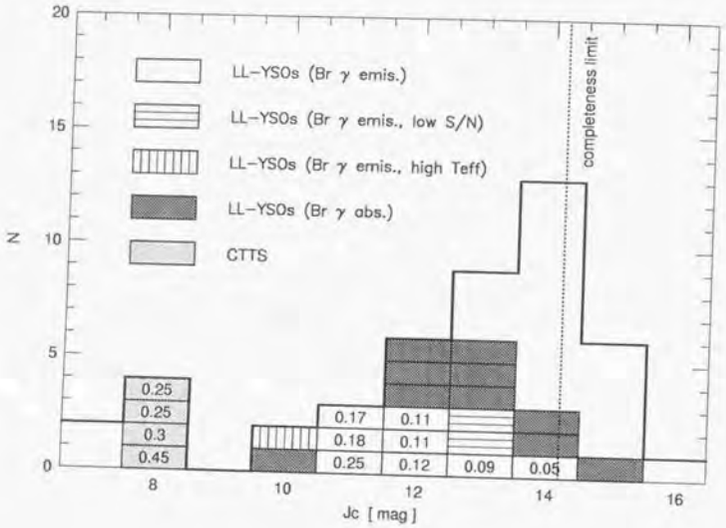

Fig. 16.— J luminosity function of the class II object candidates in Heiles Cloud 2 with mass estimated from spectroscopy. Mass is denoted in solar mass.

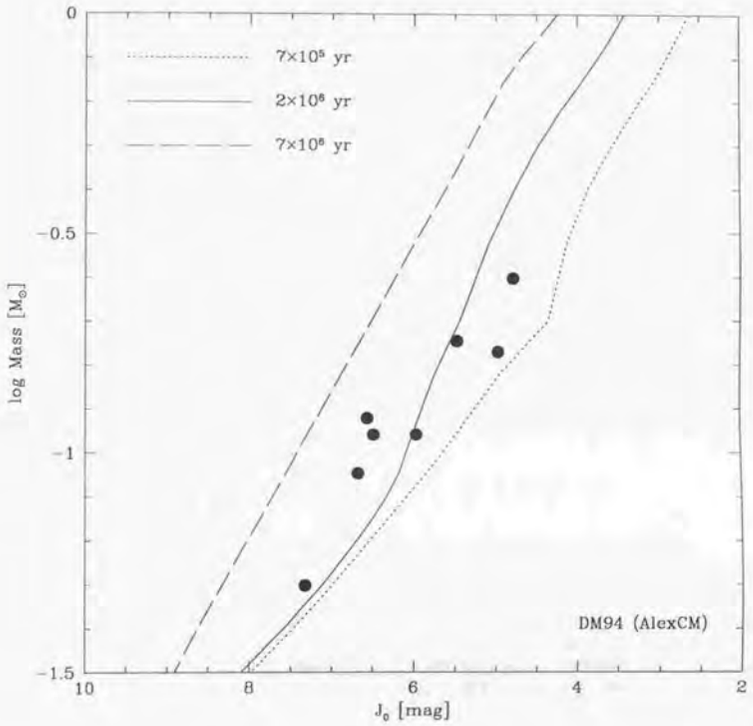

Fig. 17.— Comparison of mass and J band magnitude between the theoretical estimation and the spectroscopic estimation.

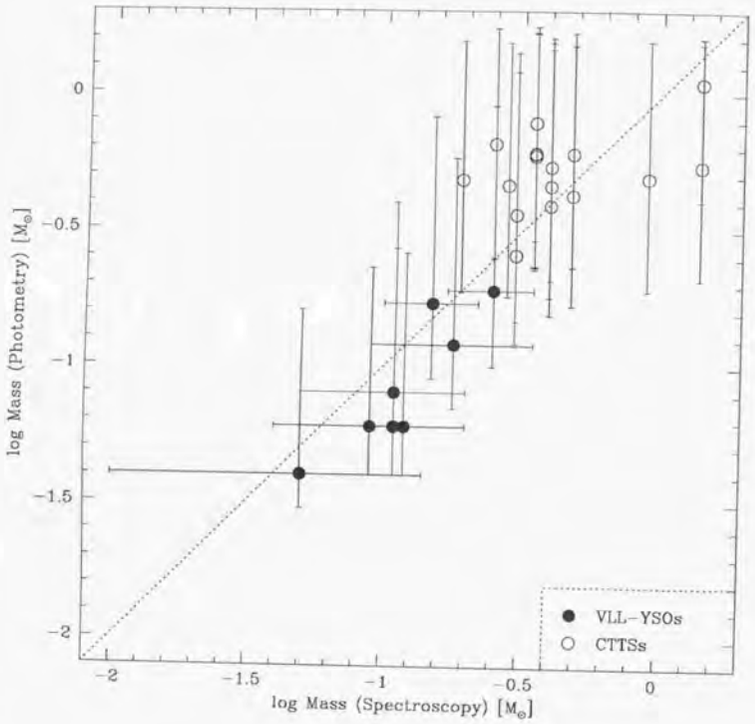

Fig. 18.— Relationship between mass deduced from spectroscopy and that deduced from photometry.

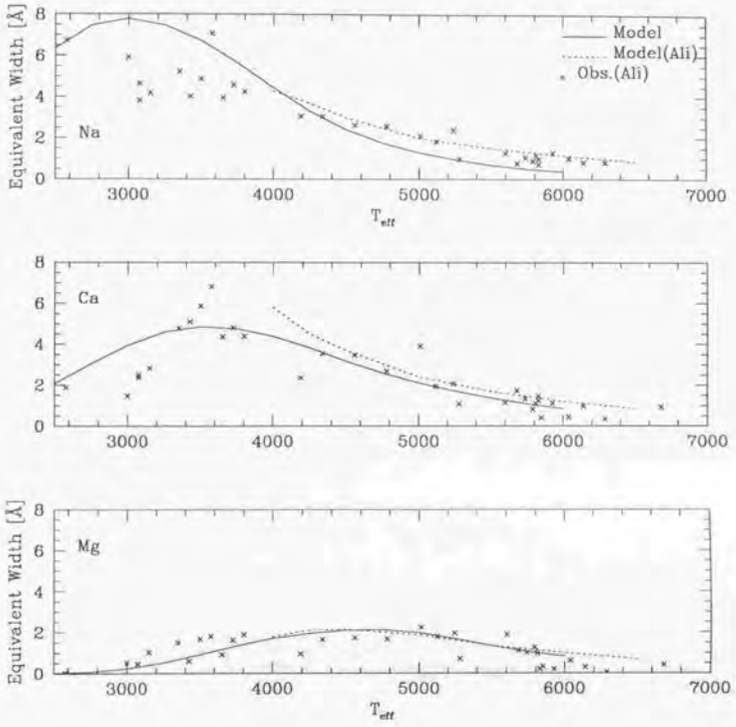

Fig. 19.— The equivalent widths of remarkable metallic lines derived by simple quantitative analysis (solid line) and by Ali et al.(1996)(dot line) are overplotted on the measurement equivalent width for nearby dwarfs.

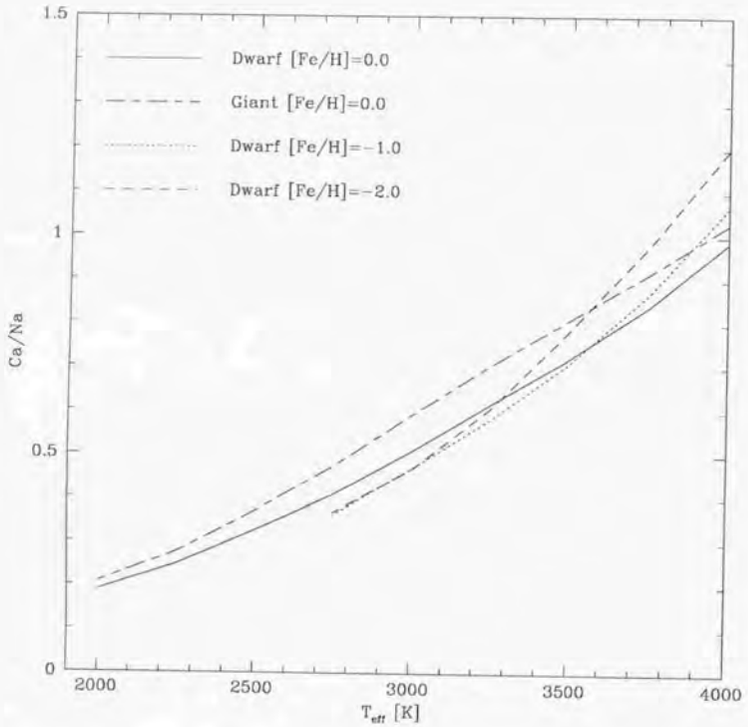

Fig. 20.— The Ca/Na line ratios. For dwarfs with [Fe/H]=0, the ratio is shown by a solid line, for dwarfs with [Fe/H]=-1.0 by a dot, [Fe/H]=-2.0 by a dashed line, and giants with solar abandance by a dot-dashed line. The line ratios are similar to each other except the extreme metal poor case.

Part III

Near-Infrared Search for Companions around Low-Luminosity YSOs in Taurus

Chapter 1

Previous Studies on Multiple Systems

1.1. Previous Observational Studies of Multiple Systems

1.1.1. Main Sequence Binary Systems

For main-sequence stars, the most comprehensive study about its multiplicity was made by Duquennoy & Mayor (1991). They carried out the radial velocity measurements of 164 main sequences in the solar neighborhood listed in Gliese & Jahreiss (1979). They concluded that the period distribution of the binary systems is unimodal and can be approximated by a Gaussian-type relation with a median period of 180 year. They also claimed that the secondary-mass distribution increases toward small secondary mass. This distribution is found similar to the mass-function found by Kroupa, Tout, & Gilmore (1990) for low-mass field stars.

Measurements of astrometric proper motion on photographic plates have been carried for the study of binary star. However, yet no convincing detections of substellar objects have resulted (e.g. Heintz 1990).

Speckle interferometry is another technique to search for brown dwarfs and stellar companions. Henry & McCarthy (1990) conducted infrared speckle observations of 27 nearby M dwarfs. They found 10 M dwarf multiple systems, and concluded that the infrared luminosity function at the low-luminosity end of the main sequence is not falling but rising for M_K <10 mag.

The techniques described above are sensitive to relatively close binaries. For wide-separated binaries, the simplest method – direct imaging – is useful. Simon, Henry & Kirkpatrick (1996) showed the results of direct imaging observations around 66 nearby M dwarfs. They identified no new stellar or substellar companions.

A brown dwarf, Gl229B, has been discovered by coronagraphic observation (Nakajima et al. 1995). Its low temperature, low luminosity ($<10^{-4}L_{\odot}$), and methane absorption spectrum make the object the definitive cold brown dwarf (Oppenheimer et al. 1995). Another recent exciting result is the detection of the planet around 51 Pegasi (Mayor & Queloz 1995). To date, more than a dozen extra-solar planets are found.

1.1.2. YSO Binary Systems

Spectroscopic Observations

For young stellar objects (YSOs), many studies have also been carried out. Mathieu, Walter & Myers (1989) discovered 6 YSO spectroscopic binaries among 53 naked T Tauri stars in the Taurus-Auriga, Ophiucus-Scopius, and Corona Australis star-forming regions. They concluded that the short-period (P <100 days) binary frequency of the naked T Tauri stars is indistinguishable from that found among nearby solar-mass stars.

Speckle Observations

A speckle observation is another technique for binary search. Ghez et al.(1993) made K band speckle observation of 69 T Tauri stars in the Taurus-Auriga and Ophiucus-Scopious star forming regions. The sample is flux-limited (K <8.5mag). They found 33 companions with separations from 0.″07 to 2.″5. They concluded that the binary star frequency for T Tauri stars is factor of 4 greater than that for the solar-type main sequence stars in the projected linear separation ranging from 16 to 252 AU. Ghez et al.(1995) monitored 20 T Tauri binary systems among the sample above by speckle imaging, in order to ascertain whether those systems are gravitationally bound system, and to derive dynamical mass of the systems.

Leinert et al.(1993) also studied the multiple frequency of YSOs. They surveyed bright (K <9.5) 104 T Tauri stars in the Taurus molecular cloud mainly by speckle observations. The degree of multiplicity in the T Tauri stars is 44/104 = 42%, which is higher than that found for main-sequence stars by factor 1.9±0.3.

Lunar Occultation

Another technique for multiple search is a lunar occultation observation. Simon et al.(1995) carried out an IR lunar occultation search for companions in the Ophiucus and the Taurus star forming regions. The sample is restricted to K <10 mag. The observed binary frequency in Ophiucus, in a 3-1400AU range of separations, is comparable to or greater than that of the nearby solar-like stars. They found no convincing difference in the binary frequency or distribution of separations of the systems with and without circumstellar disks.

These observational techniques described above suffer from selection effects. A radial

velocity observation requires a bright primary star because of its high wavelength resolution. A speckle observation and a lunar occultation observation are powerful tools for resolving out close binary systems consisting of two objects with similar luminosity. However, these techniques also need a bright primary star, because of the high speed exposures. Moreover, lunar occultation and speckle observations are not suitable for detecting a faint companion in the vicinity of the central bright star. In contrast, a direct imaging observation has a larger dynamic range (Itoh et al. 1998).

Direct Imaging Observations

Forrest, Ninkov & Garnett (1989) found faint objects around 13 T Tauri stars. They mentioned that 9 objects are probably Taurus members based on their red color. They estimated the mass to be in the range 0.005 – 0.015$M_\odot$. However, most of them have the similar near-infrared color to that of reddened field stars. Moreover, the separations are too large (typically more than 10″) to neglect confusion of background field stars. Therefore, they are mostly the background field stars. In fact, Stauffer et al.(1991) mentioned that with lack of spectral features of YSOs, the brown dwarf candidates identified by Forrest et al. (1989) are most likely to be heavily reddened background G or K field stars.

Moneti & Zinnecker (1991) observed 9 T Tauri binary systems (K <9.0) in the Taurus molecular cloud. They found that the brighter component is redder in $(J-K)$ in the most systems.

Brandner et al.(1996) presented the results of a direct imaging near-infrared survey for companions among X-ray selected YSOs. They observed 195 T Tauri stars (most of them are WTTSs) in the Chamaeleon, Lupus, and Scorpius star forming regions. They identified companions in 31 TTSs.

Recent progresses of adaptive optics technique enable us to resolve the binaries with

small separations. Bouvier, Rigaut, & Nadeau (1997) observed 144 G and K dwarf members of the Pleiades to search for close multiple systems using the CFHT's adaptive optics system. They detected 22 binaries and 3 triples with a separation between 11 and 910 AU. They derived that the binary frequency in the orbital period ranging from 10^4 to 10^7 days, is 28%, similar to that of field G dwarf binaries. They argued that the binary frequency difference between the Taurus and the Pleiades does not result from the evolution of the binary system during the pre-main sequence, but from the stellar density of the cluster.

Reid & Gizis (1997) observed 53 low-mass stars of the Hyades to search for brown dwarf companions using *HST*. They detected 9 binaries. The binary frequency for the systems with separations in the range 14 to 825 AU is 11.3%, similar to that of field M dwarf binaries. They found no brown dwarf companion and concluded that the mass ratio of low-mass binaries has a bias toward equal.

1.2. Theoretical Studies of Multiple System Formation

Three formation processes have been proposed for relatively wide-separated binary star formation: dynamical capture mechanism, collapse and fragmentation of dense molecular cloud core, and fragmentation of circumstellar disk.

McDonald & Clarke (1993) investigated the binary formation by dynamical capture within a small cluster. Their calculations suggested that the binary frequency increases with increasing primary mass. They also proposed dynamical capture mechanism with a circumstellar disk around a primary star, and led the similar binary frequency dependence on the primary star mass.

Burkert & Bodenheimer (1996) calculated the collapse of a rotating 1$M_\odot$ protostellar cloud and found that a multiple system was formed. Bonnell et al.(1994) calculated the fragmentation of uniform, isothermal elongated molecular cloud with rotation. They found

that when only a binary formed, the mass ratio is always close to unity.

Another approach for binary formation mechanism is the fragmentation of a protostellar disk. Bonnell (1994) supposed a gravitationally unstable disk around a central core. The fragmentation occurs and forms a binary system. While the emergent mass ratio is 3:2 or 3:1, they mentioned that the final mass ratio will depend strongly on the subsequent accretion. Boss (1997) examined gravitational instability in the outer solar nebula leading to giant planet formation. A $0.014M_{\odot}$ mass disk around one solar mass central star evolved to two-arm spiral shape, which changes to two giant planets. The emergent planets have a few Jupiter mass (about $0.005M_{\odot}$) and located at $\sim$8AU from the central star.

Motivated with the scientific interest described in Part I, we have conducted high-resolution direct near-infrared imaging of the low-luminosity YSOs detected by Itoh et al.(1996). In these observations, we have hoped to detect possible very low-luminosity companions. Since the primary source is already considered to be near the substellar domain, such companions may be the much more convincing case for brown dwarfs newly formed in the molecular cloud. The results also give the key to understand formation mechanism of such low-mass companions.

Chapter 2

Observations and Reduction

2.1. UH 2.2 m Telescope Observations

The data were obtained on the nights of 1997 October 11 and 12 on the University of Hawaii 2.2 meter telescope, at the summit of Mauna Kea, Hawaii. More than 300 images at J,H, and Ks bands were obtained using the infrared camera (QUIRC) on the F/31 Cassagrain focus with a spatial resolution of 0.″0612 per pixel. QUIRC is the infrared camera with a 1024×1024 pixels HgCdTe array, yielding a field of view of 62.″5. The tip-tilt secondary was also used when a visible guide star is located near the object.

17 YSO candidates listed in Itoh (1995) were observed. These YSO candidates have been found by the near-infrared survey of Heiles Cloud 2 of the Taurus molecular cloud using the Kitt Peak 1.3 meter telescope and the SQIID multi color camera. Their K band magnitudes are 9 to 13 mag, which are one or two orders of magnitude fainter than that of typical T Tauri stars. Considering that they have near-infrared excesses which imply a circumstellar disk, they are probably low mass YSOs analogous to CTTSs. The mass of some objects among the sample is deduced to be $0.1M_{\odot}$ $\sim$$0.2M_{\odot}$ from the near-infrared spectroscopic observation (see Part II). The limiting magnitude of this previous survey is 13

magnitude at K band, and the aperture radius of the photometry was about 3 arcsecond.

Every target was first observed in the Ks band, and if it appeared to be multiple, it was further observed in the H and J bands. The total exposure time in each filter was 10 minutes and consists of four 150 second exposures or eight 75 second exposures Each exposure is dithered about 3″ or 5″ each other. This technique avoids misidentification of ghost of the primary object as companion. For multiple systems, we also obtained a pair of short time exposure, typically 20 second exposures, for accurate photometry of primary object. Typical FWHM of the PSF is 0.″4 with the tip-tilt system, and 0.″8 without the tip-tilt. The observational log is summarized in Table 1.

For J and H bands, the flat field frames were made from sky images. For Ks band, thermal emission from dust on the camera window can affect the skyflat. We therefore used dome flat for Ks band. The large scale non-uniformity in the dome flat was removed by applying a 4th order surface fitting to the sky flat frame divided the dome flat frame. In Ks band, small scale non-uniformity was still remained. The non-uniformity of the flat field for Ks band is estimated to be within 2 %.

Each pair of the dithered images is subtracted with each other and flat fielded. Bad pixels are corrected by interpolation of neighbor pixels, if necessary. No deconvolution process was applied to the images before photometry.

The APPHOT package was used to derive relative photometry between the primary star and the other objects. The aperture radius is 0.″6 (with tip-tilt), or 1.″2 (without tip-tilt). For the multiple system whose separation is less than 3 arcsecond (the aperture radius of the SQIID survey), the magnitude of the primary and that of the secondary are combined, and compared with the magnitude derived from the SQIID observation. We estimate the completeness limit is around 17 magnitude at Ks band (discussed later).

The pixel scale is determined by snap shots of M15 cluster taken before the Taurus

run at the first night, with an optical astrometric table provided by Le Campion, Colin, & Geffert (1996).

2.2. Palomar 5 m telescope Observations

The other set of data were obtained on the nights of 1996 November 30 and December 1 on the Palomar 5 m telescope, California. More than 400 images at J, H, and Ks band were obtained using the D-78 InSb camera on the Cassagrain focus with a spatial resolution of 0.″125 per pixel. The camera was equipped with 256×256 InSb array, and the field of view is 32″ × 32″.

11 YSO candidates listed in Itoh (1995) and 3 reference fields were observed. Every target was observed in these 3 bands. The exposure of each target consists of one 20 sec exposure and four 150 sec exposures at J and H band. At Ks band, one 10 sec exposure and eight 75 sec exposures were taken. Each exposure is dithered about 3″ or 5″ each other. Due to a variable sky condition, the FWHM of the PSF changed between 0.″5 and 2″ during the night.

The stars listed in Elias et al.(1982) and SAO76542 were used as a standard star (Kenyon et al. 1993). Because these stars are very bright, each exposure was taken with the secondary mirror wobbled. The observation log is shown in Table 2.

Unfortunately, the field of view appeared to be partly blocked by the cooled Lyot stop inside the camera. The obscured portion increased with time. Even if the flat field frames were made by each filter and each object, time variations due to the Lyot stop motion could not be neglected, especially for the data taken at the second night. Moreover, relatively small number of the frame used for flat fielding makes about 5% non-uniformity remain in the resultant flat frame. These flat field problems as well as variable sky condition

limited photometric accuracies. Therefore only the multiplicity can be discussed from this observation.

Chapter 3

Results

The final Ks band images are shown in Figures $1 \sim 5$. We have detected 6 very low-luminosity YSO companion candidates among 23 low-luminosity YSOs in the Taurus molecular cloud. The results are listed in Table 3.

Figure 6 shows the $(J-H, H-Ks)$ color-color diagram for the detected companions and primaries. The intrinsic colors for main-sequence stars, giants (Bessell & Brett 1988), and supergiants (Tokunaga 1998) are plotted, together with the observed intrinsic colors of CTTSs (Strom et al. 1989). Reddening vectors (Koornneef 1983) are also shown. In this diagram a portion of CTTSs locates in the region redward of the region where the colors of field stars are plotted. This infrared excess is contributed by radiation from circumstellar disks. If it is assumed that the evolutional stage of the companion is almost the same as that of the primary objects and the companion also has a circumstellar disk, the companion YSOs can be distinguished from background stars by its infrared excess on this color-color diagram. In the figure, the colors of the primary objects are plotted by small filled circles, while those of the objects identified as the companion YSOs by this figure and its separation are plotted by large filled circles. The open squares are the color of the objects identified as background objects by this figure and the their separations to the primaries. The error

bars indicate 1 sigma photometric error in each color.

Figure 7 shows the $(J-H, J)$ color-magnitude diagram of the companion YSOs. The $J-H$ colors of the companions are shown by large filled circles, while the locations of the low-luminosity YSOs identified in the SQIID survey are plotted by small filled circles, the CTTSs corrected their visual extinction by dots, and the WTTSs corrected their visual extinction by open triangles. In the figure, the isochrones of low-mass stars and brown dwarfs calculated by D'Antona & Mazzitelli (1994) with the bolometric correction of Bessell (1991) are also plotted. The reddening vector is also shown, which are started from the intrinsic position of $0.08M_{\odot}$ at 10^7 year. The colors of the companion YSOs are similar to that of the YSOs detected previously, but their intrinsic J band magnitudes are about 4 magnitude fainter than those of the low-luminosity YSOs and 8 magnitude fainter than those of typical T Tauri stars.

Figure 8 shows the $(J-Ks, J)$ color-magnitude diagram of the companion YSOs. The notations are the same as in Figure 7. Moneti & Zinnecker(1991) observed 9 multiple system of T tauri stars. From the JK color-magnitude diagram they concluded that the primaries have a larger amount of near infrared excess emission than secondaries and this result indicates that as the stellar luminosity increases, the disk luminosity must increase more rapidly. However, Figure 8 does not show such a trend. This figure indicates that there is no correlation between Ks band magnitude of the object and infrared excess. Therefore it appears that the mass ratio of disk mass to central object mass is not correlated to central object mass.

Chapter 4

Discussion

4.1. Detection Limit for Distant Companions

For $r > 3''$ from the primary object, the effect of the halo component of the primary object is negligible. For the observation using the UH telescope with the tip-tilt system, the computer simulation including atmospheric turbulence shows that the intensity of the halo of the primary object is 5 order of magnitude fainter than the peak intensity of the PSF at 3 arcsec from the peak.

Therefore, the detection limit for a point source is determined by the sky noise in this region. When the detection limit is determined as the magnitude of the object with 1 sigma photometric accuracy, the limiting magnitude is estimated by

$$\text{standard deviation of the sky} \times \sqrt{\text{aperture area}} \qquad (4.1)$$

where aperture radius is the same for the primary object. The derived Ks band magnitudes of detection limit are listed in Table 4. For the observations with the tip-tilt system, the limiting magnitudes are around 21 mag at Ks band, while the limiting magnitudes are about 20 mag for the observations without the tip-tilt system.

4.2. Detection Limit for Close Companions

In order to estimate the limiting magnitude for detection of a point source in close vicinity of the primary object, we have added artificial PSFs to the original Ks band combined image. The FWHM of the artificial PSF is fixed to be the same as that of the primary object. The separations between the primary objects and the artificial PSFs are set to be 0.″61, 1.″22, 1.″84, and 2.″45. The magnitudes of the artificial PSFs are fixed to 3, 5, 7, and 9 magnitudes fainter than the magnitude of the primary. The position angles of the artificial PSF against to the primary are usually orthogonal. Because, in the cases of the images with brighter primary objects, diffraction pattern caused by spider appears in line and column direction, the position angles are rotated by 45°.

Detection of artificial PSFs added to the original images are made by eye. The results are tabulated in Table 5, where a clear detection is shown by an filled column, detection with ambiguous shape by a triangle, and no detection by a cross. For many images, the artificial point source whose magnitude is 9 magnitude fainter than that of the primary cannot be detected at any separation. This is due to sky noise (see the previous section), and is not the effect of the halo of the central object. On the other hand, the halo of the primary objects affects to detection of the objects in very close vicinity of the primary. It is the case that the artificial PSFs located at 0.″61 away from the primary are hardly detected even only 3 magnitude difference.

4.3. Resolved Objects by Deconvolution

One of the improvement techniques of image quality is the deconvolution method. The Lucy algorithm is employed to all Ks band images where artificial PSF are added in the same way as described in the previous section.

The PSFs of the image obtained by the observation have varied during the observation.

An image of the object identified as a background object is chosen as the PSF for each combined Ks band image. Because no field star is detected in the combined image of ITG35, deconvolution is not employed. Detections of artificial PSF are made by eye, and the results are tabulated in Table 6, as the same description in Table 5. Even with this deconvolution technique, the faint point source whose magnitude is 9 magnitude fainter than that of primary cannot be detected in any separation, and the closest point sources are almost failed to detect.

Therefore, these observations have incompleteness for the detection of the object whose Ks band magnitude is 7 magnitude fainter than that of the primary, or the object located within 1.2 arcsecond from the primary.

No reliable point source nor structure is newly found by deconvolution. In ITG 2, ITG12, ITG21, and ITG25, the features appear at very close of the primary. These are probably false images bacause the primaries are strongly saturated.

4.4. Confusion by Background Field Stars and Galaxies

Even though the field of view is relatively small, the imaging survey might be subject from background star confusion. While for the shallow imaging survey it is enough to consider only the effect of background star confusion, for deep survey, such as this study, galaxy should be taken into account as background confusion sources.

To estimate the number of background star, the model of the star distribution in the Galaxy by Jones et al.(1981) is considered. Though this model is simple, the result well accounts for the observed number of the background star toward several nearby dark cloud complexes (Jones et al.). The result is also valid for the star count of background field stars obtained by the small (such as $5' \times 5'$) and deep (K_{lim} ~16 mag) near-infrared survey (Oasa et al. 1998). The expected number of the background field star toward Heiles Cloud

2 is shown in Fig.11 by a dash line. The number increases with decreasing luminosity, but the number has a peak around K ~17. This is due to the finite thickness of the scale height of field stars in the Galaxy. Up to K ~18, background field stars are majority of the background source toward the observed region.

As a galaxy number counts model, the observational compilation data set listed by Gardner, Cowie, & Wainscoat (1993) is used. While they fit the compiled data by two linear lines, the second power polynomial fit is taken here. Theoretical galaxy number counts models are not used, because the estimated counts change by cosmological parameters, such as Q_0, Ω, and Λ, especially in the region fainter than 16mag at K band. The fitted line is shown in Fig.11 by a dot line. Beyond K ~19 mag, galaxies are the main component of the background source toward Heiles Cloud 2. The effect of the morphological recognition of galaxies is not considered.

The expected total number counts of the background source is shown in Fig.11 by a solid line. The number increases with down magnitude.

The limiting magnitudes for the wide fields determined in the previous section are in term of apparent magnitude. Toward a molecular cloud, however, background sources are subjected by the extinction of the cloud. The distribution model of field stars described above contains only diffuse interstellar extinction. Therefore the total visual extinction through the cloud toward observed region should be estimated. From near-infrared observation of 3 μm strong H_2O ice feature, Murakawa (1998) point out that Heiles Cloud 2 has a sub-structure whose size less than 2400AU (17″) in the line of the sight. Although the observation with a higher spatial resolution is need for accurate estimation of the extinction toward observed area, the $C^{18}O$ intensity map of Heiles Cloud 2 taken by Sunada et al.(1998) is used for estimation of extinction. This radio map is the highest resolution survey map of this cloud so far. The relationship between $C^{18}O$ column density and H_2 by Frerking et al.(1982), the relationship between H_2 and A_V by Dickman (1978), and 15 K as the excitation temperature of Heiles Cloud 2 (Fukui et al. 1991) are used for calculation of

the extinction. The derived visual extinction toward each observed region is between 0 mag and 7 mag at V band.

For the UH observation, the 1 σ detection limits corrected for the extinction of the cloud are about 21 mag for the observation with the tip-tilt system, and are about 20 mag at Ks band for the observation without the tip-tilt system. The expected total number counts of the background sources in the observed field of each object (60″ × 60″) and the region near the primary object (10″ × 10″ or 5″ × 5″) are shown in Table 7. Four or eight background objects are expected to be found in each frame with 1 σ error, and two objects with 10 σ. These values are consistent with the observational Ks band images.

4.5. Estimation of Mass of the Companion YSOs

Recent progresses on the theory of evolutional tracks and atmosphere for very low-mass stars, brown dwarfs, and giant planets enable us to estimate the mass of very low luminosity YSOs with some assumptions.

The assumptions are follows.

- The low luminosity companions are analogous to Class II objects which have active boundary region and optical thick accretion disks. Because the J band emission arises primarily from the photosphere for Class II objects (Bertout, Basri, & Bouvier 1988), the J band luminosity which is corrected for interstellar extinction and distance modulus is of photospheric origin for the low-luminosity companions. The extinction to each object is determined in the previous section and the distance to the Taurus molecular cloud is assumed to be 140pc (Elias 1978; Preibisch & Smith 1997).
- Based on the evolutional track of D'Antona & Mazzitelli (1994), it is estimated that the age of visible Class II objects in the Taurus-Auriga Complex listed in Strom et al. (1989) is distributed between $10^{4.5}$yr and $10^{7.5}$yr with an average of 10^6 yr. Because the

primaries and companions have infrared excesses which indicate circumstellar disk, the age of these objects might also be within this range. The near-infrared spectroscopy of the low-luminosity YSOs in Heiles Cloud 2 confirms that their age is about 10^6 yr. Therefore, 10^6 year and 10^7 year are assumed as the age of the companions.

The evolutional model of D'Antona & Mazzitelli (1994) is taken for low mass and very low mass stars, and the model by Burrows et al.(1997) for brown dwarfs and giant planets. For the object whose effective temperature is hotter than 2200K, empirical bolometric corrections are derived by Bessell (1991). This bolometric correction is combined with the model of D'Antona & Mazzitell to translate bolometric luminosity and effective temperature scale to J band magnitude and mass scale. Otherwise the color derived from the synthetic spectra provided by Hauschldt & Allard (on WWW) is used with the evolutional track of brown dwarfs and giant planets by Burrows et al. As the synthetic spectra are not available for solar metallicity to date, the color table for [Fe/H]=-1.0 is used. The J band magnitude differences between [Fe/H]=-1.0 and [Fe/H]=-2.0 are within 0.1 magnitude for any mass, therefore, it has no significant effect on the results and discussions to use the color table for [Fe/H]=-1.0.

Figure 12 shows the relation between mass of an object and J band magnitude, for the age of 10^6 year and 10^7 year, and using the model of D'Antona & Mazzitelli and the model of Burrows et al.. The J band magnitude of low mass stars, brown dwarfs, and giant planet decreases with the mass increasing or the age decreasing. These two models have reasonable agreement each other. Disagreement is 0.5 mag at J band or 60% in mass at maximum.

Using this J–mass relation, the mass of each companion object is calculated. The derived mass is tabulated in Table 9. All companions are estimated to have masses less than $0.08 M_\odot$. Moreover, the derived masses of ITG 9c, ITG 33b, and ITG 45b appear to fall into the region of giant planets.

4.6. Mass Ratio of Primary and Companion

The mass ratios ($M_{secondary}/M_{primary}$) of the binary/multiple systems are estimated. The mass of the primary stars is derived from the model of D'Antona & Mazzitelli (1994), and the mass of the companions is deduced from the model of D'Antona & Mazzitelli(1994) and the model of Burrows et al.(1997). For ITG15 and ITG25 the mass estimated from near-infrared spectroscopy (see Part II) is used. Both cases of the age of 10^6 yr and 10^7 yr are estimated. The results are shown in Table 10. For many cases, only an upper limit of the mass of the companion is estimated, so that the derived mass ratio shows only its lower limit. For the most cases the mass ratio appears to be less than 0.4.

The mass ratio of the low-luminosity YSOs seems to differ from the mass ratio of T Tauri binary systems. Statistical tests are carried out between these two samples. We used TWOSAMPT task in STSDAS package. This task contains several kinds of two-sample censored tests, dealing with non-detection data as well as detected data. We took the results of Ghez et al.(1993) as the T Tauri binary sample, because they provided flux ratio limits at K band for the stars without companion stars. The flux ratio limits of the UH observation are calculated in Section 4.1 in terms of ΔK. The Kaplan-Meier mean of K band flux ratio of T Tauri sample and of low-luminosity YSOs sample are 24.9±2.9 and 1718±580, respectively. The probabilities of coincident population of these two samples are 0.01 or less from all tests except Peto & Prentice test where the probability is 0.33. The parent populations of T Tauri binary systems and low-luminosity YSO binary systems might be different.

The formation mechanisms may not be the same between the objects detected by Ghez et al. and the objects detected in the UH observation. Ghez et al. observed bright T Tauri stars as primaries and found companions with comparable fluxes to the primaries. Therefore these companions are probably low-mass stars. On the other hand, the primary objects observed by the UH observation are low-luminosity YSOs, whose masses are estimated to

be $0.05M_{\odot}$ ~$0.25M_{\odot}$ by our photometry or spectroscopy. The companions are much fainter than the primaries so that they are considered to have a mass of brown dwarf. Masses of some objects are less than $0.015M_{\odot}$, if the age of 10^6 year is assumed, almost corresponding to a large planet mass (Table 9). One possibility is that they would be born in circumstellar disks around the primaries, while the T Tauri companions in fragment of the parent cloud. Bonnell et al.(1991) claimed that not only planets but also brown dwarfs and low-mass stars can be form in circumstellar disks. The derived mass ratio from disk fragmentation is calculated to be 0.28, which is similar value to the mass ratio of the low-luminosity YSOs binary systems.

However, care should be taken on the statistical discussion because of the small sample for the low-luminosity YSO candidates. If one binary system with equal K band fluxes adds to the low-luminosity YSOs sample, the probabilities for the parent population of the two samples change to as high as 0.65 for Peto & Prentice test. A direct imaging observation or a coronagraphic observation of faint companion around bright T Tauri stars is required.

4.7. Binary Frequency

By combining the UH observations with the Palomar observations, we have observed 23 systems in total. The binary frequency of these objects in term of the intrinsic J band luminosity of the primary objects is shown in Table 11. There is no systematic trend of the binary frequency with the brightness of the primary objects. This result is consistent with the results of Ghez et al.(1993) and Leinert et al.(1993), who searched multiple system around T Tauri stars mainly by K band speckle observations.

To compare the binary frequency of the low luminosity YSOs to that of field dwarfs and that of T Tauri stars, we need to translate the projected separations into orbital periods. First, the measured projected separations (ρ) are converted to the semi-major axes (a).

Assumig random inclination of the orbital plane, the relation is described as

$$< \log a >=< \log \rho > + \log c \qquad (4.2)$$

where log c is a constant whose value has been estimated to be 0.1 (Duquennoy & Mayor 1991, Reipurth & Zinnecker 1993). The derived values of the semi-major axes are between 400 AU and 1500 AU. Next, the orbital periods are calculated from the Kepler's third law, with the mass of the primary object and of the companion. The age of the all objects is assumed to be 10^6 yr. The derived orbital periods are listed in Table 12.

The observations are complete for the companion whose separation to the primary is wider than $1''.5$ and $M_{sc} > 0.006M_{\odot}$. The binary frequency (number of binary systems / number of objects in the sample) is 5/23 or 22^{+9}_{-10}% for the system whose period is 10^7 ~10^8 day. The error is estimated based on Poisson statistics. This is shown in Figure 14, where the biary frequencies of nearby dwarfs(Duquennoy & Mayor 1993) and those of T Tauri stars (Leinert et al. 1993) are also shown. While the binary frequency deduced by this work is not inconsistent with the binary frequency of visible T Tauri stars, the frequency is significantly higher than that of nearby stars.

Chapter 5

Conclusions

Near-infrared imaging observations for companions around low-luminosity YSOs in the Taurus molecular cloud have been carried out. The observations have been benefited from the high spatial resolution due to the tip-tilt secondary as well as large-format infrared array, resulting in discovery of faint companions.

1. Six very low-luminosity YSO candidates are found as companions. Their magnitudes are $15 \sim 19$ magnitude at J band.

2. The mass of the all companions is estimated from J band luminosity, using recent evolutional tracks. The mass of the companions is estimated to be comparable to that of brown dwarfs, or even planet regime for some companions.

3. The magnitude differences between the very low-luminosity companion candidates and the primaries range from 2 and 5mag at Ks band, which are significantly larger than the difference of T Tauri binaries. Statistical tests indicate that this is not only due to different observation techniques but also due to differece in the parent populations of the samples. Large magnitude differences suggest that the mass ratio of the binary ($M_{secondary}/M_{primary}$) is small, therefore, these very low-luminosity YSO companions

might be born from fragmentation of a disk around the central object. Higher dynamic range observations of YSO binary systems, such as coronagraphic observations, will be important solve the question whether different binary formations occur or not.

4. The binary frequency is 22^{+9}_{-10}% for the system whose period is $10^7 \sim 10^8$day. This frequency is consistent with that of T Tauri stars, but significantly higher than that of nearby main sequence stars. Such a high binary frequency even for low-luminosity binary systems excludes the binary formation mechanism by capture.

Chapter 6

Appendix — Comment on Interesting Sources

ITG 12

This is known as IRAS04361+2547. This is an extended source. Tamura et al.(1991) also observed this object and found the reflection nebula, whose size is about 4000AU (30″).

ITG 13

The secondary is detected near the primary object by the Palomar observation. While photometry of the Palomar observation is not trustworthy, however, the near-infrared colors are consistent with reddened background star. The K band spectrum of the primary shows the deep Br γ in absorption. The metallic lines and H_2O band absorption og the primary indicate moderately high temperature. Therefore the primary object may also background star and the binary may be only by chance.

ITG 15

This is a binary system. The K band spectroscopy indicates that the temperature of this primary is 3000K∼3400K. The mass of the primary is estimated to be $0.1{\sim}0.45M_{\odot}$.

ITG 25

This is known as IRAS04370+2559. This is a binary system. The K band spectrum of the primary shows Brγ in emission (the strongest emission in the spectroscopy sample), as well as H_2O band absorption at $2.05{\sim}2.15\mu$m.

ITG 33

This is a binary system. The K band spectrum of this primary shows Br γ in emission, metallic absorption lines, and deep CO band head absorption. The metallic line ratio of Na to Ca, and slight H_2O band absorption indicate that the primary is not very cool. However, any evolutional track cannot account for the location of the primary on the HR diagram.

ITG 35

This object is known as IRAS04381+2540. This is an extended source. Tamura et al.(1991) presented small nebulosity at K band. They estimated that the size of the nebulosity is about 3000AU.

ITG 45

This is a binary system. The separation is very small, and the secondary is very faint at near-infrared wavelength.

Table 1. University of Hawaii 2.2 m Telescope Observation Log.

Object	Date	Integration Time (sec×times)			FWHM	Comment
		J	H	Ks	(arcsec)	
1	Oct.13	···	···	75×8, 20×2	0.3	
2	Oct.12	···	···	75×8, 20×2	0.3	
6	Oct.12	···	···	75×8, 20×2	0.5	
9	Oct.13	150×4	150×4	75×8, 20×2	0.6	no Tip-Tilt
12	Oct.13	150×4	150×4	75×8, 20×2	0.8	no Tip-Tilt
15	Oct.13	150×4	150×4	75×8, 20×2	0.8	no Tip-Tilt
17	Oct.13	···	···	75×8, 20×2	0.8	no Tip-Tilt
21	Oct.13	···	···	75×8, 20×2	1.0	no Tip-Tilt
25	Oct.12	150×4	75×8, 20×2	75×12, 20×2	0.6	
27	Oct.13	···	···	75×8, 20×2	0.5	
32	Oct.13	···	···	75×8, 20×2	0.3	
33	Oct.12	150×4	150×4, 20×2	75×8, 20×2	0.3	
35	Oct.12	150×4	150×4	75×8, 20×2	0.4?	
41	Oct.12	···	···	75×8, 20×2	0.4	
42	Oct.13	···	···	75×8, 20×2	0.4	
45	Oct.12	150×4	150×4	75×8, 20×2	0.3	
46	Oct.12	···	···	75×8, 20×2	0.4	

Table 2. Palomar 5 m Telescope Observation Log.

Object	Date	Integration Time (sec×times)			FWHM
		J	H	Ks	(arcsec)
9	Nov.30	150×4, 20×1	75×8, 20×1	75×8, 10×1	1.3
13	Nov.30	150×4, 20×1	75×8, 20×1	75×8, 10×1	1.3
16	Dec.1	150×4, 20×1	75×8, 20×1	75×8, 10×1	1.0
24	Nov.30	180×4, 60×1	60×10	60×10	1.3
25	Dec.1	75×8, 10×1	75×4, 5×1	75×8, 3×1	1.3
29	Nov.30	150×4, 20×1	75×8, 20×1	75×8, 10×1	2.5
32	Dec.1	150×4, 20×1	75×8, 20×1	75×8, 10×1	1.3
33	Nov.30	150×4, 20×1	75×8, 20×1	75×8, 10×1	1.3
37	Dec.1	150×4, 20×1	75×8, 20×1	75×8, 10×1	1.3
43	Nov.30	150×4, 20×1	75×8, 20×1	75×8, 10×1	1.9
45	Dec.1	150×8, 20×1	75×8, 20×1	75×8, 10×1	0.9

Table 3. Luminosities and separations of low-luminosity YSO companion candidates.

Object	Ks (mag)	$J-H$ (mag)	$H-Ks$ (mag)	separation ($''$)	$\Delta\alpha$ ($''$)	$\Delta\delta$ ($''$)
9b	14.45±0.03	0.70±0.04	0.70±0.04	4.339±0.006	0.445±0.001	4.316±0.006
9c	17.57±0.10	0.92±0.12	0.56±0.13	8.50	-3.84	7.59
15b	14.50±0.01	1.01±0.02	0.73±0.02	3.004±0.013	-1.792±0.016	2.408±0.003
17b†	16.77±0.06	···	···	4.19	3.72	-1.92
25b	13.38±0.01	2.14±0.01	1.28±0.01	4.320±0.011	-3.932±0.016	-1.788±0.008
33b	16.05±0.02	0.79±0.04	0.54±0.03	5.203±0.002	-2.239±0.000	4.696±0.002
45b	15.76±0.05	1.33±0.08	0.91±0.09	2.301±0.058	-2.294±0.066	-0.027±0.106

†No photometry is available at J & H band. Therefore we do not regard this object as a YSO companion candidate.

Table 4. Detection limit at Ks band.

Region	Ks_{lim} [mag]
with tip-tilt	
ITG2	21.3
ITG6	21.5
ITG25	21.5
ITG33	22.2
ITG35	21.3
ITG41	21.5
ITG45	20.1
ITG46	21.3
without tip-tilt	
ITG1	20.4
ITG9	20.6
ITG12	20.5
ITG15	20.4
ITG17	20.7
ITG21	20.6
ITG27	20.5
ITG32	20.6
ITG42	20.7

Table 5. Detection limits without deconvolution.

Object	Magnitude difference	Separation 0.″61	1.″22	1.″84	2.″45
1	3	△	▬	▬	▬
	5	×	▬	▬	▬
	7	×	×	×	×
	9	×	×	×	×
2	3	×	▬	▬	▬
	5	×	△	▬	▬
	7	×	×	▬	▬
	9	×	×	▬	▬
6	3	×	▬	▬	▬
	5	×	△	▬	▬
	7	×	×	▬	▬
	9	×	×	×	×
9	3	×	▬	▬	▬
	5	×	×	▬	▬
	7	×	×	×	×
	9	×	×	×	×
12	3	×	△	▬	▬
	5	×	×	▬	▬
	7	×	×	×	×
	9	×	×	×	×
15	3	×	▬	▬	▬
	5	×	×	▬	▬
	7	×	×	×	×
	9	×	×	×	×
17	3	×	▬	▬	▬
	5	×	×	▬	▬
	7	×	×	×	×
	9	×	×	×	×
21	3	×	△	▬	▬
	5	×	×	×	▬
	7	×	×	×	×
	9	×	×	×	×
25	3	×	▬	▬	▬
	5	×	▬	▬	▬
	7	×	×	▬	▬
	9	×	×	×	△
27	3	×	▬	▬	▬
	5	×	×	▬	▬
	7	×	×	×	▬
	9	×	×	×	×

Table 5—Continued

Object	Magnitude difference	Separation 0.″61	1.″22	1.″84	2.″45
32	3	△	▬	▬	▬
	5	×	▬	▬	▬
	7	×	×	×	×
	9	×	×	×	×
33	3	▬	▬	▬	▬
	5	×	▬	▬	▬
	7	×	△	▬	▬
	9	×	×	×	×
41	3	×	▬	▬	▬
	5	×	△	▬	▬
	7	×	×	×	×
	9	×	×	×	×
42	3	×	×	▬	▬
	5	×	×	▬	▬
	7	×	×	×	×
	9	×	×	×	×
45	3	▬	▬	▬	▬
	5	×	▬	▬	▬
	7	×	×	×	×
	9	×	×	×	×
46	3	×	▬	▬	▬
	5	×	▬	▬	▬
	7	×	×	▬	▬
	9	×	×	×	×

▬ : clear detection

△ : detection with ambiguous shape

× : no detection

Table 6. Detection limits with deconvolution.

Object	Magnitude difference	Separation 0.″61	1.″22	1.″84	2.″45
1	3	×	△	▬	▬
	5	×	×	×	×
	7	×	×	×	×
	9	×	×	×	×
2	3	▬	▬	▬	▬
	5	×	▬	▬	▬
	7	×	×	▬	▬
	9	×	×	▬	▬
6	3	△	▬	▬	▬
	5	×	▬	▬	▬
	7	×	×	×	×
	9	×	×	×	×
9	3	×	△	▬	▬
	5	×	×	×	×
	7	×	×	×	×
	9	×	×	×	×
12	3	×	▬	▬	▬
	5	×	×	×	×
	7	×	×	×	×
	9	×	×	×	×
15	3	×	△	▬	▬
	5	×	×	×	×
	7	×	×	×	×
	9	×	×	×	×
17	3	×	×	▬	▬
	5	×	×	×	×
	7	×	×	×	×
	9	×	×	×	×
21	3	×	×	×	×
	5	×	×	×	×
	7	×	×	×	×
	9	×	×	×	×
25	3	×	▬	▬	▬
	5	×	▬	▬	▬
	7	×	△	▬	▬
	9	×	×	×	×
27	3	×	▬	▬	▬
	5	×	×	×	×
	7	×	×	×	×
	9	×	×	×	×

Table 6—Continued

Object	Magnitude difference	Separation 0.″61	1.″22	1.″84	2.″45
32	3	×	▬	▬	▬
	5	×	▬	×	×
	7	×	×	×	×
	9	×	×	×	×
33	3	▬	▬	▬	▬
	5	×	▬	▬	▬
	7	×	×	×	×
	9	×	×	×	×
41	3	×	▬	▬	▬
	5	×	×	×	×
	7	×	×	×	×
	9	×	×	×	×
42	3	×	×	▬	▬
	5	×	×	×	×
	7	×	×	×	×
	9	×	×	×	×
45	3	▬	▬	▬	▬
	5	×	▬	▬	▬
	7	×	×	×	×
	9	×	×	×	×
46	3	×	▬	▬	▬
	5	×	×	×	×
	7	×	×	×	×
	9	×	×	×	×

Table 7. Expected number of background objects.

K magnitude	$1^\circ \times 1^\circ$	$1' \times 1'$	$10'' \times 10''$	$5'' \times 5''$
18	8333	2.31	0.064	0.016
20	16695	4.64	0.13	0.032
21	30444	8.46	0.23	0.059

Table 8. Minimum mass ratio limits(q_{min}) for each observation.

Object		Separation			
	difference	0.″61	1.″22	1.″84	2.″45
2	$\Delta\ Ks_{max}$	3	5	9	9
	J_{lim}	9	11	15	15
	M_{sc}	0.017	<0.006	<0.006	<0.006
	q_{min}	0.21	<0.08	<0.08	<0.08
6	$\Delta\ Ks_{max}$	3	5	7	7
	J_{lim}	10	12	14	14
	M_{sc}	0.01	<0.006	<0.006	<0.006
	q_{min}	0.017	<0.1	<0.1	<0.1
25	$\Delta\ Ks_{max}$	<3	7	7	9
	J_{lim}	<8	12	12	14
	M_{sc}	0.025	<0.006	<0.006	<0.006
	q_{min}	0.13	<0.03	<0.03	<0.03
33	$\Delta\ Ks_{max}$	3	7	7	7
	J_{lim}	11	15	15	15
	M_{sc}	<0.006	<0.006	<0.006	<0.006
	q_{min}	<0.2	<0.2	<0.2	<0.2
41	$\Delta\ Ks_{max}$	<3	5	7	7
	J_{lim}	<9	11	13	13
	M_{sc}	>0.017	<0.006	<0.006	<0.006
	q_{min}	>0.14	<0.05	<0.05	<0.05
45	$\Delta\ Ks_{max}$	3	5	5	5
	J_{lim}	12	14	14	14
	M_{sc}	<0.006	<0.006	<0.006	<0.006
	q_{min}	<0.3	<0.3	<0.3	<0.3
46	$\Delta\ Ks_{max}$	<3	5	7	7
	J_{lim}	<10	12	14	14
	M_{sc}	>0.01	<0.006	<0.006	<0.006
	q_{min}	>0.2	<0.12	<0.12	<0.12
1	$\Delta\ Ks_{max}$	3	5	5	5
	J_{lim}	12	14	14	14
	M_{sc}	<0.006	<0.006	<0.006	<0.006
	q_{min}	<0.3	<0.3	<0.3	<0.3

Table 8—Continued

Object	difference	Separation 0.″61	1.″22	1.″84	2.″45
9	$\Delta\ Ks_{max}$	<3	3	5	5
	J_{lim}	<12	12	14	14
	M_{sc}	>0.006	<0.006	<0.006	<0.006
	q_{min}	>0.2	<0.2	<0.2	<0.2
12	$\Delta\ Ks_{max}$	<3	3	5	5
	J_{lim}	<12	12	14	14
	M_{sc}	<0.006	<0.006	<0.006	<0.006
	q_{min}		Class I		
15	$\Delta\ Ks_{max}$	<3	3	5	5
	J_{lim}	<8	8	10	10
	M_{sc}	>0.025	0.025	0.011	0.011
	q_{min}	>0.15	0.15	0.06	0.06
17	$\Delta\ Ks_{max}$	<3	3	5	5
	J_{lim}	<10	10	12	12
	M_{sc}	>0.011	0.011	<0.006	<0.006
	q_{min}	>0.18	0.18	0.10	0.10
21	$\Delta\ Ks_{max}$	<3	3	3	5
	J_{lim}	<10	10	10	12
	M_{sc}	>0.011	0.011	0.011	<0.006
	q_{min}	>0.18	0.18	0.18	<0.1
27	$\Delta\ Ks_{max}$	<3	3	5	7
	J_{lim}	<7	7	9	11
	M_{sc}	>0.05	0.05	0.017	<0.006
	q_{min}	>0.18	0.18	0.06	<0.02
32	$\Delta\ Ks_{max}$	3	5	5	7
	J_{lim}	12	14	14	14
	M_{sc}	<0.006	<0.006	<0.006	<0.006
	q_{min}	<0.3	<0.3	<0.3	<0.3
42	$\Delta\ Ks_{max}$	<3	<3	5	5
	J_{lim}	<12	<12	14	14
	M_{sc}	<0.006	<0.006	<0.006	<0.006
	q_{min}	<0.2	<0.2	<0.2	<0.2

Table 9. Estimated mass of companion candidates.

Object	J_0 [mag.]	DM(1Myr) [$M_\odot$]	DM(10Myr) [$M_\odot$]	Burrows(1Myr) [$M_\odot$]	Burrows(10Myr) [$M_\odot$]
9b	10.13	<0.02	<0.02	0.010	0.018
9c	13.05	<0.02	<0.02	<0.006	<0.009
15b	10.21	<0.02	<0.02	0.009	0.016
25b	8.53	0.02	0.06	0.015∼0.020	0.055
33b	11.64	<0.02	<0.02	<0.006	0.011
45b	11.37	<0.02	<0.02	<0.006	0.012

Table 10. Mass ratio of the multiple systems.

Object	DM(1Myr)	DM(10Myr)	Burrows(1Myr)	Burrows(10Myr)
9b	<0.80	<0.40	0.40	0.36
9c	<0.80	<0.40	<0.24	<0.18
15b	<0.14	<0.14	0.06	0.11
25b	0.08	0.24	0.07	0.22
33b	<0.57	<0.22	<0.17	0.12
45b	<0.87	<0.50	<0.15	0.30

Table 11. Binary frequency as the function of the J band luminosity of the primary star (binary:total).

J_0	4 mag.	5 mag.	6 mag.	7 mag.	8 mag.	9 mag.
	1:1	1:1	1:4	1:0	2:3	1:2
	2:2		2:4		3:5	
		3:6			4:5	
			7:11			

Table 12. Estimated periods of the companion candidates.

Object	separation [″]	semi-major axis [AU]	M_{pr} [a]	M_{sc} [b]	Period [day]
9b	4.339	765	0.03	0.010	3.9×10^{7}
9c	8.50	1498	0.03	<0.006	1.1×10^{8}
15b	3.004	529	0.17	0.009	1.0×10^{7}
25b	4.320	761	0.19	0.015∼0.020	1.7×10^{7}
33b	5.203	917	0.03	<0.006	5.3×10^{7}
45b	2.301	406	0.02	<0.006	1.8×10^{7}

[a]DM(1Myr) [$M_\odot$]

[b]Burrows(1Myr)[$M_\odot$]

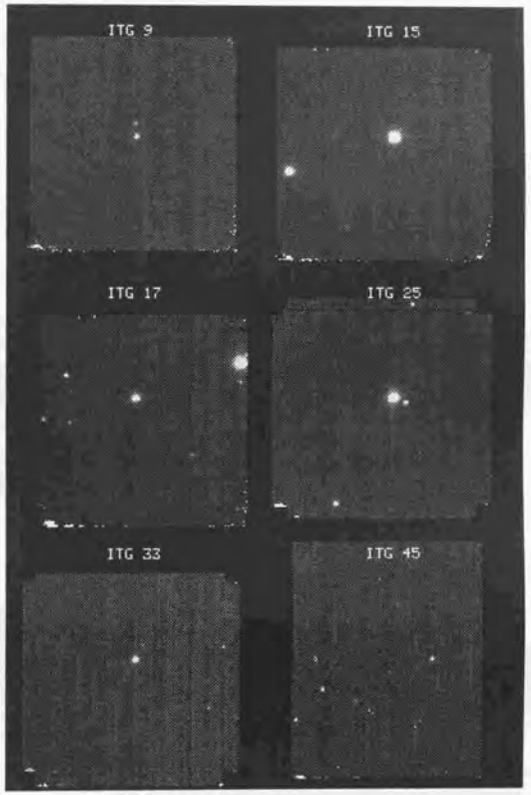

Fig. 1.— Ks band images of binary systems. The field of view of each image is about $60'' \times 60''$. (UH 2.2m)

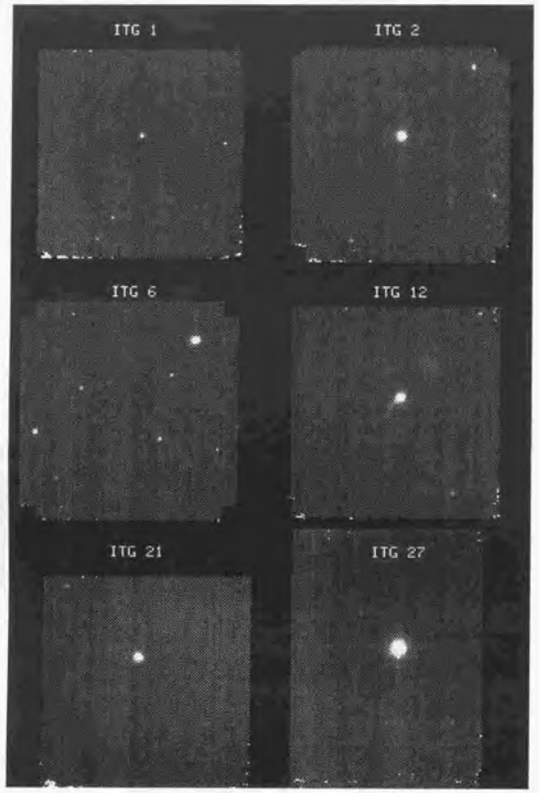

Fig. 2.— Ks band images of single stars. (UH 2.2m)

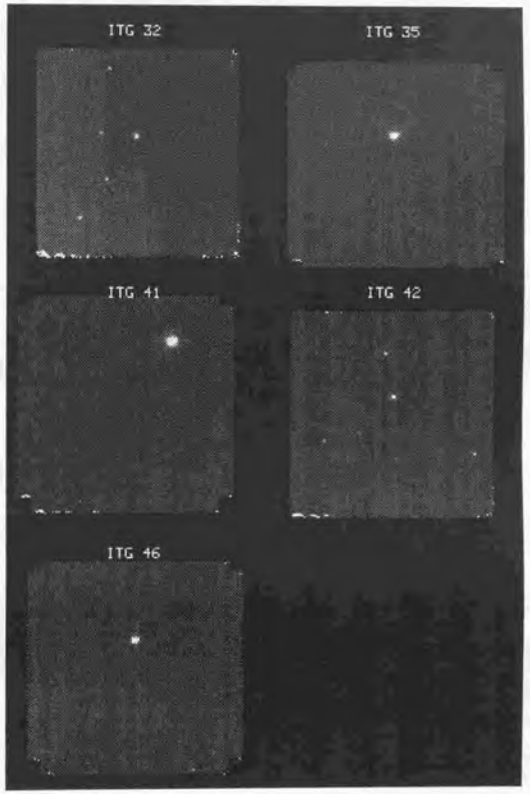

Fig. 3.— Ks band images of single stars. (UH 2.2m)

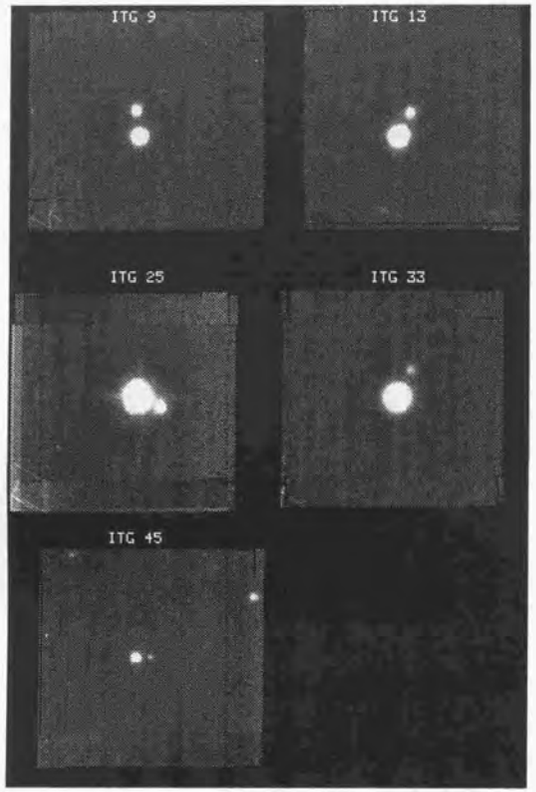

Fig. 4.— Ks band images of binary systems. The field of view of each image is about $40'' \times 40''$. (Palomar 5 m)

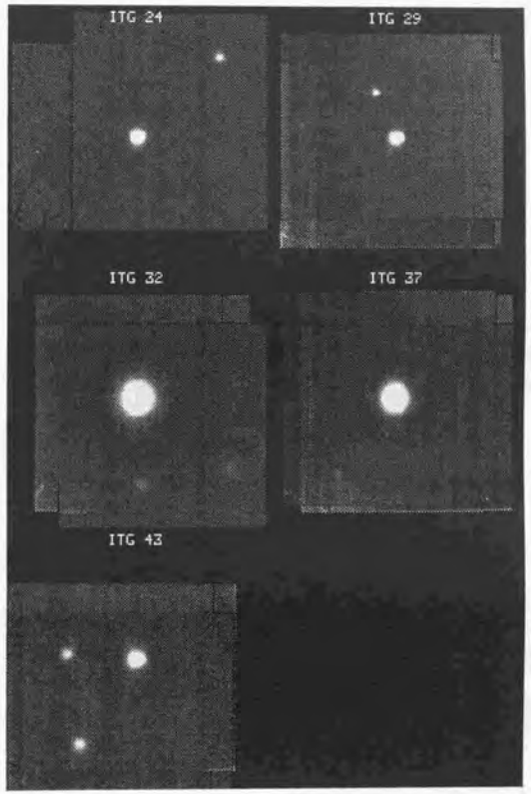

Fig. 5.— Ks band images of single stars. (Palomar 5 m)

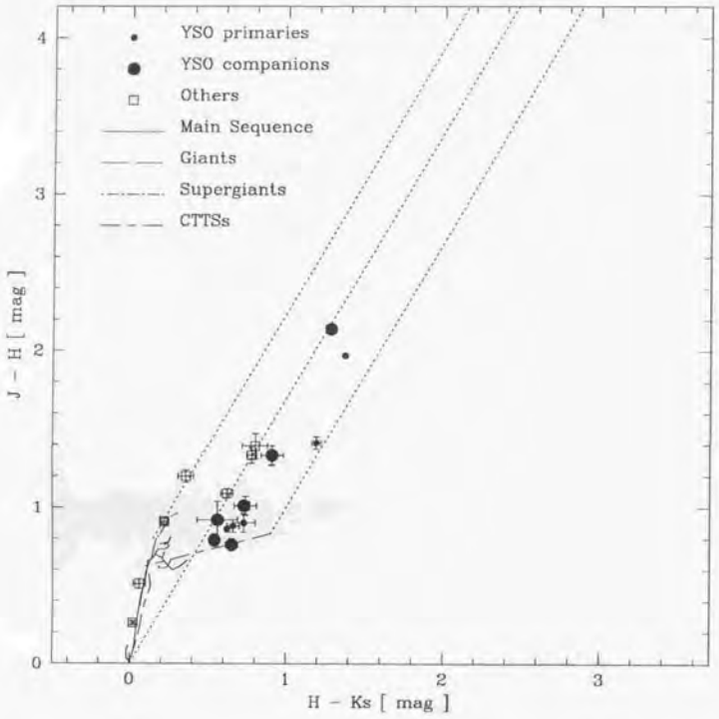

Fig. 6.— $(J-H, H-Ks)$ color-color diagram. The large filled circles represent the colors of YSO companions, the small circles represent the colors of YSO primaries, and the colors of background sources are shown by open squares.

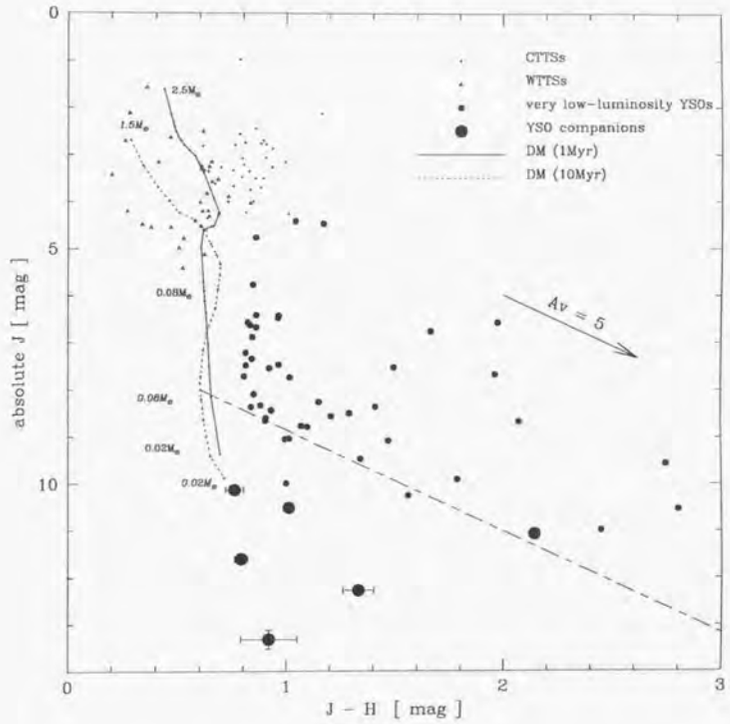

Fig. 7.— $(J-H, J)$ color-magnitude diagram.

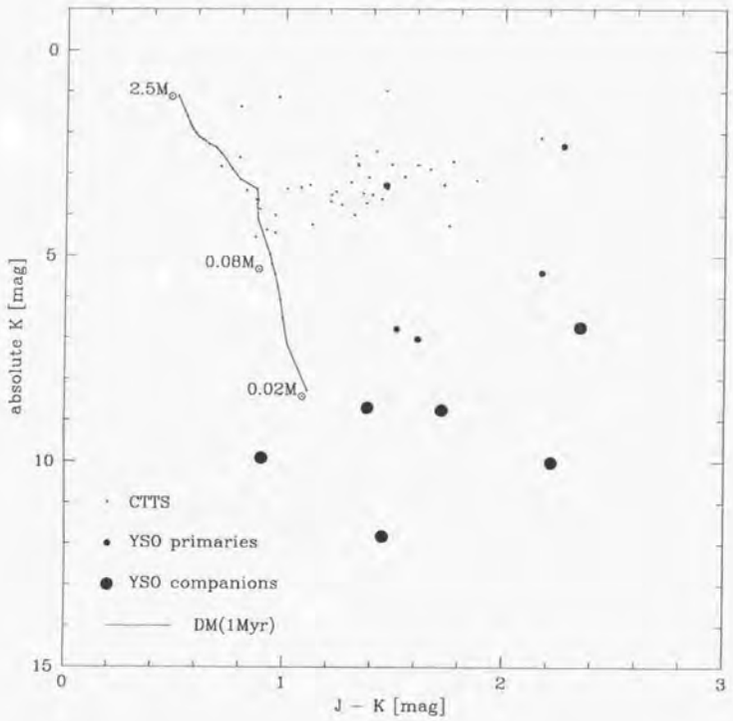

Fig. 8.— $(J-K, K)$ color-magnitude diagram.

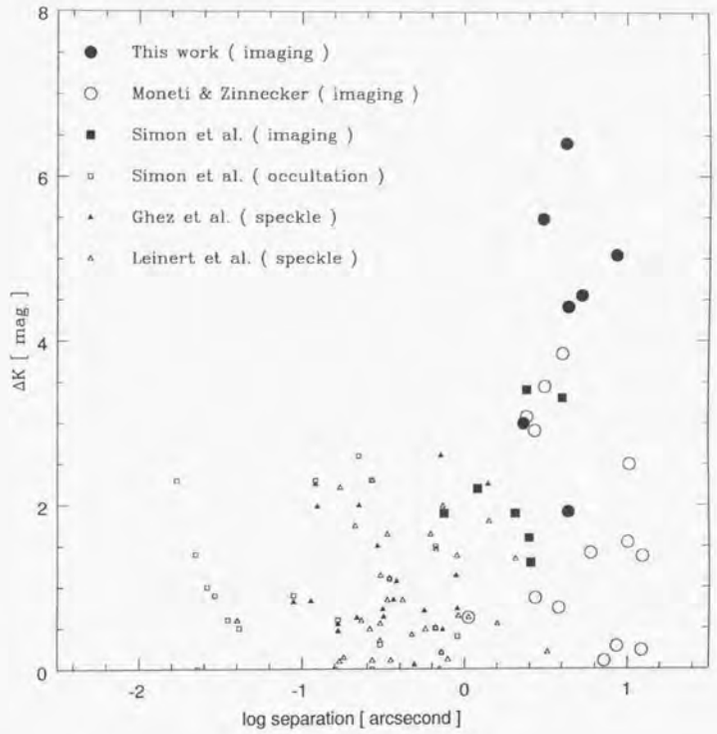

Fig. 9.— Magnitude differences between the primary and the companion at Ks band vs. separations.

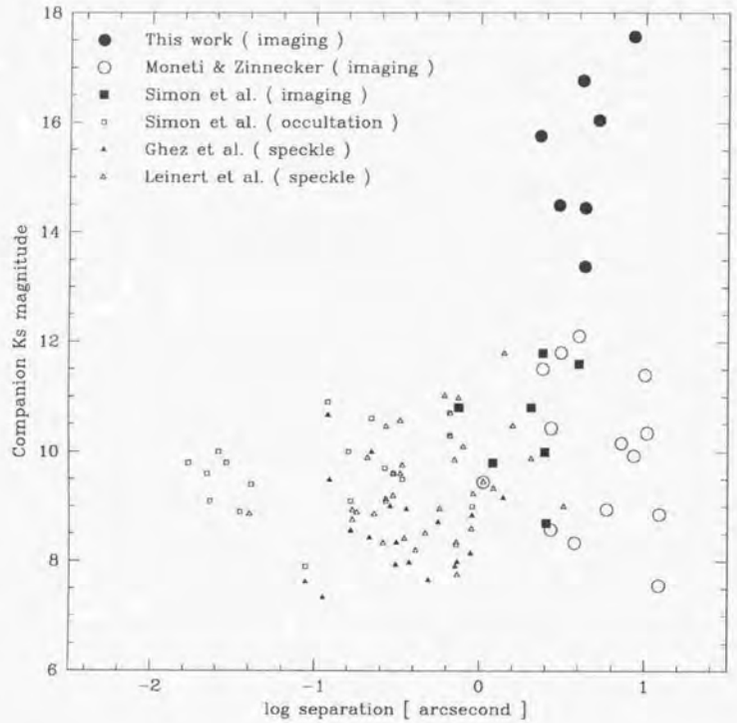

Fig. 10.— Ks magnitude of the companion vs. separation from the primary.

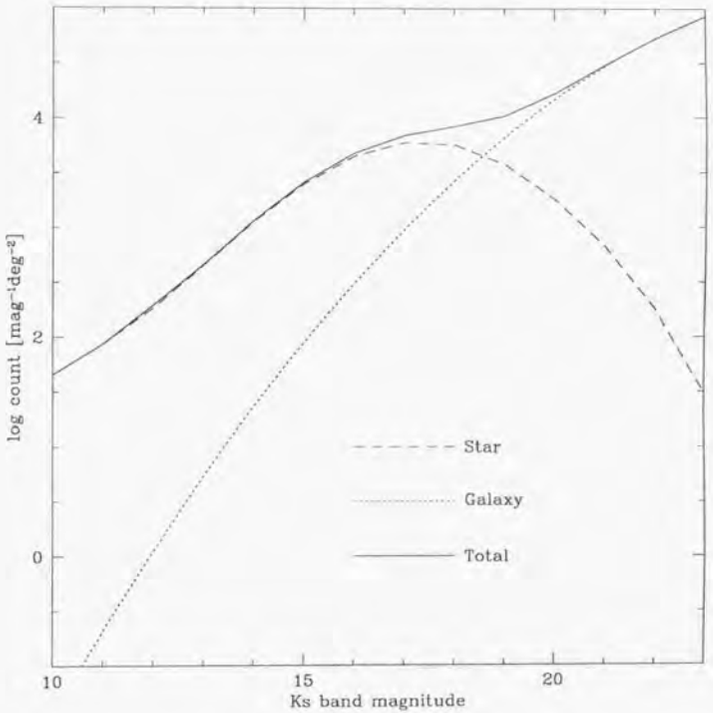

Fig. 11.— Expected number count of background objects at Ks band.

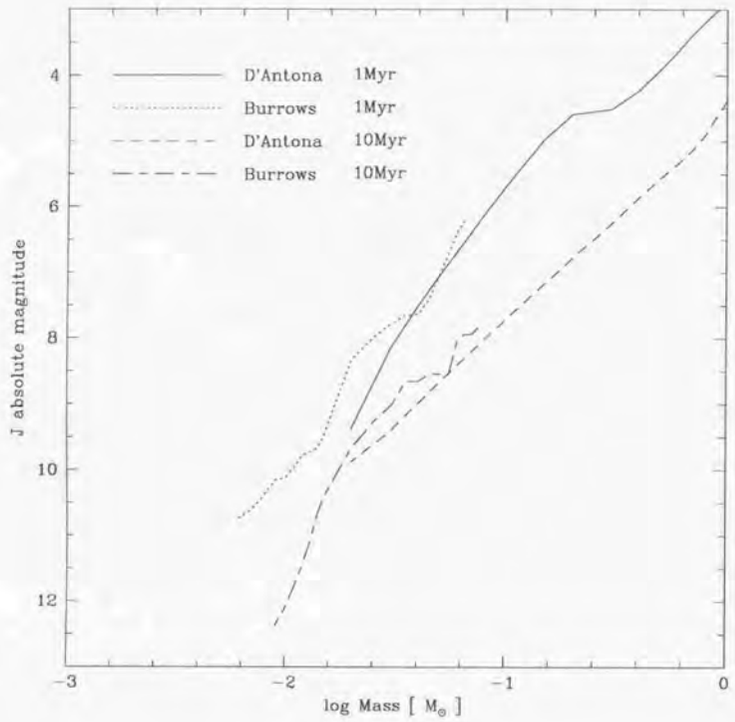

Fig. 12.— Mass – luminosity relation at J band.

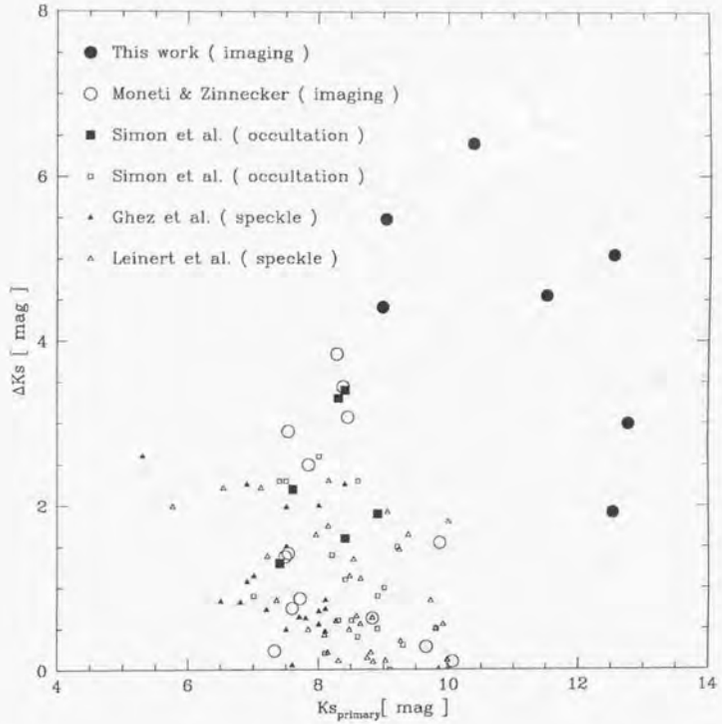

Fig. 13.— Magnitude difference between the primary and the companion at Ks band vs. Ks band magnitude of the primary.

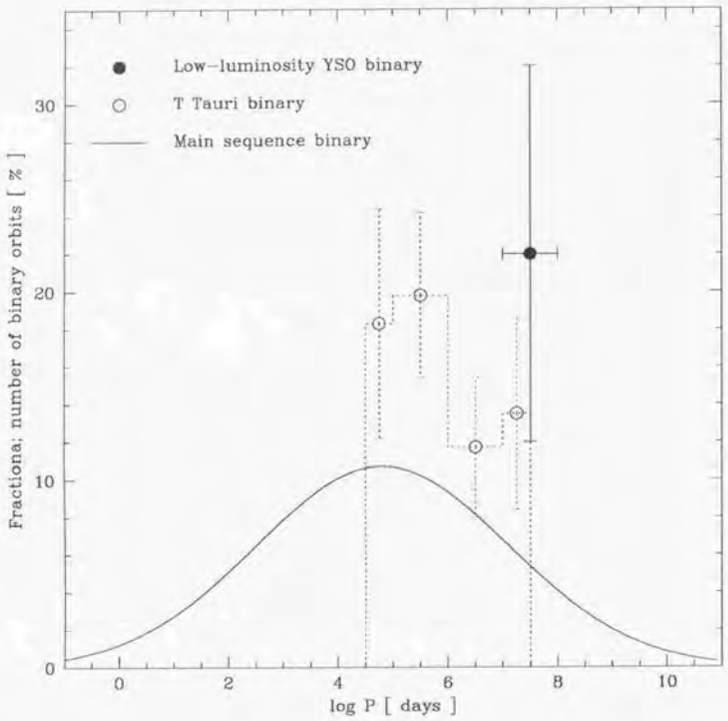

Fig. 14.— The binary frequency vs. orbital period. The binary frequency of nearby dwarfs (Duquennoy & Mayor 1993) are shown solid line, and the frequency of T Tauri stars(Leinert et al. 1994) are shown as dot line histogram.

Part IV

Prospective Remarks

We have found that low-luminosity ($K = 10 \sim 12$ mag) YSOs are indeed low-mass ($0.1 \sim 0.2 M_{\odot}$) YSOs by our spectroscopic observations. Many fainter YSO candidates are discovered by the previous wide-field survey and by the binary search. These object may be very low-mass YSOs, or young brown dwarfs. A moderate resolution ($R \sim 1000$) near-infrared spectroscopy of these objects using an 8 m class telescope, such as the Subaru telescope, will reveal that these objects are young brown dwarfs.

The very low-luminosity YSOs and the T Tauri stars night have different types of companions: The former tend to be associated with the companion much lighter than the primary, while the later with the companion of a similar mass to the primary. In order to confirm this posible difference, high dynamic range imaging observations around T Tauri stars are required. CIAO, the stellar coronagraph for the Subaru telescope, will be a powerful instrument for such observations. The small mass ratio for very low-luminosity YSO companions implys that these companions were born in the circumstellar disk around the primary object by fragmentation. Increasing of the sample number of very low-luminosity YSO companions, as well as spectroscopy of these companions to determine its temperature, are important.

The binary frequency of the low-luminosity YSOs is consistent with that of T Tauri stars, but significant higher than that of nearby main-sequence, that of the Pleiades, and that of the Hyades. The stellar density of the star-forming region could affect the binary frequency. In order to the clusitering effect, binary searches for denser star-forming regions, such as the ρ Oph cloud and the core of the Chamaeleon I cloud, are important.

REFERENCES

Aaronson, M., Frogel, J.A., & Persson, S.E., 1978, ApJ, 220, 442

Alcock, C., Allsman, R.A., Axelrod, T.S., et al., 1995, Phys. Rev. Lett., 74, 2867

Alexander, D.R., Johnson, H.R., & Rypma, R.L., 1983, ApJ, 272, 773

Alexander, D.R., Augason, G.C., & Johnson, H.R., 1989, ApJ, 345, 1014

Alexander, D.R., & Fergusson, J.W., 1994, ApJ, 437, 879

Ali, B., Carr, J.S., DePoy, D.L., Frogel, J.A., & Sellgren, K. 1995, AJ, 110, 2415

Allard, F., Hauschildt, P.H., Miller, S., & Tennyson, J., 1994, ApJ, 426, L39

Allard, F., & Hauschildt, P.H., 1995, ApJ, 445, 433

Ansari, R., Cavalier, F., Moniez, M., et al., 1996, A&A, 314, 94

Arnaud, K.A., Gilmore, G., & Cameron, A.C., 1989, MNRAS, 237, 495

Basri, G., Marcy, G.W., Graham, J.R., 1996, ApJ, 458, 600

Bertout, C., Basri, G., & Bouvier, J., 1988, ApJ, 330, 350

Bessell, M., & Brett, J., 1988, PASP, 100, 1134

Bessell, M., 1991, AJ, 101, 662

Bonnell, I.A., Martel, H., Bastien, P., Arcoragi, J.P., Benz, W., 1991, ApJ, 378, 553

Bonnell, I.A., 1994, MNRAS, 269, 837

Boss, A.P., 1997, science, 276, 1836

Bouvier, J., Rigaut, F., & Nadeau, D., 1997, A&A, 323, 139

Brandner, W., Alcala, J.M., Kunkel, M., Moneti, A., & Zinnecker, H., 1996, A&A, 307, 121

Briceño, C., Hartmann, L.W., Stauffer, J.R., Gagné, M., Stern, R.A., & Caillault, J.P., 1997, AJ, 113, 740

Burkert, A., & Bodenheimer, P., 1996, MNRAS, 280, 1190

Burrows, A., Marley, M., Hubbard, W. B., Lunine, J. I., Guillot, T., Saumon, D., Freedman, R., Sudarsky, D., & Sharp, C., 1997, ApJ, 491, 856

Cayrel, R., & Jugaku, J., 1963, Annales D'Astrophysique, 26, 495

Chabrier, G., & Baraffe, I., 1997. A&A, 327, 1039

Cohen, M., & Kuhi, L.V., 1979, ApJS, 41, 743

Comeron, F., Rieke, G., Burrows, A., & Rieke, M., 1993, ApJ, 416, 185

Cox, A.N., & Tabor, J.E., 1976, ApJS, 31, 271

D'Antona, F., & Mazzitelli, I., 1994, ApJS, 90, 467

Delfosse, X., Tinney, C.G., Forveille, T., Epchtein, N., Bertin, E., Borsenberger, J., Copet, E., de Batz, B., Fouque, P., Kimeswenger, S., le Bertr, T., Lacombe, F., Rouan, D., & Tiphene, D., 1997, A&A, 327, L25

Dickman, R.L. 1978, ApJS, 37, 407

Duquennoy, A., & Mayor, M., 1991, A&A, 248, 485

Elias, J.H., 1978, ApJ, 224, 857

Elias, J., Fogel, A., Matthews, K., & Neugebauer, G., 1982, AJ, 87, 1029

Fluks, M.A., Plez, B., The, P.S., de Winter, D., Westerlund, B.E., & Steenman, M.C., 1994, A&ASuppl., 105, 311

Forrest, W.J., Ninkov, Z., & Garnett, J.D., 1989, Proc. of 3rd IR. Tech. Workshop, ed. by C. McCreight, p.p.221

Frerking, M., Langer, W., & Wilson, R., 1982, ApJ, 262, 590

Fukui, Y., Mizuno, A., Nagahama, T., Imaoka, K., & Ogawa, H., 1991, Mem. Soc. Ast. It, 62, 801

Gardner, J.P., Cowie, L.L., & Wainscoat, R.J., 1993, ApJ, 415, L9

Ghez, A. M., Neugebauer, G., & Matthews, K., 1993 AJ, 106, 2005

Ghez, A. M., Weinberger, A.J., Neugebauer, G., & Matthews, K., 1995, AJ, 110, 753

Gliese, W., & Jahreiss, H., 1979, A&ASuppl., 38, 423

Greene, T.P., & Meyer, M.R., 1995, ApJ, 450, 233

Greene, T.P., & Lada, C.J., 1996a, AJ, 112, 2184

Greene, T.P., & Lada, C.J., 1996b, ApJ, 461, 345

Greene, T.P., & Lada, C.J., 1997, AJ, 114, 2157

Gullbring, E., Petrov, P.P., Ilyin, I., Gahm, G.F., & Lodén, K., 1996, A&A, 314, 835

Hambly, N.C., Hawkins, M.R.S., & Jameson, R.F., 1991, MNRAS, 253, 1

Harris, III, D.L., 1948, ApJ, 108, 112

Hartigan, P., Strom, K.M., & Strom, S.E., 1994, ApJ, 427, 961

Heintz, W.D., 1990, AJ, 99, 420

Henry, T.J., & McCarthy, Jr., D.W., 1990, ApJ, 350, 334

Irwin, A.W., 1981, ApJS, 45, 621

Itoh, Y., 1995, Master thesis, University of Tokyo (in Japanese)

Itoh, Y., Tamura, M., & Gatley, I., 1996, ApJ, 465, L129

Itoh, Y., Takato, N., Takami, H., & Tamura, M., 1998, accepted to PASJ

Johnson, H.L., 1966, ARA&A, 4, 193

Jones, H.R.A., Longmore, A.J., Jameson, R.F., & Mountain, C.M., 1994, MNRAS, 267, 413

Jones, H.R.A., Longmore, A.J., Allard, F., Hauschildt, P.H., Miller, S., Tennyson, J., 1995, MNRAS, 277, 767

Jones, H.R.A., Longmore, A.J., Allard, F., & Hauschildt, P.H., 1996, MNRAS, 280, 77

Jones, H.R.A., & Tsuji, T., 1997, ApJ, 480, L39

Jones, T., Ashley, M., Hyland, A., & Ruelas-Mayoroga, A., 1981, MNRAS, 197, 413

Kirkpatrick, J.D., Henry, T.J., & McCarthy, D.W., Jr. 1991, ApJS, 77, 417

Kirkpatrick, J.D., Kelly, D.M., Rieke, G.H., Liebert, J., Allard, F., & Wehrse, R., 1993, ApJ, 402, 643

Kirkpatrick, J.D., McGraw, J.T., Hess, T.R., Liebert, J., & McCarthy Jr., D.W., 1994, ApJS, 94, 749

Kleinmann, S.G., & Hall, D.N.B., 1986, ApJS, 62, 501

Koornneef, J., 1983, A&A, 128, 84

Kroupa, P., Tout, C.A., & Gilmore, G., 1990, MNRAS, 244 76

Kroupa, P., Tout, C.A., & Gilmore, G., 1993, MNRAS, 262, 545

Kurucz, R.L., 1991, in Stellar Atmospheres: Beyond the Classical Models, ed. Crivellari, L., Hubeny, I., & Hummer, D.G., Kluwer Academic Publ., p.p.441

Larson, R.B., 1985, MNRAS, 214, 379

Larson, R.B., 1992, MNRAS, 256, 641

Le Campion, J.F., Colin, J., & Geffert, M., 1996, A&Asuppl., 119, 307

Legett, S.K., 1992, ApJS, 82, 351

Legett, S.K., Allard, F., Berriman, G., Dahm, C.C., & Hauschildt, P.H., 1996, ApJS, 104, 117

Leinert, Ch., Zinnecker, H., Weitzel, N., Christou, J., Ridgway, S. T., Jameson, R., Haas, M., & Lenzen, R., 1993, A&A, 278, 129

Livingston, W., & Wallace, L., 1991, N.S.O. Technical Report No.91-001

Luhman, K.L., Liebert, J., & Rieke, G.H., 1997, ApJ, 489, L165

Luhman, K.L., & Rieke, G.H., 1998, ApJ, accepted

Mathieu, R.D., Walter, F.M., & Myers, P.C., 1989, AJ, 98, 987

Martín, E.L., 1997, A&A, 321, 492

Martin, E.L., Basri, G., Delfosse, X., & Forveille, T., 1997, A&A, 327, L29

Mayor, M., & Queloz, D., 1995, Nature, 378, 355

McDonald, J.M., & Clarke, C.J., 1993, MNRAS, 262, 800

Meyer, R.M., 1996, Ph.D. Thesis, University of Massachusetts

Moneti, A., & Zinnecker, H., 1991, A&A, 242, 428

Mouschovias, T,C., & Morton, S.A., 1991, ApJ, 371, 296

Murakawa, K., & Tamura, M., 1998, in preparation

Nakajima, T., Oppenheimer, B.R., Kulkarni, S.R., Golimowski, D.A., Matthews, K., & Durrance, S.T., 1995, Nature, 378, 463

Nakano, T., 1998, preprint

Nelson, L.A., Rappaport, S., & Joss, P.C., 1993, ApJ, 404, 723

Oasa, Y., Tamura, M., & Sugitani, K., 1998, in preparation

Okumura, S., 1997, Ph.D. Thesis, University of Tokyo

Oppenheimer, B.R., Kulkarni, S.R., Matthews, K., & Nakajima, T., 1995, Science, 270, 1478

Oppenheimer, B.R., Basri, G., Nakajima, T., & Kulkarni, S.R., 1997, AJ, 113, 296

Padgett, D.L., 1996, ApJ, 471, 847

Preibisch, T., & Smith, M.D., 1997, A&A, 322, 825

Reid, I.N., & Gizis, J.E., 1997, AJ, 114, 1992

Reipurth, B., Zinnecker, H., 1993, A&A, 278, 81

Salpeter, E.E., 1955, ApJ, 121, 161

Saumon, D., Bergeron, P., Lunine, J.I., Hubbard, W.B., & Burrows, A., 1994, ApJ, 424, 333

Scalo, J.M., 1986, *Fund. of Cosmic Phys.*, 11, 1

Simon, M., Ghez, A. M., Leinert, Ch., Cassar, L., Chen, W. P., Howell, R. R., Jameson, R. F., Matthews, K., Neugebauer, G., & Richichi, A., 1995, ApJ, 443, 625

Simon, D.A., Henry, T.J., & Kirkpatrick, J.D., 1996, AJ, 112, 2238

Simons, D.A., & Becklin, E.E., 1992, ApJ, 390, 431

Stauffer, J., Hamilton, D., Probst, R., Rieke, G., & Mateo, M., 1989, ApJ, 344, L21

Stauffer, J., Herter, T., Hamilton, D., Rieke, G., Rieke, C.J., Probst, R., & Forrest, W. 1991, ApJ, 367, L23

Steele, I.A., Jameson, R.F., Hodgkin, S.T., & Hambly, N.C., 1995, MNRAS, 275, 841

Stringfellow, G.S., 1991, ApJ, 374, L21

Strom, K., Strom, S., Edwards, S., Cabrit, S., & Strutskie, M., 1989, AJ, 97, 1451

Strom, K.M., Strom, S.E., & Merrill, K.M., 1993, ApJ, 412, 233

Sunada, K., 1998, in preparation

Tamura, M., Gatley, I., Walter, W., & Werner, M., 1991, ApJ, 374, L25

Tinney, C.G., Mould, J.R., & Reid, I.N., 1993, AJ, 1045, 105

Tinney, C.G., Delfosse, X., & Forveille, T., 1997, ApJ, 490, L95

Tokunaga, A., 1998 in Astrophysical Quantities, ed. A.N. Cox (New York: AIP)

Tsuji, T., & Ohnaka, K., 1994, in Elementary Processes in Dense Plasmas ed. by Ichimaru, S., & Ogata, S. (Addison-Wesley)

Tsuji, T., Ohnaka, K., & Aoki, W., 1996, A&A, 305, L1

Wallace, L., & Hinkle, K., 1996, ApJS, 107, 312

Wilking, B.A., McCaughrean, M.J., Burton, M.G., Giblin, T.Y., Rayner, J.T., & Zinnecker, H., 1997, AJ, 114, 2029

Williams, D.M., Comeron, F., Rieke, G.H., & Rieke, M.J., 1995, ApJ, 454, 144

This manuscript was prepared with the AAS LaTeX macros v4.0.